

AD-A181 671

ESTIMATION OF CORONARY ARTERY DIMENSIONS FROM  
ANGIOGRAMS(U) MASSACHUSETTS INST OF TECH CAMBRIDGE  
RESEARCH LAB OF ELECTRONICS T N PAPPAS APR 87 TR-528

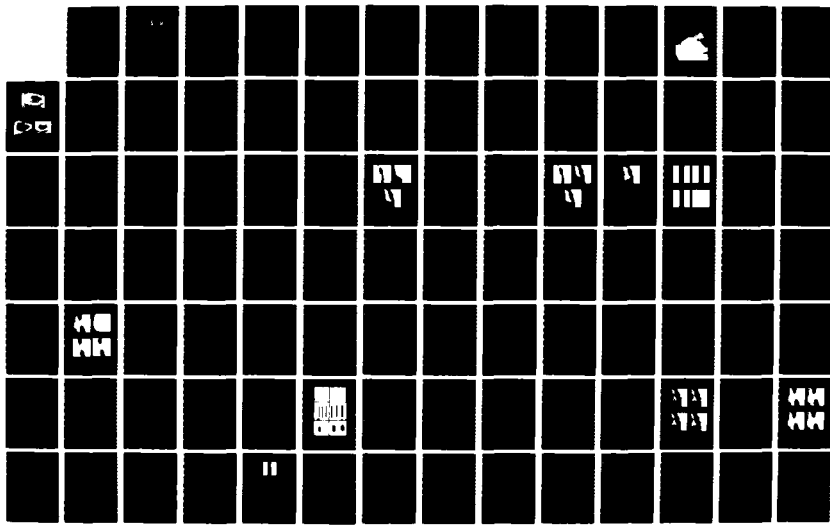
1/2

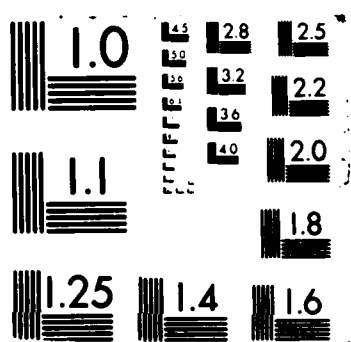
UNCLASSIFIED

N00014-81-K-0742

F/G 6/5

NL



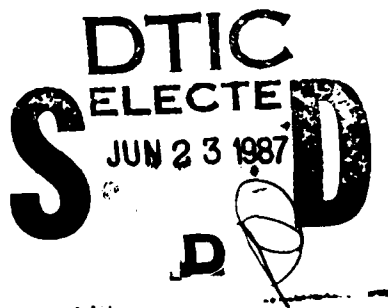


Massachusetts Institute of Technology  
Department of Electrical Engineering and Computer Science  
Research Laboratory of Electronics  
Room 36-615  
Cambridge, MA 02139

12

DTIC FILE COPY

AD-A181 671



Estimation of Coronary Artery Dimensions

from Angiograms

Thrasyvoulos N. Pappas

Technical Report No. 528

April 1987

DISTRIBUTION STATEMENT A

Approved for public release;  
Distribution Unlimited

This work has been supported in part by the Advanced Research Projects Agency monitored by ONR under Contract No. N00014-81-K-0742 and in part by the National Science Foundation under Grant ECS-8407285.

UNCLASSIFIED

SECURITY CLASSIFICATION OF THIS PAGE

A181671

## REPORT DOCUMENTATION PAGE

1a. REPORT SECURITY CLASSIFICATION		1b. RESTRICTIVE MARKINGS	
2a. SECURITY CLASSIFICATION AUTHORITY		3. DISTRIBUTION/AVAILABILITY OF REPORT Approved for public release; distribution unlimited.	
2b. DECLASSIFICATION/DOWNGRADING SCHEDULE		4. PERFORMING ORGANIZATION REPORT NUMBER(S)	
5. MONITORING ORGANIZATION REPORT NUMBER(S)		6a. NAME OF PERFORMING ORGANIZATION Research Laboratory of Electronics Massachusetts Institute of Technology	
6b. OFFICE SYMBOL (If applicable)		7a. NAME OF MONITORING ORGANIZATION Office of Naval Research Mathematical & Information Scien.Div.	
6c. ADDRESS (City, State and ZIP Code) 77 Massachusetts Avenue Cambridge, MA 02139		7b. ADDRESS (City, State and ZIP Code) 800 North Quincy Street Arlington, Virginia 22217	
8a. NAME OF FUNDING/SPONSORING ORGANIZATION Advanced Research Projects Agency		9. PROCUREMENT INSTRUMENT IDENTIFICATION NUMBER N00014-81-K-0742	
8c. ADDRESS (City, State and ZIP Code) 1400 Wilson Boulevard Arlington, Virginia 22217		10. SOURCE OF FUNDING NOS. PROGRAM ELEMENT NO.      PROJECT NO.      TASK NO.      WORK UNIT NO. NR      049-506	
11. TITLE (Include Security Classification) Estimation of Coronary Artery Dimensions		12. PERSONAL AUTHORIS) from Angiograms.      Thrasyvoulos Nicholaou Pappas	
13a. TYPE OF REPORT Technical		13b. TIME COVERED FROM _____ TO _____	
14. DATE OF REPORT (Yr., Mo., Day) April 1987		15. PAGE COUNT 124	
16. SUPPLEMENTARY NOTATION			
17. COSATI CODES FIELD      GROUP      SUB. GR.		18. SUBJECT TERMS (Continue on reverse if necessary and identify by block number)	
19. ABSTRACT (Continue on reverse if necessary and identify by block number) A new approach is presented for the measurement of the severity of coronary obstructions from coronary angiograms. An angiogram is an x-ray picture of arteries in which a contrast agent has been injected. Existing techniques are heuristic and their performance is not satisfactory. The proposed approach exploits the characteristics of the signals involved. A model of the film density of the coronary angiograms is developed and used to estimate the diameter and cross-sectional area at each point along the vessel. The model accounts for the structure of the vessel and background, as well as the distortions introduced by the imaging system. Both a one-dimensional and a two-dimensional model of the angiogram are presented. The algorithms are tested on synthetic data, on x-rays of contrast-medium-filled cylindrical phantoms, and on real coronary angiograms. Both algorithms are shown to have better performance than current methods. Moreover, the two-dimensional algorithm is better than the one-			
20. DISTRIBUTION/AVAILABILITY OF ABSTRACT UNCLASSIFIED/UNLIMITED <input checked="" type="checkbox"/> SAME AS RPT <input type="checkbox"/> DTIC USERS <input type="checkbox"/>		21. ABSTRACT SECURITY CLASSIFICATION Unclassified	
22a. NAME OF RESPONSIBLE INDIVIDUAL Kyra M. Hall RLE Contract Reports		22b. TELEPHONE NUMBER (Include Area Code) (617) 253-2569	22c. OFFICE SYMBOL →

UNCLASSIFIED

cont'd

dimensional algorithm.

UNCLASSIFIED



Accesion For	
NTIS	CRA&I
DTIC	TAB
Unannounced	<input type="checkbox"/>
Justification	
By _____	
Distribution /	
Availability Codes	
Dist	Aval and/or Special
A-1	

3

## Acknowledgements

I would like to thank Professor Jae Lim for his encouragement, guidance, and support during this thesis research. It has been a pleasure working with him. I would also like to thank my thesis readers Professor Alan Oppenheim and Dr. Dan Duggeon.

I am indebted to Dr. Tamas Sandor of the Harvard Medical School for many useful discussions on the problem, especially during the early stages of the research. Dr. Sandor provided all the angiograms used in this thesis.

Thanks to all members of the Digital Signal Processing Group at MIT for providing an enjoyable and stimulating environment. Discussions with Farid Dowla, Dennis Martinez, Evangelos Milios, and Patrick Van Hove were particularly useful.

Many thanks to all those who dedicated considerable effort to maintaining the group computing facility in excellent shape, Giovanni Aliberti, Webster Dove, Dennis Martinez, Bruce Musicus, and Cory Myers. Giovanni in particular has been a special friend in addition to solving all the system problems that came up during the writing of this thesis.

I also wish to acknowledge the support provided by the National Science Foundation and the Advanced Research Projects Agency during this research.

This thesis is dedicated to my parents for their love and support throughout my education.

# Contents

<b>1</b>	<b>Introduction</b>	<b>9</b>
1.1	Problem Statement . . . . .	16
1.2	Existing Techniques . . . . .	17
1.3	Scope of the Thesis . . . . .	20
1.4	Summary and Notation . . . . .	22
<b>2</b>	<b>Coronary Angiogram Model</b>	<b>23</b>
2.1	Perfect Imaging System . . . . .	24
2.2	Two-Dimensional Vessel Model . . . . .	25
2.3	Two-Dimensional Model of Background . . . . .	31
2.4	Model of Imaging Process . . . . .	32
2.5	One-Dimensional Model . . . . .	39
<b>3</b>	<b>Estimation of Model Parameters</b>	<b>44</b>
3.1	One-Dimensional Model . . . . .	45
3.2	Two-Dimensional Model . . . . .	48
3.2.1	Comparison With One-Dimensional Approach . . . . .	53
3.3	Initial Vessel Estimate . . . . .	54
<b>4</b>	<b>Comparison of One-Dimensional Model With Slope Methods</b>	<b>57</b>
4.1	Synthetic Data . . . . .	58
4.1.1	Effect of Noise Level . . . . .	60
4.1.2	Effect of Vessel Radius . . . . .	63
4.1.3	Effect of Parameter Alpha . . . . .	66
4.1.4	Effect of Background . . . . .	69
4.1.5	Remarks . . . . .	73
4.2	Vessel Phantoms . . . . .	73
4.3	Coronary Angiograms . . . . .	79
4.4	Summary . . . . .	83
<b>5</b>	<b>Comparison of Two-Dimensional Model With One-Dimensional Model</b>	<b>85</b>
5.1	Synthetic Data . . . . .	86

5.1.1	Effect of Noise Level . . . . .	88
5.1.2	Effect of Vessel Radius . . . . .	91
5.1.3	Effect of Parameter Alpha . . . . .	94
5.1.4	Realistic Example . . . . .	97
5.1.5	Remarks . . . . .	103
5.2	Vessel Phantoms . . . . .	103
5.3	Coronary Angiograms . . . . .	107
5.4	Summary . . . . .	117
<b>6</b>	<b>Summary and Future Work</b>	<b>118</b>
6.1	Summary . . . . .	118
6.2	Suggestions for Further Research . . . . .	119

# List of Figures

1.1 Coronary Angiogram . . . . .	10
1.2 Cross-Sections of Stenotic Coronary Arteries . . . . .	13
1.3 Vessel Cross-Section and Projection . . . . .	15
1.4 Projection of Vessel Cross-Section . . . . .	16
2.1 Imaging System . . . . .	23
2.2 Generalized Cylinder and Its Projection . . . . .	26
2.3 Ellipse and Its Line Integral Projection . . . . .	27
2.4 Line-Integral Projections of Stenotic Vessel Cross-Sections . . . . .	29
2.5 Perfect Model . . . . .	33
2.6 Two-Dimensional Model . . . . .	36
2.7 Real Angiogram . . . . .	37
2.8 Comparison of Vessel Phantom and Model . . . . .	38
2.9 One-Dimensional Model . . . . .	41
2.10 Comparison of Vessel Phantom and Model . . . . .	43
3.1 Example of Fine Perturbation . . . . .	52
3.2 Example of Crude Perturbation . . . . .	53
3.3 Initial Estimate of Vessel . . . . .	56
4.1 Synthetic Densitometric Profile . . . . .	59
4.2 Radius Estimation for Different SNR's . . . . .	61
4.3 Area Estimation for Different SNR's . . . . .	62
4.4 Radius Estimation for Different Radii . . . . .	64
4.5 Area Estimation for Different Radii . . . . .	65
4.6 Radius Estimation for Different Alphas . . . . .	67
4.7 Area Estimation for Different Alphas . . . . .	68
4.8 Different Backgrounds for Background Experiment . . . . .	70
4.9 Radius Estimation for Different Backgrounds . . . . .	71
4.10 Area Estimation for Different Backgrounds . . . . .	72
4.11 Vessel Phantoms . . . . .	74
4.12 Vessel Phantom Cross-Section and Perfect Projection . . . . .	75
4.13 Phantom Experiment: Radius Estimation . . . . .	76
4.14 Phantom Experiment: Area Estimation . . . . .	78

4.15 Boundary Detection (Example A) . . . . .	80
4.16 Cross-sectional Area Detection (Example A) . . . . .	81
4.17 Boundary Detection (Example B) . . . . .	82
4.18 Cross-sectional Area Detection (Example B) . . . . .	83
5.1 Two-Dimensional Synthetic Image . . . . .	87
5.2 Radius Estimation for Different SNR's . . . . .	89
5.3 Area Estimation for Different SNR's . . . . .	90
5.4 Radius Estimation for Different Radii . . . . .	92
5.5 Area Estimation for Different Radii . . . . .	93
5.6 Radius Estimation for Different Alphas . . . . .	95
5.7 Area Estimation for Different Alphas . . . . .	96
5.8 Two-Dimensional Synthetic Image . . . . .	97
5.9 Vessel Parameter Sequences . . . . .	98
5.10 Vessel Parameter Estimates . . . . .	100
5.11 Radius Estimation for Different SNR's . . . . .	101
5.12 Area Estimation for Different SNR's . . . . .	102
5.13 Phantom Experiment: Radius Estimation . . . . .	105
5.14 Phantom Experiment: Area Estimation . . . . .	106
5.15 Two-Dimensional Model (Example A) . . . . .	108
5.16 Estimated Parameter Sequences (Example A) . . . . .	109
5.17 One-Dimensional Model (Example A) . . . . .	110
5.18 Smoothed One-Dimensional Model (Example A) . . . . .	111
5.19 Two-Dimensional Model (Example B) . . . . .	113
5.20 One-Dimensional Model (Example B) . . . . .	114
5.21 Smoothed One-Dimensional Model (Example B) . . . . .	115
5.22 Estimated Parameter Sequences (Example B) . . . . .	116

# Chapter 1

## Introduction

The precise and objective measurement of the severity of coronary artery obstructions is important in the treatment of patients with ischemic heart disease, that is, deficiency of blood supply to the heart.

The coronary arteries are the vessels which encircle the heart and supply blood directly to the heart muscle. Narrowing of the coronary arteries, usually as a result of atherosclerosis, prevents adequate supply of blood to the heart, causing pain and, eventually, damage to the heart muscle. Such damage of the heart is called coronary disease. The number of deaths from coronary disease has increased strikingly in the last 70 years in association with a marked prolongation of the average life span [1]. In order to restore normal flow of blood to the heart, over 100,000 coronary artery bypass surgical procedures are undertaken each year [1].

An angiogram is an x-ray picture of arteries taken after a contrast agent has been injected into the vessels. Coronary angiography is necessary to determine whether a bypass operation is needed. In addition, it is an essential part of any surgical therapeutic approach, as it is used for the preparation and evaluation of the results of surgery. An example of a coronary angiogram is shown in figure 1.1. In the case of coronary angiograms the injection of the contrast agent is done via a catheter directly to the arteries to achieve high concentrations. At present the



Figure 1.1: Coronary Angiogram

best storage medium for the coronary angiograms is 35mm cinefilm, because of its inherent high resolution.

Conventional visual evaluation of the severity of coronary obstructions has been characterized by large inter- and intra-observer variability [12,36,11,24]. Thus, the development of digital processing techniques for the precise and objective measurement of the severity of coronary obstructions from coronary angiograms is important in the treatment of patients with ischemic heart disease.

Coronary artery imaging presents special problems, because of their location on the beating heart and their shape and size. For example, intravenous digital radiography can be used to visualize most of the major arteries except the coronaries. When the injection is intravenous the SNR of the angiographic image is low. To improve the SNR, an x-ray image obtained before injection of contrast agent into the vessels is subtracted from an image obtained after injection. The image that is obtained in this way contains the vessels in uniform background. In the coronary artery case subtraction results in poor quality images, because of the rapid movement of the heart. As a result of these special problems many techniques that have been used quite successfully for stenosis determination of other arteries, like the femoral and carotid, do not have satisfactory performance when applied to coronary arteries.

The most commonly used measure of an obstruction is percent stenosis, which is determined as the maximum percent arterial narrowing within a specified length of the vessel

$$\text{stenosis (\%)} = \frac{d_1 - d_2}{d_1} 100 \quad (1.1)$$

where  $d_1$  is the diameter (or cross-sectional area) of the normal section of the artery and  $d_2$  is the diameter (or cross-sectional area) of the most obstructed section. Of course, the resulting stenosis is different depending on whether we use the diameter or the cross-sectional area. According to equation (1.1), in determining the severity of an obstruction, it is the relative dimensions of the vessel that matter, not the ab-

solute ones. However, in some cases it is important to have absolute measurements of vessel dimensions, especially when it is not possible to locate with certainty a normal section of the vessel.

The hemodynamic resistance of the vessel is determined by the cross-sectional area of the vessel. According to Poisenille's equation, the pressure gradient  $P$  necessary to ensure a constant flow  $F$  in a cylindrical vessel of radius  $r$  and length  $L$  is given by

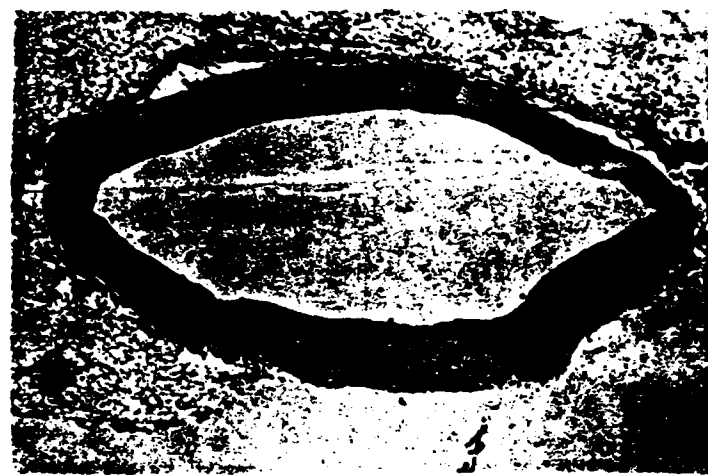
$$P = \frac{8\mu LF}{\pi r^4} = \frac{8\pi\mu LF}{A^2} \quad (1.2)$$

where  $\mu$  is the coefficient of viscosity and  $A$  is the cross-sectional area of the vessel [4]. This theoretical result has also been corroborated by experimental studies [13,14]. Thus, the vessel dimension that is most significant for this problem is the cross-sectional area. The severity of heart disease is determined by the cross-sectional area of the obstructed segments of the vessel.

According to almost unanimous opinion, the stenoses regarded as significant enough to require an operation are those which reduce the lumen (that is the cross-sectional area) by 75% - 100% [4]. Thus, it is important to have accurate estimates of the vessel dimensions at its most narrow points, as they may determine whether an operation is needed.

The cross-sectional area of the vessel can be obtained from the diameter, if the vessel has a circular cross-section. This is approximately true for healthy vessels, but at a coronary obstruction the shape of the cross-section is frequently irregular. Figure 1.2 shows a few characteristic examples of such cross-sections taken from Abrams [1]. In such cases it is obvious that the diameter depends on the angle of projection, and does not provide a good estimate of the area.

The methods which estimate the area of the cross-sections directly from the image density are usually called densitometric. These methods assume that the contrast agent is mixed homogeneously with blood, and also that there is a linear relationship between the density of the radiographic image and the thickness of con-



(a)



(b)



(c)

Figure 1.2: Cross-Sections of Stenotic Coronary Arteries

trast agent. This relationship can be secured under rigidly controlled experimental radiographic conditions [23,9]. When this is not possible, appropriate corrections must be taken. Spears developed a rotating wedge technique for linearization of cineangiographic gray scale with contrast medium thickness [30,31]. A different technique for transforming x-ray density levels to irradiated object thickness was implemented by Reiber et al. [17]. Thus, densitometric methods require strict densitometric checks and, if necessary, calibration of the imaging system.

The maximum percent area reduction, as defined in equation (1.1), is a reasonable estimate of heart disease. Obviously, a more accurate indication of the severity of the obstructions would be the exact shape of the cross-section at each point along the artery. As we will see in chapter 2 the optical density distribution of the radiographic image is the line-integral projection of the x-ray attenuation coefficient along each ray path through the human body. According to the projection-slice theorem, if we know the projections at all angles, then we can reconstruct the object exactly. Since the attenuation coefficient of the contrast agent inside the arteries is different from the coefficient of the surrounding material, we can thus obtain the vessel cross-sections. However, there are practical problems in obtaining and combining angiograms of more than one view. More than one view perpendicular to the long axis of a given vessel segment often cannot be obtained, because of overlapping branches [31,33]. Even when we can get more views, proper registration of the projections in the various views is difficult to achieve because of motion of the heart. Thus it is important to extract as much information as possible about the vessel cross-sections from one projection.

It is clear that we cannot reconstruct the vessel cross-sections from one projection. Even if we could isolate the vessel component of the projection, we could not reconstruct the vessel cross-section, unless we had some *a priori* information about its shape. However, some vessel parameters can easily be obtained from the vessel component of the projection. Figure 1.3 shows one of the vessel cross-sections of

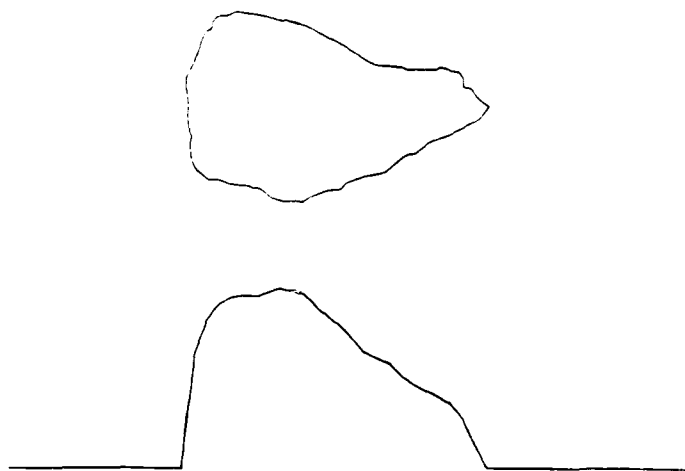
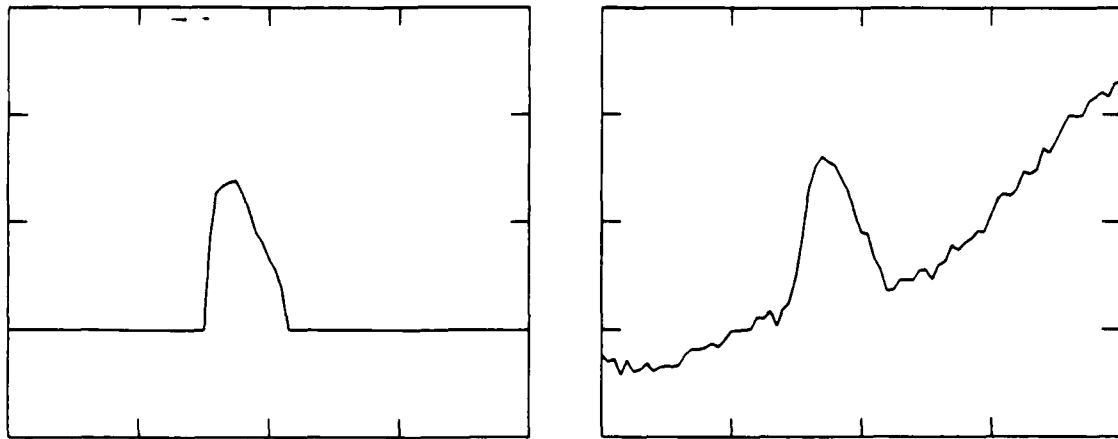


Figure 1.3: Vessel Cross-Section and Projection

figure 1.2 and its projection, assuming a perfect imaging system and uniform contrast agent concentration within the vessel. This projection corresponds to a linear profile perpendicular to the two-dimensional vessel projection. The cross-sectional area is the integral along this profile. The diameter of the cross-section is simply the length of the nonzero projection values. It is clear that the diameter changes when we rotate the vessel, while the cross-sectional area does not.

The problem of course is that we do not have the vessel component of the projection. There are other objects in the background, and distortions are introduced by the imaging system. The task of isolating the vessel component is not easy. As a result, the problems of estimating the diameter and cross-sectional area of the vessel become nontrivial. Figure 1.4(a) shows the projection of figure 1.3, which assumes a perfect imaging system. Figure 1.4(b) shows the same projection after we added a low order polynomial (background), convolved with a Gaussian line spread function (blur), and added white noise. The resulting profile is close to what we would obtain from the actual imaging system. We observe that, while it is straight forward



(a) Perfect Imaging System

(b) Actual Imaging System

Figure 1.4: Projection of Vessel Cross-Section

to obtain the diameter and the area from the first projection, it is not obvious how we would obtain the same parameters from the second.

## 1.1 Problem Statement

The problem we will consider in this thesis is the following. Given a coronary angiogram, that is, one view of an artery, estimate the diameter and cross-sectional area at each point along the artery. We will assume that we have a single isolated vessel. We will not attempt to handle branch points and overlapping vessels. Our procedure for computer measurement of coronary angiograms assumes that the angiographer selects the vessel segment to be analyzed.

The diameter we will be estimating is the one parallel to the projection plane. As we saw above this diameter is sensitive to vessel rotation. The cross-sectional area on the other hand does not present this problem. In addition to this, the cross-sectional area determines the hemodynamic resistance of the vessel. Hence the

cross-sectional area is a more attractive measure of vessel obstruction. However, cross-sectional area estimation assumes that there is a linear relationship between the density of the radiographic image and the thickness of contrast agent. As we have already mentioned, when this is not true, appropriate corrections must be taken. The advantage of the diameter estimates is that they are not sensitive to deviations from this linear relationship. The experiments with vessel phantom angiograms in chapters 4 and 5 illustrate these points.

The severity of heart disease is determined by the most obstructed segments of the vessel. It is usually the greatest degree of narrowing observed that is recorded by the angiographer [4]. Thus it is important to have accurate estimates of the vessel dimensions at the most narrow points. An algorithm that estimates the vessel dimensions very accurately at most points along the vessel except the very narrow ones is not very useful.

## 1.2 Existing Techniques

Current algorithms analyze the angiograms by examining the densitometric profiles of a series of lines perpendicular to the vessel image. Their objective in most cases is to find the diameter or the area of the vessel. In both cases the boundary points of the vessel must be determined. Most algorithms are quite heuristic and find the boundaries of the artery by first smoothing the profile and then finding the inflection points (extrema of the first derivative), or the knee points (maxima of the second derivative) [26,16,3,32,15]. Smoothing is done by averaging or fitting some polynomial or spline function to the projection profile. Barth *et al.* [5] use a correlation technique to find the positions of maximal second derivative. Smith *et al.* [29] do not use derivative operators to determine the boundaries; instead they select a threshold level after background subtraction. The diameter of the vessel is obtained as the distance between the two boundary points. The area

is obtained as the integral of the projection profile between the boundary points after the background has been estimated and subtracted. The estimation of the background is, in our view, a nontrivial task. Some authors [16] estimate the background by computing the linear regression line through the points directly left and right of the detected boundaries. Smith *et al.* [29] estimate the background by sliding a large sphere underneath the surface of the image. An extensive overview of many of these heuristic methods is given in [20].

We will refer to the methods described above as the slope methods, because they base their analysis on the slope of the profiles. Their main advantage is their computational simplicity. They are heuristic, however, and their performance is not satisfactory. As we will see in chapter 4 this is especially true at the narrow sections of the vessels, which are the most important ones. We will also show that they are sensitive to scaling of the image. The choice of the inflection points is arbitrary, except for the fact that they are close to what our eyes perceive as the vessel edge. In fact, the inflection points are typically located inside the actual vessel edges. The knee points happen to be closer to the true boundaries, but again the choice is arbitrary. As one would expect, the knee points are less reliable than the inflection points, because second derivatives are involved.

Another problem with the slope methods is that they do not take fully into account the spatial continuity of the vessel. One way to use the vessel continuity is by averaging the profiles before finding the edge points. An alternative is to smooth the edge points after detection. Finally, the detected points of one profile can be used to determine bounds for the location of the edge points of the next profile. There are problems associated with each approach. Averaging of the profiles may result in loss of resolution. The same is true for smoothing of the detected boundaries. The use of the bounds can lead to very distorted boundaries, or totally wrong ones, because, if the algorithm starts tracking the wrong edge, it is impossible for it to recover.

Inaccuracies in the estimation of the vessel boundaries by the slope methods affect the cross-sectional area estimates as well as the diameter estimates. The area estimates are affected because the area is obtained as the integral between the boundary points after background subtraction, and also because the background estimate depends on the boundary points.

Shmueli used a modeling approach to detect vessel boundaries in subtraction angiograms [27,28]. Subtraction angiograms are obtained when an x-ray image obtained before injection of contrast agent into the vessels is subtracted from an image obtained after injection. The purpose of the subtraction is to remove the background and thus increase the signal to noise ratio (SNR) of the vessel image. In subtraction angiography the injection is intravenous and so the SNR of the final image is low. Shmueli's algorithm is designed to detect vessels in uniform background and was applied to simulated data and to vessel phantom measurement data. As we have already mentioned subtraction angiograms of the coronary arteries are especially difficult to obtain and are not currently used for diagnostic purposes, because of their poor quality (low SNR).

Shmueli assumes a simple model for the profiles perpendicular to the vessel. It is based on the assumption that the vessel has a circular cross-section and there is no background. Thus the profiles are characterized by the radius and the location of the center. Shmueli uses a stochastic approach to model vessel continuity.

Some authors have developed algorithms for the reconstruction of the vessel cross-sections from two orthogonal projections [16]. They use some heuristic technique to find the vessel boundaries and to remove the background from each projection, and then they reconstruct the cross-sections in the following way. They assume that the cross-section can be represented by a matrix of 0's and 1's, and that the projections are proportional to the row and column sums of the matrix. Since it is well known that the matrix can not be reconstructed uniquely from the two sums, their reconstruction algorithm minimizes a cost criterion that reflects the

fact that adjacent slices must be similar.

The problem with this approach is that, in addition to the fact that the cross-sections cannot be reconstructed from the two projections, the algorithm assumes that the vessel projections can be isolated from the background. We have already discussed the problems with the estimation of boundaries and background.

### 1.3 Scope of the Thesis

In this thesis we present a modeling approach to estimate the dimensions of the coronary arteries from their x-ray projections. The idea is the following. We fit a model to the x-ray image and obtain the desired vessel dimensions from the estimated model parameters, instead of relying on direct boundary estimates based on local extrema of first or second derivatives.

We develop a two-dimensional model of a rectangular section of the angiogram that contains a single vessel. Our model accounts for the structure of the background, as well as distortions introduced by the imaging system. The desired vessel dimensions, that is, the diameter and cross-sectional area at each point along the vessel, can be obtained easily from the model parameters.

The vessel component of the projection is derived from a simple three dimensional model of the vessel. The vessel is assumed to be a tube with elliptical cross-sections. The background is modeled by a low order two-dimensional polynomial. The model takes into account the continuity of both the vessel and the background. In addition to the two-dimensional model of a section of the angiogram, we derive a one-dimensional model of the densitometric profiles of lines crossing the vessel. This model can also be used to obtain the diameter and cross-sectional area at each point along the vessel, even though it does not use the continuity of the vessel and the background.

The main difference with Shmueli's model is the addition of the background.

Shmueli's model assumes a flat background and therefore cannot even be applied to coronary angiograms. Also Shmueli's model of vessel continuity is stochastic. The model presented in this thesis is deterministic.

The parameters of the model are deterministic and we obtain the maximum likelihood estimates, which is equivalent to finding the model that best fits the data in the least squares sense. The estimation of the model parameters is a non-linear problem. We developed an iterative algorithm to estimate the parameters. The computational requirements for the one-dimensional algorithm are reasonable, even though they are considerably greater than the slope methods. The two-dimensional algorithm requires much more computation than the one-dimensional approach.

We test the algorithms on three types of data. The first type is computer generated data. It provides the opportunity to test the algorithms under the assumption that the model is valid and to compare them with the current methods. Second, the algorithms are tested on x-rays of contrast-medium-filled cylindrical phantoms. Since the true vessel dimensions are known, this set of data gives us the opportunity to test the model of the imaging system. Finally, the algorithms are tested on real coronary angiograms. In this case the true vessel dimensions are not known. Thus this set of experiments can only lead to qualitative conclusions. In the first part of our experiments we compare the performance of this one-dimensional model to the slope approaches. We then compare the performance of the one-dimensional model with that of the two-dimensional model.

Our results indicate that both the one-dimensional and the two-dimensional algorithm have better performance than the conventional slope approaches. This is because the modeling approach uses all the information in the projection image to estimate the model parameters. The slope approaches use only the slope information at the sides of the vessel to determine the vessel boundaries and get an estimate of the background. We also show that the two-dimensional algorithm is more robust to non-white noise in the background than the one-dimensional algorithm.

## 1.4 Summary and Notation

The thesis is organized as follows. The parametric model approach for the detection of coronary artery dimensions is presented in chapter 2. The computation of the model parameters is discussed in chapter 3. In chapter 4 we compare the modeling approach to the slope methods. The two versions of the modeling approach are compared in chapter 5. The conclusions of the thesis are summarized in chapter 6.

Throughout the thesis we will use parentheses to denote a continuous function  $f(\cdot)$  and brackets to denote a discrete function  $f[\cdot]$ . We will use bold face lower case letters to denote a vector  $\mathbf{x}$ .

## Chapter 2

### Coronary Angiogram Model

The radiographic imaging chain includes the following stages, shown in figure 2.1. The object is illuminated by the x-ray source into the image intensifier. A cine-camera records the output of the image intensifier on 35mm film. Each frame is optically magnified and digitized by a vidicon camera/digitizer.

First we will develop a model for the coronary angiogram under the assumption of a perfect imaging system. That is, the x-ray tube is an ideal point source emitting a monoenergetic x-ray beam, the image intensifier introduces no distortions, the film characteristic curve is linear, there is no film grain noise, and the output of the system is a continuous image. Later we will extend our model to take into consideration the more significant distortions of the imaging system.

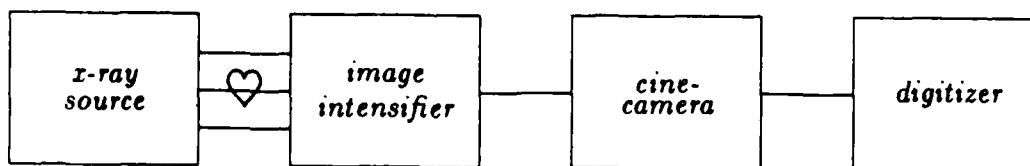


Figure 2.1: Imaging System

## 2.1 Perfect Imaging System

The analysis of the x-ray images is based on the Lambert-Beer law [23]. According to this law, a monoenergetic x-ray beam with input intensity  $I_0$  photons passing through a length  $z$  of material gives an output intensity of

$$I = I_0 e^{-\mu z} \quad (2.1)$$

The attenuation coefficient  $\mu$  depends on the energy of the x-ray beam and the type of material it passes through. In the case of the human body, the attenuation coefficient  $\mu(x, y, z)$  is a function of position, and the simple  $\mu z$  product becomes a line integral. Thus the output intensity is also a function of position

$$I(x, y) = I_0(x, y) e^{-\int \mu(x, y, z) dz} \quad (2.2)$$

The projection  $P(x, y)$  that we see in an x-ray image is actually the following quantity [25]

$$P(x, y) = -\ln \frac{I(x, y)}{I_0(x, y)} = \int \mu(x, y, z) dz \quad (2.3)$$

Thus the x-ray image is the line-integral projection of the attenuation coefficients. The x-ray beam passing through the human body encounters three types of material: tissue, bones, and contrast agent (iodine) which has been injected into the blood vessels. Thus

$$P(x, y) = \int_I \mu_I(x, y, z) dz + \int_T \mu_T(x, y, z) dz + \int_B \mu_B(x, y, z) dz \quad (2.4)$$

where  $\mu_I(x, y, z)$  is the attenuation coefficient of iodine, and the corresponding integral is over the iodine sections along the line parallel to the z-axis at  $(x, y)$ . The other two integrals are similarly defined. If we assume that iodine is uniformly distributed inside the vessel, and thus the attenuation coefficient is constant in the iodine sections, then we have

$$P(x, y) = \mu_I l_I(x, y) + \int_b \mu_b(x, y, z) dz \quad (2.5)$$

where  $l_I(x, y)$  is the thickness of the blood vessel (iodine) along the line parallel to the  $z$ -axis at  $(x, y)$  of the body, and the integral is the combination of the tissue and bone terms of equation (2.4). Thus the projection consists of two terms, the vessel term and the background term, and equation (2.5) can be written as

$$P(x, y) = v(x, y) + b(x, y) \quad (2.6)$$

The attenuation coefficient of the contrast agent is substantially higher than the other two, and that is why we can see the vessels.

Assuming this perfect image processing system we will develop a model for the x-ray image. In particular, we will develop a model for the vessel component and a model for the background component. The background model will be for a small rectangular section of the image around the vessel.

## 2.2 Two-Dimensional Vessel Model

In this section we will develop a two-dimensional model for the vessel component  $v(x, y)$  of equation (2.6). We will do this by considering a model for the three-dimensional vessel and from this deriving the model of its two-dimensional projection on the x-ray film.

We consider the following model for the three-dimensional vessel. We assume that the vessel is continuous and has elliptical cross-sections. Then it can be described by a continuous multi-dimensional function, each point of which is a vector containing the coordinates of the axis and the parameters characterizing the elliptical cross-section perpendicular to the axis at the point. This kind of object is usually referred to as a generalized cone or cylinder [2]. Figure 2.2 shows an example of such a cylinder and its line-integral projection.

This model is clearly too simple to match the actual vessel exactly. The model is pretty close to the healthy vessels, but it deviates significantly from the obstructed vessels. As we pointed out in the introduction, the shape of a cross-section at an

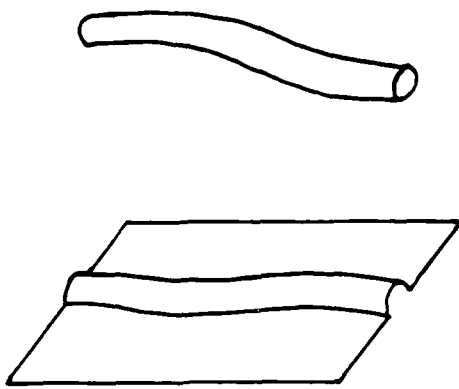


Figure 2.2: Generalized Cylinder and Its Projection

obstruction can be irregular in shape. The model is simple so that we can estimate its parameters from only one projection. The hope is that even when the model is crude, we can still get good estimates of the true vessel parameters, such as the diameter and cross-sectional area.

A slice of a cylinder with an elliptical cross-section is always an ellipse. Thus, if the vessel is continuous and its parameters are slowly varying, then the slices of the vessel are ellipses. Now, look at a plane perpendicular to the x-ray image which slices the vessel, and consider the line-integral projection of the vessel along that plane. The elliptical vessel cross-section and its projection are shown in figure 2.3 in solid lines.

An ellipse is described by the following parameters: the major and minor axes, the angle of rotation, and the coordinates of its center. If the axes have lengths  $2a$  and  $2b$ , the angle of rotation is  $\theta$ , and the center of the ellipse is located at  $(c_x, c_y)$ , then the equation of the ellipse is

$$\frac{(s - c_x) \cos\theta + (t - c_y) \sin\theta}{a^2} + \frac{-(s - c_x) \sin\theta + (t - c_y) \cos\theta}{b^2} = 1 \quad (2.7)$$

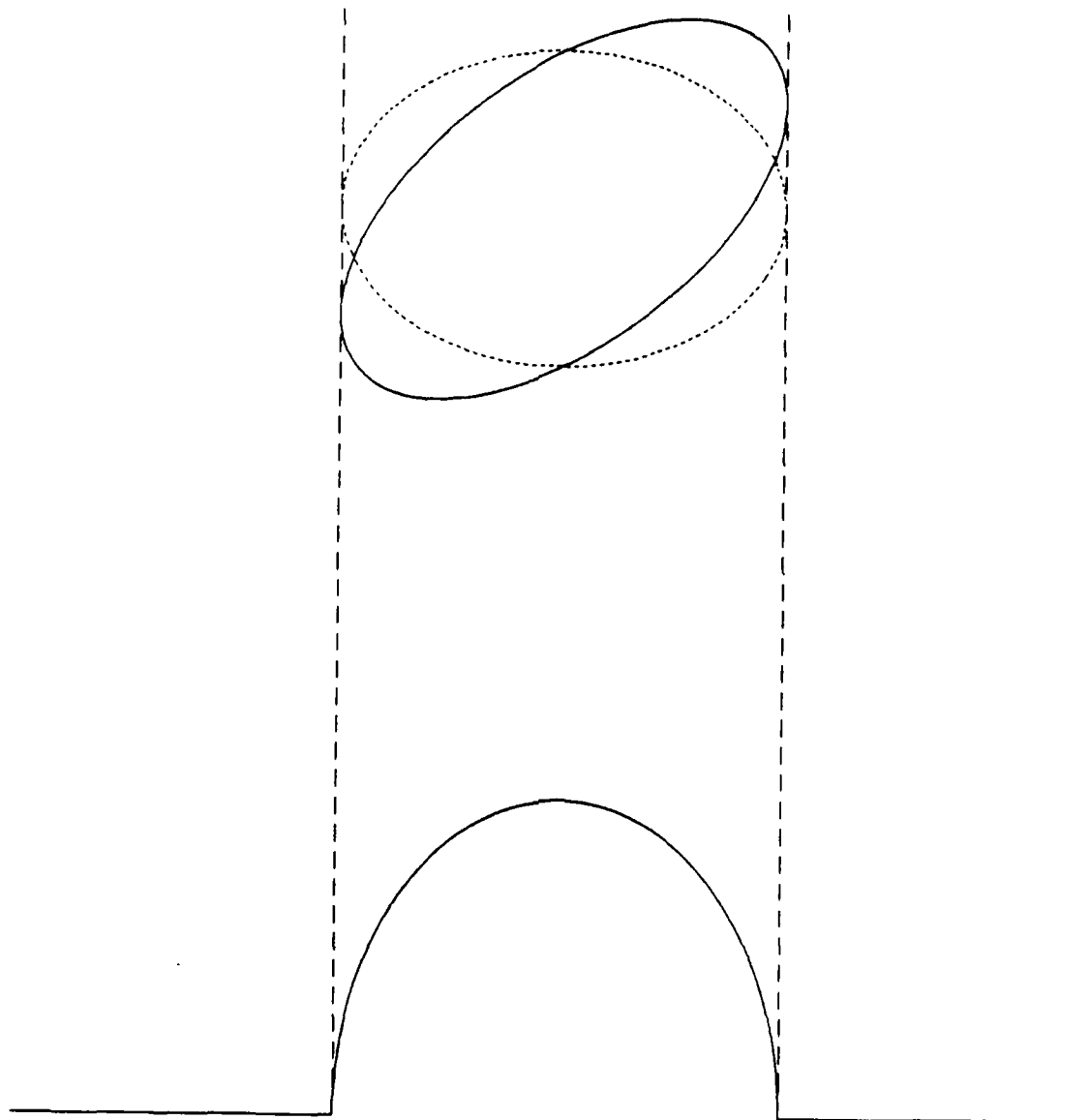


Figure 2.3: Ellipse and Its Line Integral Projection

and its projection is given by

$$p(t) = \begin{cases} \frac{2ab}{r^2} \sqrt{r^2 - (t - c_t)^2}, & \text{if } |t - c_t| \leq r \\ 0, & \text{otherwise} \end{cases} \quad (2.8)$$

where  $r^2 = b^2 \cos^2 \theta + a^2 \sin^2 \theta$ .

It is easy to see that this ellipse has the same projection as an ellipse with axes  $\hat{a} = ab/r$  and  $\hat{b} = r$  and  $\theta = 0$ . The new ellipse is shown in figure 2.3 in dotted line. This shows that, as we mentioned earlier, it is impossible to recover the exact shape of the cross-section from one projection. However, the area of the two ellipses is the same and is given by

$$\text{area} = \pi ab = \pi \hat{a} \hat{b} \quad (2.9)$$

which is also equal to the integral of the projection.

In fact, if we express the projection of an ellipse in terms of the parameters  $r$ ,  $\alpha$ , and  $c$  as follows,

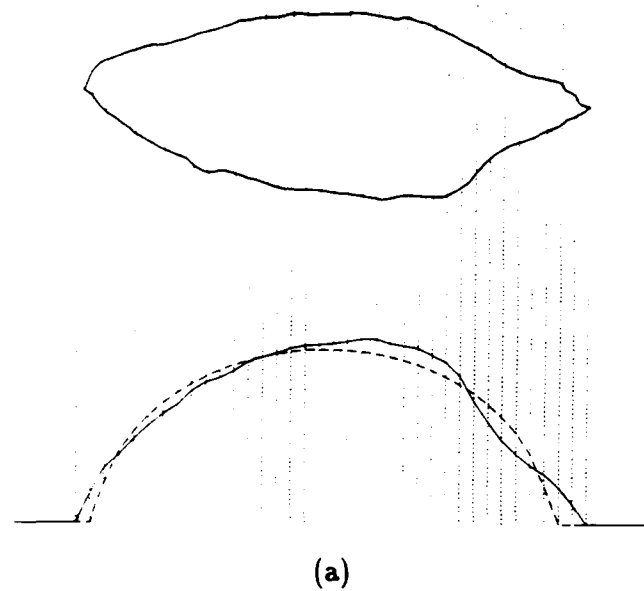
$$v(t) = \begin{cases} 2\alpha \sqrt{r^2 - (t - c)^2}, & \text{if } |t - c| \leq r \\ 0, & \text{otherwise} \end{cases} \quad (2.10)$$

then these parameters can be recovered from the projection. The area of the cross-section is given by

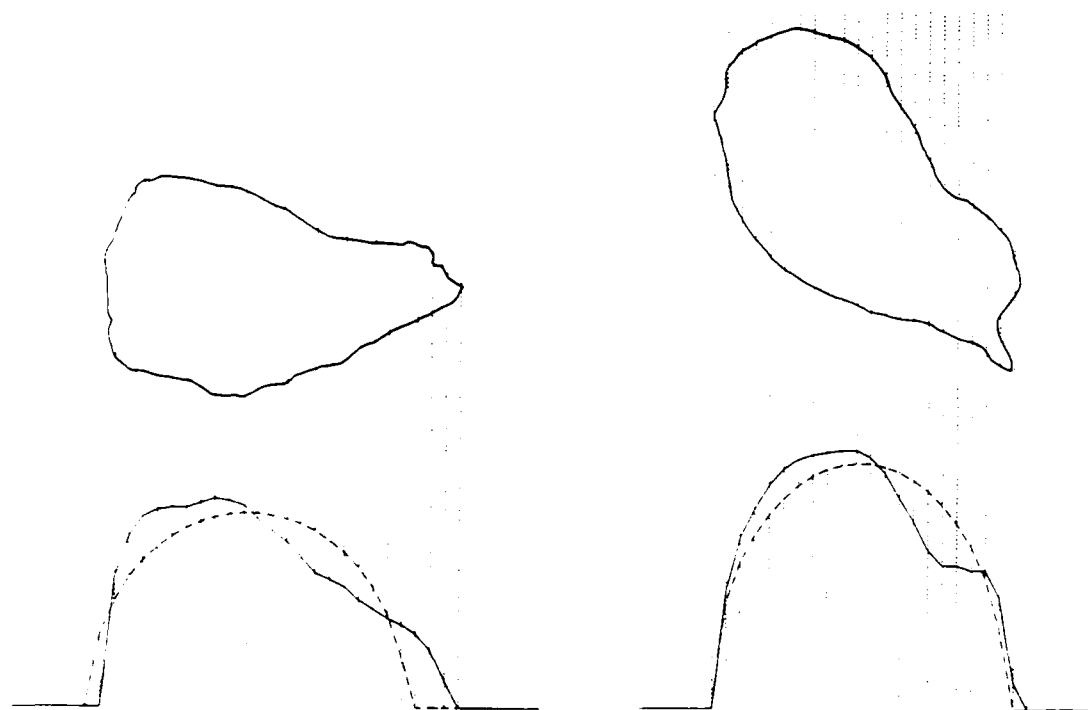
$$\text{area} = \pi \alpha r^2 \quad (2.11)$$

Thus two quantities that we can get from one projection are the area of the cross-section, and its diameter  $2r$ , which is equal to the diameter of the ellipse which has the given projection and an axis parallel to the projection plane.

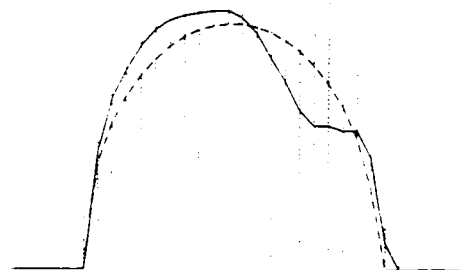
As an illustration of the potential errors in the obstructed sections of the vessels we considered several cross-sections obtained from post-mortem analyses. Figure 2.4 shows the line-integral projections of the cross-sections of figure 1.2. Also shown in this figure are the elliptical models fitted to these projections. The model parameters are chosen so that the sum of squares of the difference between the actual projection and the model is minimized. Table 2.1 displays the percent error between the



(a)



(b)



(c)

Figure 2.4: Line-Integral Projections of Stenotic Vessel Cross-Sections

estimated and actual parameters. We see that, even though the cross-sections are far from being elliptical, we get good estimates of the cross-sectional area. The diameter estimates are not as good, but the exact values are not very useful, since they depend on the angle of projection.

So far we have derived a model for a cross-section of the vessel projection. We must now extend this to a two-dimensional model for the projection of the vessel on the x-ray image. Consider the profiles of the projection that are perpendicular to the axis of the projected vessel. According to our discussion, each profile is described by an equation of the form of (2.10). Let  $c_1(q)$  and  $c_2(q)$  be the functions that specify the x- and y-coordinates of the axis of the projected vessel, and let the functions  $r(q)$  and  $\alpha(q)$  describe the corresponding perpendicular profiles. These functions describe the vessel component  $v(x, y)$  of the perfect projection model of equation (2.6). The continuity of the vessel implies that the functions  $r(q)$ ,  $\alpha(q)$ ,  $c_1(q)$  and  $c_2(q)$  are continuous. We will assume that they are cubic splines.

Splines are piecewise polynomial functions of degree  $n$  that are connected together (at points called nodes) so as to have  $n - 1$  continuous derivatives [8,10]. They represent nice smooth curves which are convenient to use in many practical applications. One important property of splines is that they are good approximations of functions whose behavior in one region is totally unrelated to their behavior in another region. The behavior of polynomials, as well as most other mathematical functions, is just the opposite. Their behavior in any small region affects their

Cross-section	Diameter	Area
(a)	-11%	-4%
(b)	-12%	-3%
(c)	-6%	-1%

Table 2.1: Error in Estimation of Stenotic Vessel Parameters

behavior everywhere [21].

The continuity and flexibility of the cubic splines are the main reasons that make them a good choice for modeling the spatial continuity of the vessel. In addition, their flexibility can be adjusted by changing the spacing of the nodes. The choice of the spline parameters does not depend on the length of the vessel. The importance of these properties will become more evident in the next chapter, where we discuss the estimation of the model parameters.

We showed that from the projection parameters we can obtain the area of the vertical cross-sections of the three-dimensional vessel, but not the exact cross-sections. It should also be obvious that we cannot recover the exact three-dimensional location of the vessel either.

Here we should note that the parameter  $\alpha$  is also proportional to the attenuation coefficient  $\mu_I$  of the contrast agent, i.e. to the iodine concentration. Assuming that the iodine concentration is constant along the vessel section of interest, estimates of the vessel model parameters will give us relative estimates of the true vessel parameters.

## 2.3 Two-Dimensional Model of Background

In this section we will introduce a two-dimensional model for the background component  $b(x, y)$  of equation (2.6). We will model the background in a rectangular section of the image around the vessel.

We assume that the objects in the background, that is tissue and bones, are much bigger than the blood vessels. Therefore the density of their two-dimensional projection is slowly varying, and we can model it by a low order two-dimensional polynomial  $p(x, y)$ . A two-dimensional polynomial is a function of the form

$$p(x, y) = \sum_{i=0}^Q \sum_{j=0}^{Q-i} a_{ij} x^i y^j \quad (2.12)$$

If we assume that  $a_{i,Q-i} \neq 0$  for some  $0 \leq i \leq Q$ , then the degree of the polynomial is  $Q$  and the order is  $Q + 1$ . Given that the image occupies a rectangular area  $[a, b] \times [c, d]$  of the plane, we can express this function in terms of an orthonormal basis  $\psi_{ij}(x, y)$

$$p(x, y) = \sum_{i=0}^Q \sum_{j=0}^{Q-i} d_{ij} \psi_{ij}(x, y) \quad (2.13)$$

where  $\psi_{ij}(x, y) = \phi_i^x(x) \phi_j^y(y)$  and  $\phi_i^x(x), \phi_j^y(y)$  are the orthonormal bases for the one-dimensional polynomials in the intervals  $[a, b]$  and  $[c, d]$  respectively [8].

Polynomials, especially of low order, are very smooth functions. They are unable to take on sharp bends followed by relatively flat behavior. Thus their properties are very different from those of the vessel projection, which varies drastically in the direction perpendicular to its axis. This makes the models of the background and vessel relatively independent, and thus makes simultaneous estimation of their parameters from one projection possible.

The model for the perfect projection of equation (2.6) now becomes

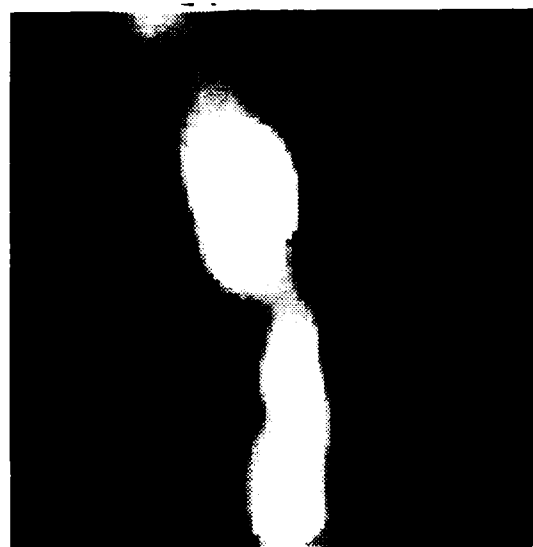
$$P(x, y) = v(x, y) + p(x, y) \quad (2.14)$$

An example of the perfect model and its components is shown in figure 2.5. Figure 2.5(a) depicts the vessel model. A fifth degree polynomial modeling the background is shown in figure 2.5(b). The sum of the two components is shown in figure 2.5(c).

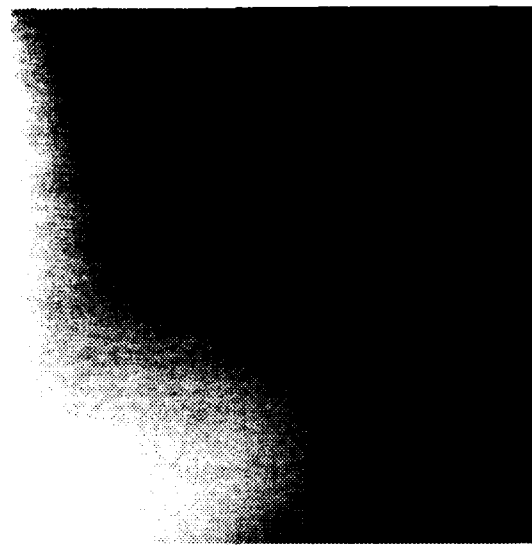
We must now extend our model to take into consideration the distortions of the imaging system.

## 2.4 Model of Imaging Process

In the development of our model we assume that the x-ray tube is an ideal point source and that the radiation is monoenergetic. We model the blurring that is introduced at various stages in the imaging process as convolution of the perfect



(a) Vessel Model



(b) Background Model



(c) Vessel Plus Background Model

Figure 2.5: Perfect Model

projection image with a two-dimensional point spread function  $g(x, y)$ . In this thesis we will assume that the point spread function is Gaussian with covariance matrix  $S$ , but any other smooth bell shaped function can be used. In fact, the x-ray pattern in the plane of the film (intensity domain) is the convolution of the x-ray pattern that enters the image intensifier with the point spread function of the film-screen combination [22]. Tests with vessel phantom x-rays show that it is reasonable to model this, as well as other effects, as convolution in the density domain. We model degradations such as quantum mottle noise, digitization noise, and film grain noise, as white noise  $w(x, y)$  added to the projection image.

According to this model the optical density distribution of the radiographic image is the following

$$f(x, y) = P(x, y) * g(x, y) + w(x, y) \quad (2.15)$$

where  $P(x, y)$  is the perfect projection of equation (2.14),  $g(x, y)$  is the Gaussian blurring function, and  $w(x, y)$  is the additive noise. Substituting for  $P(x, y)$  we obtain the density at each point of the image section

$$f(x, y) = [v(x, y) + p(x, y)] * g(x, y) + w(x, y) \quad (2.16)$$

where

$f(x, y)$  : observed densitometric profile

$v(x, y)$  : vessel model

$p(x, y)$  : polynomial model of background tissue and bones

$g(x, y)$  : Gaussian point spread function

$w(x, y)$  : white noise

The convolution of an  $n$ -th order polynomial with a smooth function like a Gaussian is also an  $n$ -th order polynomial, i.e.

$$p(x, y) * g(x, y) = p'(x, y) \quad (2.17)$$

where  $p'(x, y)$  is a polynomial of the same order as  $p(x, y)$ . Substituting equation (2.17) into (2.16) we have

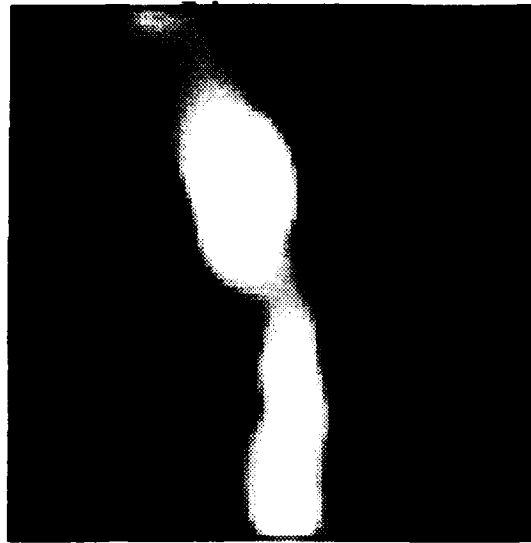
$$f(x, y) = v(x, y) * g(x, y) + p'(x, y) + w(x, y) \quad (2.18)$$

This is the two-dimensional model of the coronary angiogram that we will use in this thesis. An example of the model and its components is shown in figure 2.6. Figure 2.6(a) depicts the vessel model of figure 2.5(a) convolved with a Gaussian point spread function. The sum of this component and the background of figure 2.5(b) is shown in figure 2.6(b). When white noise is added to the above we obtain figure 2.6(c).

The radiographic imaging process is much more complicated, however. There are many distortions introduced because of the x-ray tube characteristics (it is not an ideal point source), the image intensifier distortions (pincushion), the film characteristics, and the fact that the radiation is not monoenergetic. A section of an actual coronary angiogram is shown in figure 2.7. The model parameters for figure 2.6 were obtained from this angiogram.

Our model is only a crude model and cannot account for all the distortions introduced during the imaging process. However, the more important distortions are either accounted for by the model (blurring, noise), or can be corrected independently. Nonlinear geometric distortions, such as the pincushion distortion, are important only if absolute measurements are to be derived from the angiograms. Kooijman *et al.* [15] present a technique for correcting this type of distortions. Our model assumes a linear relationship between the density of the radiographic image and the thickness of the contrast medium. When this is not true, linearity can be restored by the techniques we mentioned in the introduction [30,31,17]. A comparison of the model of figure 2.6(c) with the actual angiogram of figure 2.7 indicates that our model is reasonable despite the simplifications.

As we discussed in the introduction, the x-rays of contrast-medium-filled cylindrical phantoms give us an opportunity to test our model. Since the vessel phantoms



(a)  $v(x, y) * g(x, y)$



(b)  $v(x, y) * g(x, y) + p'(x, y)$



(c)  $v(x, y) * g(x, y) + p'(x, y) + n(x, y)$

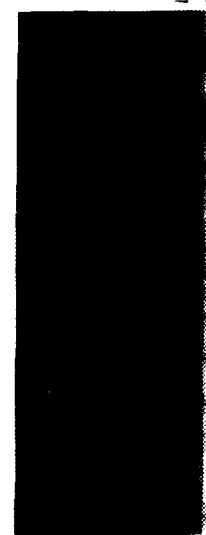
Figure 2.6: Two-Dimensional Model



Figure 2.7: Real Angiogram

are straight with circular cross-sections, and the background is flat, they both fit the model, and thus we can use their x-rays to check the model of the imaging process. A section of a vessel phantom x-ray is shown in figure 2.8(a). The model for this phantom is shown in figure 2.8(b). The vessel component is shown in figure 2.8(c), and the difference between the original and the vessel component is shown in figure 2.8(d). Examining this figure we find no traces of the vessel. This indicates that the model of the imaging process is adequate for this case.

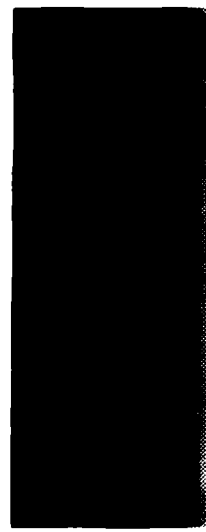
Further justification for our model will be provided in the experiments of the following chapters.



(a) Original



(b) Model



(c) Vessel Component



(d) Model Minus Vessel Component

Figure 2.8: Comparison of Vessel Phantom and Model

## 2.5 One-Dimensional Model

As we saw in the introduction, all of the current algorithms estimate the vessel parameters by analyzing the densitometric profiles of the lines perpendicular to the vessel. A model of these one-dimensional profiles can be developed based on assumptions similar to those of the previous sections. Modeling the perpendicular profiles would be an obvious first step towards a modeling approach to our problem. It is therefore of interest to compare it to the two-dimensional model. It also offers a computational advantage over the two-dimensional approach, as we will see in the next chapter. The advantage of the two-dimensional approach is that it uses the spatial continuity of both the vessel and the background.

The model for the one-dimensional profiles can be derived similarly to the two-dimensional model. Consider the profile of a line crossing the vessel projection at some angle, not necessarily a right angle. The one-dimensional analog of equation (2.16) is the following

$$f(t) = [v(t) + p(t)] * g(t) + w(t) \quad (2.19)$$

where

$f(t)$  : observed densitometric profile

$v(t)$  : vessel model

$p(t)$  : polynomial model of background tissue and bones

$g(t)$  : Gaussian point spread function

$w(t)$  : white noise

The model for a cross-section of the vessel projection  $v(t)$  was derived in section 2.2, and is given by equation (2.10)

$$v(t) = \begin{cases} 2\alpha\sqrt{r^2 - (t - c)^2}, & \text{if } |t - c| \leq r \\ 0, & \text{otherwise} \end{cases}$$

The background is modeled as a low-order polynomial  $p(t)$  of the form

$$p(t) = \sum_{i=0}^N d_i \phi_i(t) \quad (2.20)$$

where  $\phi_i(t)$  is the orthonormal basis for the one-dimensional polynomials in an interval  $[a, b]$ . It is easy to see that a slice of a two-dimensional polynomial is a one-dimensional polynomial of the same degree. Thus the vessel and background components are consistent with the two-dimensional model. Blurring is modeled as convolution of the perfect projection  $v(t) + p(t)$  with a Gaussian point spread function  $g(t)$ , with standard deviation  $s$ . However, it is not true that a slice of the convolution of two functions is the convolution of their slices. Blurring in all directions cannot be equivalent to blurring along one direction. Thus equation (2.19) is an analog of equation (2.16), but cannot be obtained as a slice of equation (2.16). The final component of the model is additive white noise  $w(t)$ , with standard deviation  $\sigma$ .

Similarly to the two-dimensional case the convolution of an  $n$ -th order polynomial with a smooth function like a Gaussian is also an  $n$ -th order polynomial, i.e.

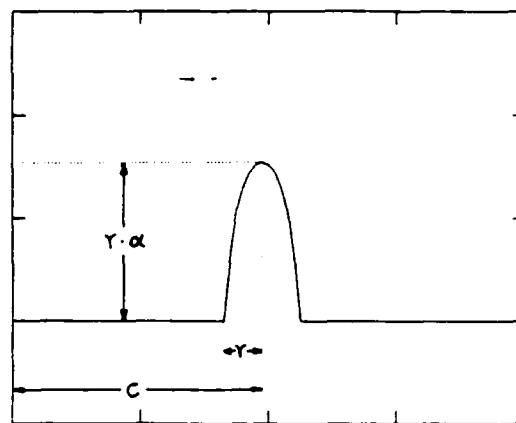
$$p(t) * g(t) = p'(t) \quad (2.21)$$

where  $p'(t)$  is a polynomial of the same order as  $p(t)$ . Substituting equation (2.21) into (2.19) we have

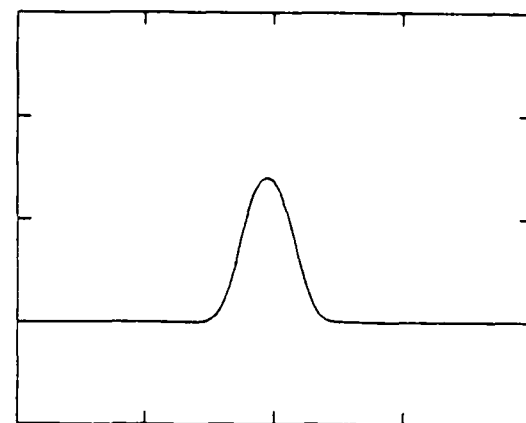
$$f(t) = v(t) * g(t) + p'(t) + w(t) \quad (2.22)$$

This is the one-dimensional model of the densitometric profile along a line crossing the coronary artery. We should note here that the profile does not have to be perpendicular to the vessel for the model to be valid. The reason for which we are interested in the perpendicular profiles is that it is their parameters that are useful for our problem.

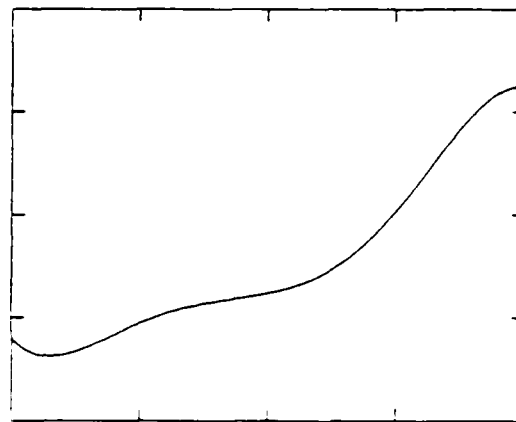
The model and its components are shown in figure 2.9. Figure 2.9(a) depicts the vessel model. This model convolved with a Gaussian point spread function is shown in figure 2.9(b), while a fifth degree polynomial modeling the background is in figure 2.9(c). The sum of the components of figures 2.9(b) and 2.9(c) is in figure 2.9(d). When white noise is added to the above we obtain figure 2.9(e).



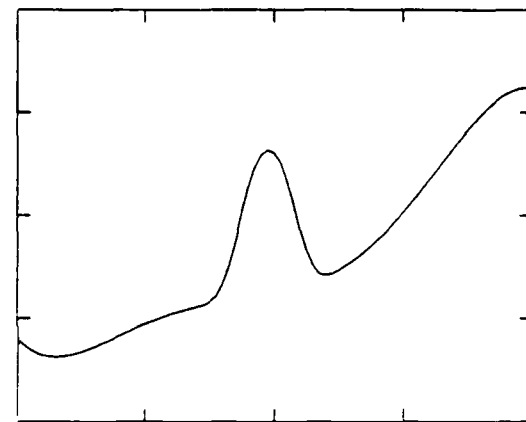
(a)  $v(t)$



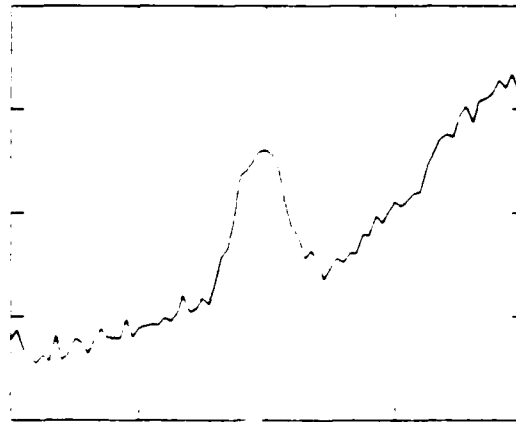
(b)  $v(t) * g(t)$



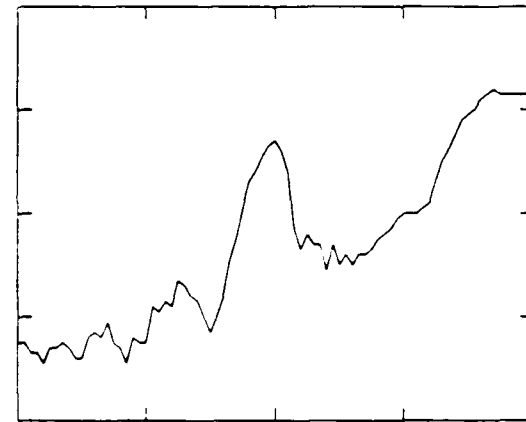
(c)  $p'(t)$



(d)  $v(t) * g(t) + p'(t)$



(e)  $v(t) * g(t) + p'(t) + n(t)$



(f) Real Profile

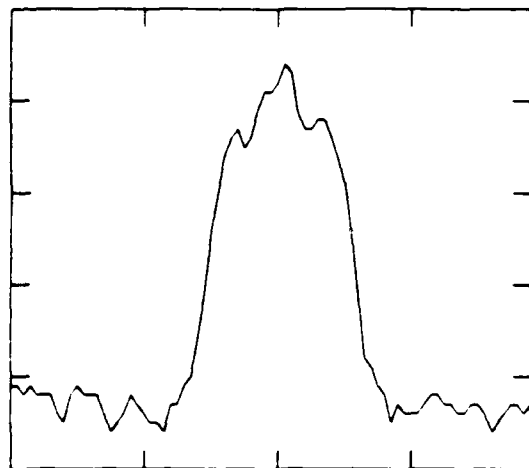
Figure 2.9: One-Dimensional Model

An example of an actual vessel profile, taken from a real angiogram, is shown in figure 2.9(f).<sup>7</sup> The parameters for the model were obtained from this profile. A comparison of the model of figure 2.9(e) with the actual angiogram of figure 2.9(f) indicates that our model is reasonable despite the simplifications.

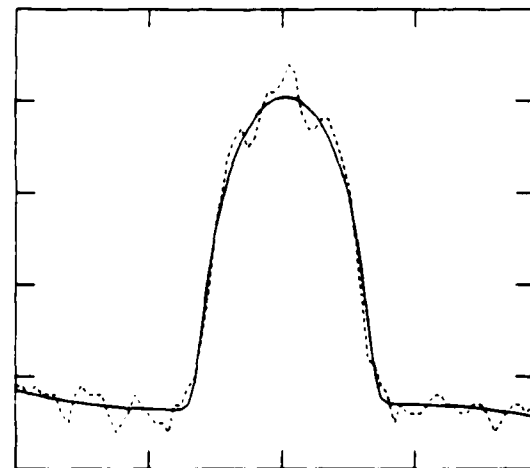
As we did in the two-dimensional case, we can test the model of the imaging process on x-rays of contrast-medium-filled cylindrical phantoms. A profile of a vessel phantom x-ray is shown in figure 2.10(a). The model for this phantom is shown in solid line in figure 2.10(b); the original is shown in dotted line for comparison. We see that there is a close match between the two. The vessel component is shown in figure 2.10(c), and figure 2.10(d) shows the original minus the vessel component. No trace of the vessel is evident in this subtracted profile. This indicates that the model of the imaging process is adequate for this case.

The two-dimensional vessel projections can be described by the parameter functions  $r(q)$  and  $\alpha(q)$ , as well as the corresponding axis coordinate functions  $c_1(q)$  and  $c_2(q)$ .

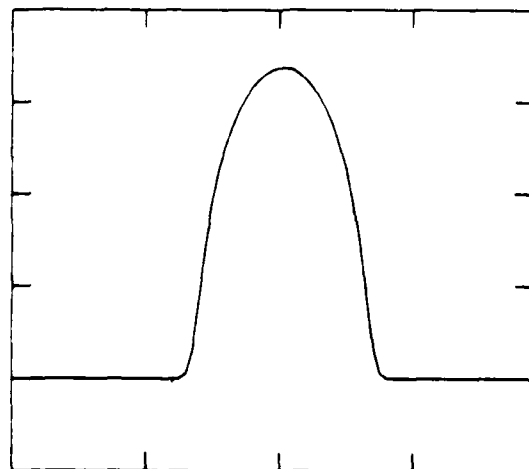
The difference between the one-dimensional and the two-dimensional model is that the latter takes into consideration the continuity of both the vessel and the background. Also the blurring is in all directions, rather than along a linear profile. In the next chapter we will consider a simple heuristic (and suboptimal) way to incorporate the vessel continuity into the one-dimensional model. But there does not appear to be a reasonable way to use the continuity of the background.



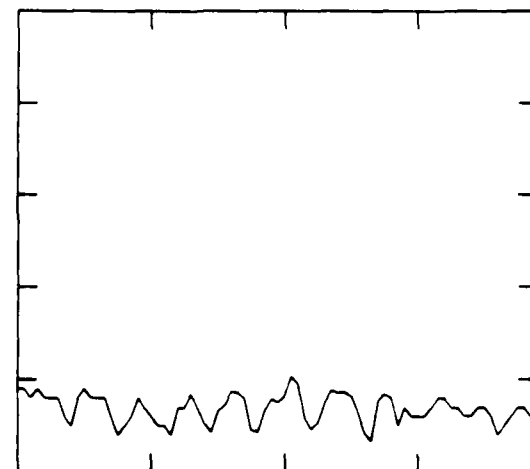
(a) Original



(b) Model



(c) Vessel Component



(d) Model Minus Vessel Component

Figure 2.10: Comparison of Vessel Phantom and Model

# Chapter 3

## Estimation of Model Parameters

In the previous chapter we introduced parametric models for a rectangular section of the coronary angiogram and a linear profile of the angiogram crossing the artery. In this chapter we will look at the problem of estimating the parameters of these models from the angiograms. The unknown parameters of the model are assumed to be nonrandom. In this case, the problem can be formulated as a maximum likelihood (ML) estimation problem.

According to our model the observations (coronary angiogram) are described by equations (2.18) and (2.22), which we will combine into

$$f(\mathbf{x}) = f_0(\mathbf{x}; \mathbf{a}) + w(\mathbf{x}) \quad (3.1)$$

where  $f_0(\mathbf{x}; \mathbf{a}) = v(\mathbf{x}) * g(\mathbf{x}) + p'(\mathbf{x})$ . The vector  $\mathbf{x}$  stands for the coordinate pair  $x, y$  in the two-dimensional model, or the coordinate  $t$  in the one-dimensional model, and  $\mathbf{a}$  is the vector of all the model parameters. The parametric function  $f_0$  is deterministic, and the noise  $w$  is stationary, white, Gaussian, with variance  $\sigma^2$ .

In the Gaussian case the ML estimate  $\hat{\mathbf{a}}$  is the value of  $\mathbf{a}$  which maximizes the likelihood function [34]

$$\Lambda[f(\mathbf{x}); \mathbf{a}] = -\frac{1}{\sigma^2} \int \{f(\mathbf{x}) - f_0(\mathbf{x}; \mathbf{a})\}^2 d\mathbf{x} \quad (3.2)$$

Differentiating with respect to  $\mathbf{a}$ , we find that the ML estimate satisfies the equation

$$\int \{f(\mathbf{x}) - f_0(\mathbf{x}; \mathbf{a})\} \frac{\partial f_0(\mathbf{x}; \mathbf{a})}{\partial \mathbf{a}} d\mathbf{x} = 0 \quad (3.3)$$

The covariance matrix of the ML estimate  $\hat{\mathbf{a}}$  satisfies the Cramer-Rao inequality

$$E\{(\hat{\mathbf{a}} - \mathbf{a})(\hat{\mathbf{a}} - \mathbf{a})^T\} \geq \mathbf{J}^{-1}(\mathbf{a}) \quad (3.4)$$

where

$$\mathbf{J}_{ij}(\mathbf{a}) = -\frac{2}{\sigma^2} \int \left( \frac{\partial f_0(\mathbf{x}; \mathbf{a})}{\partial a_i} \right) \left( \frac{\partial f_0(\mathbf{x}; \mathbf{a})}{\partial a_j} \right) d\mathbf{x} \quad (3.5)$$

The ML equation (3.3) is nonlinear and cannot be solved analytically. Instead, we will consider iterative procedures to minimize equation (3.2).

So far we assumed all parameters to be continuous. The coronary angiogram is digitized, however. That is, we are given samples of the image on a Cartesian grid, and the above integrals become summations. In the following sections we will look at algorithms for finding the maximum likelihood estimates of the parameters of each model. We will consider the one-dimensional model first, because it is simpler and leads into a better understanding of the two-dimensional case.

### 3.1 One-Dimensional Model

The one-dimensional model of a densitometric profile along a line crossing the coronary artery is described by the discrete version of equation (2.22)

$$f[t] = v[t] * g[t] + p'[t] + w[t] \quad (3.6)$$

The vessel component is described by the location of the center  $c$ , the radius  $r$ , and the parameter  $\alpha$ . The background component is characterized by the coefficients of the polynomial  $d_i$ , the Gaussian point spread function is characterized by the standard deviation  $s$ , and the noise by the standard deviation  $\sigma$ .

The choice of the degree of the polynomial that models the background depends on the width of the vessel relative to the width of the profile we are analyzing and

the variation in the background. We want the models of the background and vessel to be independent, that is, the polynomial must fit the background component not the vessel component. Thus we must choose a polynomial that fits the background with as low a degree as possible. Reasonable values for the degree of the polynomial are three and five (odd degrees seem to have better behavior than even degrees).

We can find the maximum likelihood estimates of the parameters characterizing our model by maximizing the discrete version of the likelihood function of equation (3.2), or equivalently minimizing

$$\Lambda'(\mathbf{a}) = \sum_{t=0}^N \{f[t] - f_0[t; \mathbf{a}]\}^2 \quad (3.7)$$

where

$$f_0[t; \mathbf{a}] = v[t] * g[t] + p'[t] \quad (3.8)$$

over all parameter vectors  $\mathbf{a}$ .

Minimizing  $\Lambda'$  over the parameters  $c$ ,  $r$ ,  $\alpha$ ,  $s$ , and the coefficients of the polynomial is the same as fitting a polynomial to all possible functions

$$f[t] - v[t] * g[t] \quad (3.9)$$

and selecting the one that results in the minimum mean square error. This means that we must search over all possible values of the unknown parameters. However, taking the structure of the problem into consideration, we can proceed with the search in a systematic way.

We assume that the variance of the Gaussian point spread function can be estimated independently of the other parameters. The above minimization is done as follows. First we find crude estimates of the parameters  $c$ ,  $r$ , and  $\alpha$ . The estimates of the previous profile should be adequate because of the spatial continuity of the vessel. At the first profile we can use some heuristic technique to determine the estimates. Once we have the initial estimates, we need only search in the neighborhood of these estimates. To reduce the search even further, we decouple

the search over  $c$ , and the parameters  $r$  and  $\alpha$ . This is possible, because of the bell shaped vessel and its model. It should be obvious that with a reasonable estimate of  $r$  and  $\alpha$ , optimization over  $c$  will give a value pretty close to the optimal. We can then optimize over  $r$  and  $\alpha$ . A possible strategy for the minimization is the following:

1. Get initial estimates for  $c$ ,  $r$ , and  $\alpha$ . Pick search increment.
2. Update  $c$  estimate by searching over a neighborhood of  $c$ .
3. Update  $r$  and  $\alpha$  estimates by searching over their neighborhoods.
4. Reduce search increment.
5. Update  $c$  estimate by searching over a neighborhood of  $c$ .
6. Update  $r$  and  $\alpha$  estimates by searching over their neighborhoods.
7. Repeat last 2 steps if necessary.

It also follows from the shape of the vessel that the likelihood function is locally convex. As we move away from the optimum value of one of the parameters (in either direction) the value of the error should keep increasing. Thus we need only search in the direction of decreasing error.

For each value of  $c$ ,  $r$ , and  $\alpha$  we have to evaluate the function in equation (3.9) and fit a polynomial to this function. The main computation in each function evaluation is the convolution with the Gaussian. For the convolution the number of computations is of the order of  $N \log_2 N$ . The polynomial fit is of the order of  $QN$  computations, where  $Q$  is the degree of the polynomial. We will refer to the above operations as one iteration. Thus the number of computations per iteration is proportional to

$$\text{computations/iteration} \sim N \log_2 N + QN \quad (3.10)$$

Exact knowledge of the covariance matrix of the Gaussian point spread function

is not crucial in the optimization procedure. In fact, if we assumed that there is no blurring, we would still get good estimates of the parameters.

So far we considered only one profile of a line crossing the vessel. In order to apply the algorithm to a segment of the vessel, we need a starting point and the approximate direction of the vessel. We assume that they can be provided by the angiographer. We can then apply the algorithm to the profiles perpendicular to the given direction. The output of the algorithm consists of the sequences of estimated parameters  $r[q]$ ,  $\alpha[q]$ , and  $c[q]$ . From  $c[q]$  and the direction of the vessel we get the axis coordinates  $c_1[q]$  and  $c_2[q]$ .

However, the objective is to estimate the dimensions of the cross-sections that are perpendicular to the vessel axis. Using the initial estimate of the axis coordinates, we can obtain the perpendicular profiles at each point and get new parameter estimates. This procedure can be repeated iteratively. Usually one additional iteration is enough. At each point along the vessel the perpendicular direction is computed by fitting a cubic spline to the estimated  $c[q]$  sequence, and computing its slope. The density of the linear profile is obtained by simple linear interpolation.

Thus far the one-dimensional algorithm does not use the spatial continuity of the vessel, except for determining initial estimates for the parameters of each profile from the previous one. In order to have a fair comparison of the one-dimensional approach with the two-dimensional approach, we will consider a simple heuristic way to use the continuity of vessel. This is to smooth the vessel parameter sequences after they are estimated, by fitting splines to them. This approach will be useful in chapter 5, where we will compare the one-dimensional approach to the two-dimensional approach.

## 3.2 Two-Dimensional Model

We consider a small rectangular section of the angiogram ( $N \times M$ , where usually  $M = N = 50\text{-}80$  pixels). We assume that there is a single isolated vessel in this section of the angiogram. We assume that the angiographer can pick such a section. Physical considerations dictate that the vessel must cross the section borders in two places at most. It may terminate (total obstruction) before it reaches another part of the border. For simplicity we assume that the vessel does not cross the two vertical sides of the section. This is not a limiting assumption, since the angiographer can pick the section so that it is true.

The two-dimensional model of the rectangular section is described by the discrete version of equation (2.18)

$$f[x, y] = v[x, y] * g[x, y] + p'[x, y] + w[x, y] \quad (3.11)$$

The vessel component is described by the sequence of axis coordinates  $c_1[q]$  and  $c_2[q]$ , and the sequences of the corresponding radii  $r[q]$  and alphas  $\alpha[q]$ . The background component is characterized by the coefficients of the polynomial  $d_{ij}$ . Finally, the Gaussian point spread function is characterized by the covariance matrix  $S$ , and the noise by the variance  $\sigma^2$ .

We assume that the variation in the direction of the axis of the vessel is limited so that the vessel crosses each horizontal line at most once. This is a reasonable assumption, given the fact that we look at a short segment of the vessel. In this case we can choose  $c_2[q] = q$ . Thus, the total number of parameters describing the vessel is  $3N$ , where  $N$  is the vertical dimension of the image section. However, since we have assumed that these sequences are samples of continuous cubic splines, they can also be described by the spline parameters. The location of the nodes determines how smooth the splines are. Thus we can choose the spline parameters to reflect our *a priori* knowledge of the vessel smoothness. Of course the choice also depends on the magnification of the x-ray.

The choice of the degree of the two-dimensional polynomial that models the background depends on the size of the vessel relative to the image section we are analyzing and the variation in the background. As we argued in the one-dimensional case, we want the models of the background and vessel to be independent, and thus we must choose a polynomial that fits the background with as low a degree as possible. Reasonable values for the degree of the polynomial are three and five (odd degrees seem to have better behavior than even degrees).

We can find the maximum likelihood estimates of the parameters characterizing our model by maximizing the discrete version of the likelihood function of equation (3.2), or equivalently minimizing

$$\Lambda'(\mathbf{a}) = \sum_{x=0}^N \sum_{y=0}^M \{f[x, y] - f_0[x, y; \mathbf{a}]\}^2 \quad (3.12)$$

where

$$f_0[x, y; \mathbf{a}] = v[x, y] * g[x, y] + p'[x, y] \quad (3.13)$$

over all parameter vectors  $\mathbf{a}$ .

Minimizing  $\Lambda'$  over the model parameters is the same as fitting a polynomial to all possible functions

$$f[x, y] - v[x, y] * g[x, y] \quad (3.14)$$

and selecting the one that results in the minimum mean square error. This means that we must do an exhaustive search through all possible sequences  $c_1[q]$ ,  $r[q]$  and  $\alpha[q]$ . This is a formidable task. However, as we did in the one-dimensional case, we can take the structure of the problem into consideration and proceed with the search in a systematic way.

We assume that the covariance matrix of the Gaussian point spread function can be estimated independently of the other parameters. The above minimization is done as follows. First we determine a crude estimate of the sequences  $c_1[q]$ ,  $r[q]$ , and  $\alpha[q]$ , and then we consider perturbations around these estimates. For this we can use the estimates obtained by some heuristic technique, or the one-dimensional

approach presented in the previous section. We can also obtain initial estimates of the vessel directly by a technique described in section 3.3.

To simplify the search, we decouple the search over the sequences  $c_1[q]$ ,  $r[q]$  and  $\alpha[q]$ . As we argued in the one-dimensional case, this is possible because of the bell shaped vessel and its model. It also follows from the shape of the vessel that the likelihood function is convex for perturbations of a sequence around a point. One possible strategy for the minimization is the following:

1. Get initial estimate of the sequences  $c_1[q]$ ,  $r[q]$ , and  $\alpha[q]$ .
2. Optimize over a set of rough perturbations around the current  $r[q]$  estimates.
3. Optimize over a set of rough perturbations around the current  $c_1[q]$  estimates.
4. Optimize over a set of fine perturbations around the current  $r[q]$  estimates.
5. Optimize over a set of fine perturbations around the current  $c_1[q]$  estimates.
6. Consider tradeoff in perturbations around the  $r[q]$  estimates and  $\alpha[q]$  estimates.
7. Repeat last 3 steps if necessary.

At each step, we consider a set of perturbations around a parameter sequence. For example consider the sequence  $r[q]$  shown in figure 3.1. The solid line shows the original sequence, and the dotted line shows a typical perturbation of step 4. The perturbations are made at  $K$  evenly spaced points, shown by the vertical dashed lines in the figure. As can be seen in the picture, the perturbations are local. Our ability to do this follows from the flexibility of the splines. As we discussed in chapter 2, the splines can be changed locally without affecting their global behavior. On the other hand the properties of the splines guarantee that these changes are smooth. Thus the properties of the splines insure that spatial continuity constrains the vessel parameters only locally.

Another property of the splines that is important here is the fact that their flexibility can be adjusted by changing the spacing of the nodes. Figure 3.2 shows

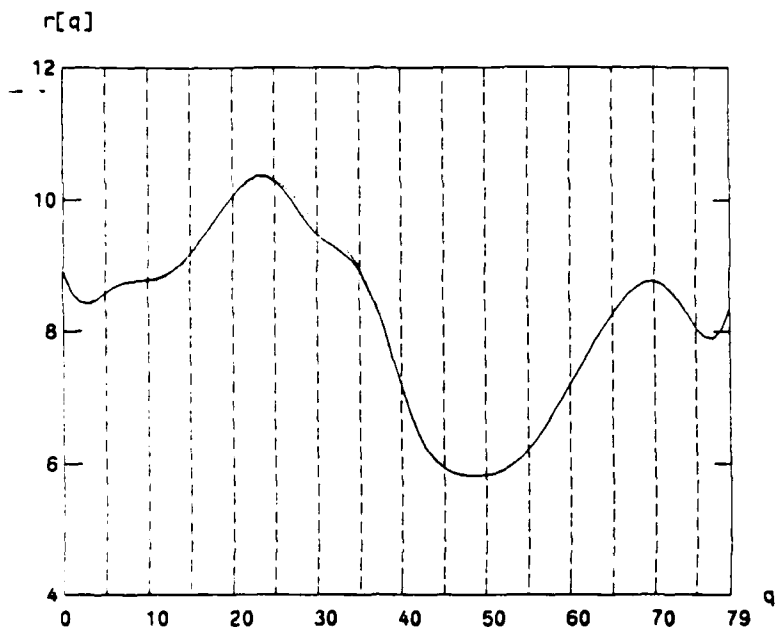


Figure 3.1: Example of Fine Perturbation

an example of a perturbation at an earlier stage in the optimization procedure (step 2). Here the spacing of the nodes is wider and the spline less flexible. As a result the spacing of the points at which the perturbations are made need not be as dense.

For each perturbation we have to evaluate the function in equation (3.14) and fit a polynomial to this function. Each function evaluation involves the computation of the vessel component, the convolution with a Gaussian, and a subtraction. The number of computations for the vessel evaluation is of the order of  $N^2$  (from now on we set  $M = N$ ). For the convolution the number of computations is of the order of  $N^2 \log_2 N$ .<sup>1</sup> Finally, the polynomial fit is of the order of  $\frac{1}{2}Q^2 N^2$  computations, where  $Q$  is the degree of the polynomial. We will refer to the above cycle of computations as one iteration.

We observe that the computations are dominated by the convolution with the

<sup>1</sup> Actually the number of computations is of the order of  $N_1^2 \log_2 N_1$ , where  $N_1 \geq N + N_g$  and  $N_g \times N_g$  is the support of the Gaussian point spread function.

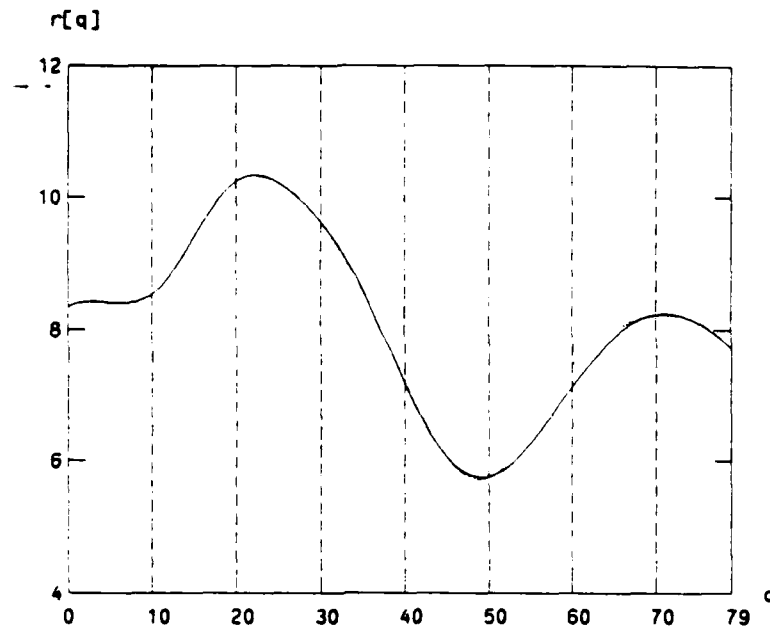


Figure 3.2: Example of Crude Perturbation

Gaussian point spread function and the polynomial fitting. Considering only these two operations, the number of computations per iteration is proportional to

$$\text{computations/iteration} \sim N^2 \log_2 N + \frac{1}{2} Q^2 N^2 \quad (3.15)$$

Exact knowledge of the covariance matrix of the Gaussian point spread function is not crucial in the optimization procedure. In fact we can assume that there is no blurring until the very last optimization stage, without significantly affecting the procedure. Thus we can save a considerable amount of computation, since the number of operations per iteration becomes proportional to  $\frac{1}{2} Q^2 N^2$ .

### 3.2.1 Comparison With One-Dimensional Approach

In terms of computations, the advantage of the one-dimensional approach is that it optimizes the cross-section parameters of the vessel at each point independently of all others. Also, it only uses background information of one linear profile. The two-dimensional optimization is also done locally, but more than one cross-section is

involved at each point, as the algorithm takes the spatial continuity of the vessel into account. Also, it uses all of the background, and assumes blurring in all directions. Thus we expect the two-dimensional approach to require much more computation. This is indeed the case as demonstrated by the following crude comparison.

The number of computations at each step of the two-dimensional optimization procedure is proportional to  $K$ , the number of perturbation points, and the number of computations per iteration of equation (3.15). Thus the total number of computations is proportional to

$$\text{computations for 2D case} \sim K(N^2 \log_2 N + \frac{1}{2} Q^2 N^2) \quad (3.16)$$

The number of computations at each step of the one-dimensional optimization procedure is proportional to the number of computations per iteration of equation (3.10). But this is repeated for  $N$  profiles along the vessel. Thus the total number of computations is proportional to

$$\text{computations for 1D case} \sim N^2 \log_2 N + QN^2 \quad (3.17)$$

Assuming that everything else is the same, we can see that the two-dimensional approach is much more time consuming than the one-dimensional approach. In fact, the two-dimensional approach requires more computation than this simple comparison indicates, mainly because more iterations are needed. Finally, it should be obvious that both approaches involve much more computation than the slope methods, mainly because of the search involved in the optimization procedure.

### 3.3 Initial Vessel Estimate

The modeling approach presented in this thesis suggests a way to estimate the background from the angiogram without estimating the vessel parameters. At the same time we can get a rough estimate of the vessel in the section.

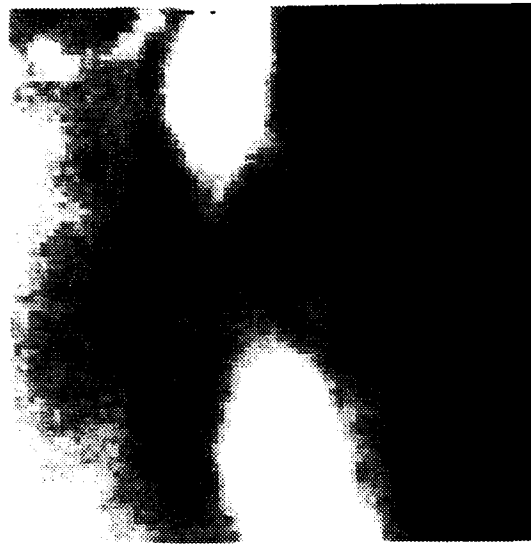
Consider a rectangular section of the coronary angiogram, containing one or more vessels. Assume that the background is slowly varying compared to the vessel profile, and thus can be modeled by a low order two-dimensional polynomial. This assumption is reasonable, as we discussed in the previous chapter, if the section of the angiogram to be analyzed is chosen properly. Also assume that the vessel profile is positive, which is always true. Now consider the following algorithm.

### **Algorithm: Background Estimation**

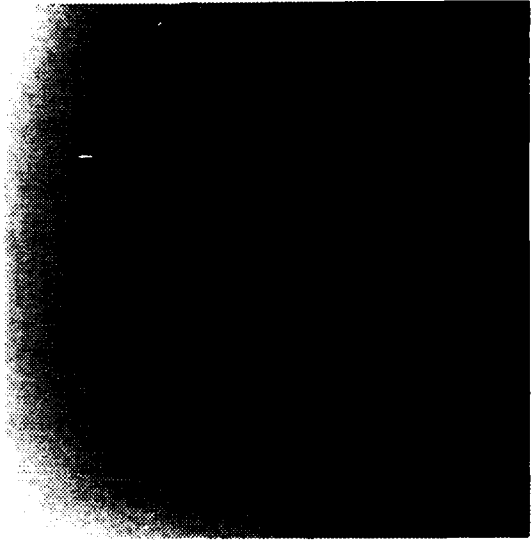
1. Fit a low order polynomial to the section, and compute the standard deviation.
2. Remove the points for which the error is greater than a given multiple of the standard deviation.
3. Fit a low order polynomial to the remaining points of the section, and compute the standard deviation [35].
4. Quit if there is no significant reduction in the standard deviation. Otherwise go back to step 2.

This algorithm has been observed to converge after a few iterations. The polynomial thus obtained is a good estimate of the background. The set of points that are removed in the process give a good initial estimate of the vessel after we use some simple neighborhood operations to remove isolated points due to noise in the background.

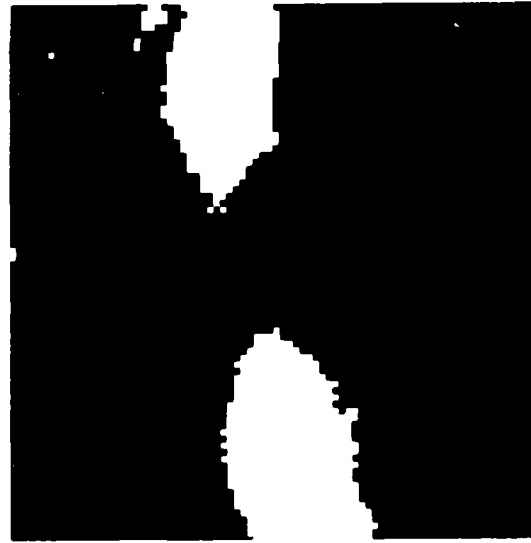
An example of this procedure is shown in figure 3.3. The original coronary angiogram section is shown in figure 3.3(a). After 3 iterations of algorithm 1, the background estimate is shown in figure 3.3(b). The degree of the background polynomial used in this example is 3, and the threshold used was 1.5 times the standard deviation. The set of points above the threshold are shown in figure 3.3(c). Figure 3.3(d) shows the points after removal of isolated points by simple neighborhood operations.



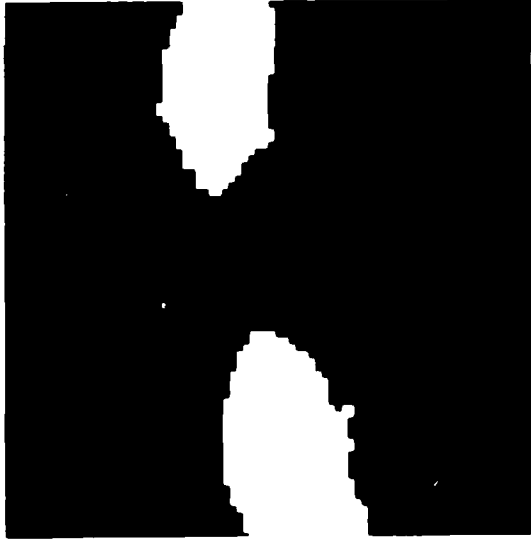
(a) Original Angiogram



(b) Background Estimate



(c) Points Above Threshold



(d) Vessel Estimate

Figure 3.3: Initial Estimate of Vessel

## Chapter 4

# Comparison of One-Dimensional Model With Slope Methods

In this chapter we examine the performance of the one-dimensional model and compare it to that of the slope methods, on which most current boundary detection methods are based. In our analysis we will consider each densitometric profile independently of the previous profiles, i.e., the spatial continuity of the vessel or the background (in the direction of the vessel) will not be taken into account. Our objective is to isolate the problem of accurately estimating the cross-sectional dimensions from one profile, from that of exploiting the spatial continuity of the vessel. The importance of vessel continuity will be examined in the following chapter.

The slope method we implemented in our examples is the following: at each point of the profile we fitted a second degree polynomial to a set of 7 adjacent points. The first and second derivative of the profile were estimated as the corresponding derivatives of the polynomial. The inflection points were identified as the points with maximum and minimum first derivative, and the knee points as the maxima of the second derivative. Variations of the above approach, as well as other approaches of estimating the profile derivatives, were tried with comparable or worse results.

The vessel diameter was obtained as the difference between the inflection or the

knee points. The cross-sectional area was obtained as the integral of the profile between the boundary points after the background had been estimated and subtracted. The background was estimated by computing the linear regression line through the boundary points.

We tested our algorithm on computer generated data (synthetic data), on x-rays of contrast-medium-filled cylindrical phantoms, and on real coronary angiograms. The first two cases are useful, because the results can be compared to the true vessel dimensions. The last case is useful as an illustration of application of the algorithms to actual coronary angiograms. The true dimensions are not known, so any conclusions we draw will be only qualitative.

In the phantom and coronary artery cases a sequence of images were recorded on 35mm film (cine-angiogram) and a single frame was selected by the angiographer. The analog image was optically magnified and digitized by a vidicon camera/digitizer interfaced to a Vax 11/780 computer. The grey level of each pixel was digitized to 256 levels. The scans were performed four times and averaged. The phantom x-rays were the same ones used by Spears *et al.* in [32]; the resolution was fixed at approximately 15 microns/pixel. The resolution for the real coronary angiograms varied from image to image. In the synthetic data case the grey level of each pixel was also digitized to 256 levels to be consistent with the x-ray data.

## 4.1 Synthetic Data

First we examine the performance of the model on synthetic data. The data were generated assuming the model is valid. A typical example of a synthetic densitometric profile is shown in figure 4.1. This profile is 80 pixels wide. The background is a fifth degree polynomial, obtained from a real angiogram profile. The vessel parameter values are  $c = 40$  pixels,  $r = 10$  pixels,  $\alpha = 2$ , and  $s = 1$  pixel. These parameters were chosen to correspond to vessel profiles of actual angiograms. Fig-

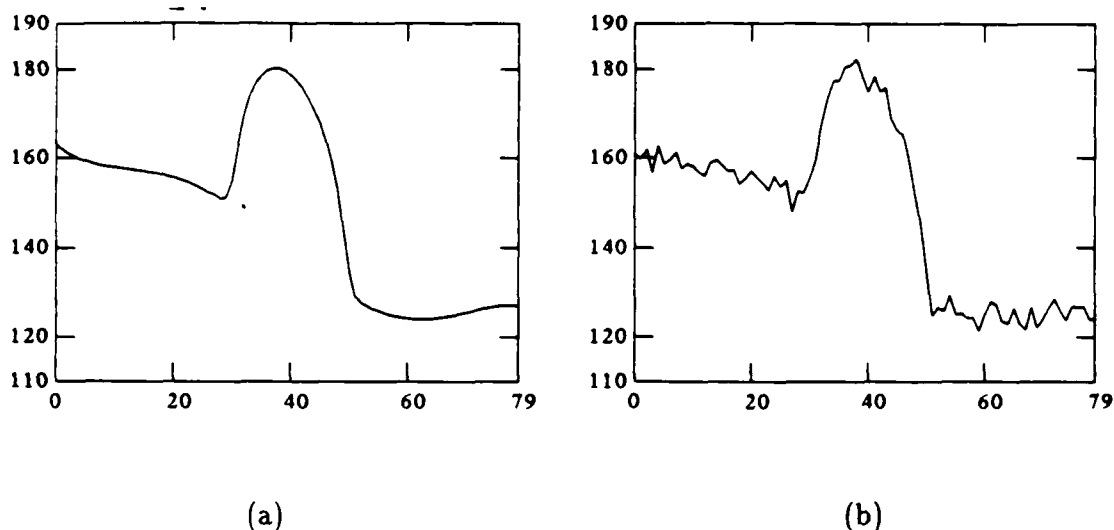


Figure 4.1: Synthetic Densitometric Profile

ures 4.1(a) and (b) show the profile before and after the noise was added. The standard deviation of the noise is  $\sigma = 2$ , which corresponds to signal to noise ratio of 19.6 dB.

We conducted a number of experiments to study the properties of the modeling approach and to compare them to the properties of the slope method. In particular, we investigated the behavior of the two approaches for different levels of noise, different vessel dimensions, and different image backgrounds. In each of the experiments we describe below, all the parameters (background,  $c$ ,  $r$ ,  $\alpha$ ,  $s$ , and noise variance) were fixed except one. We considered 80 noise samples, and estimated the vessel dimensions for each sample using the modeling approach and the slope methods. The radius and cross-sectional area estimates were averaged, and the standard deviation of the estimates was computed. The standard deviation of the estimates was normalized, that is, it was divided by the true value of the parameter being estimated (radius or area).

The degree of the polynomials used in the modeling approach was 5, the same as

that of the background polynomials of the synthetic data. In all of the experiments the model parameters were chosen to correspond to profiles of actual angiograms.

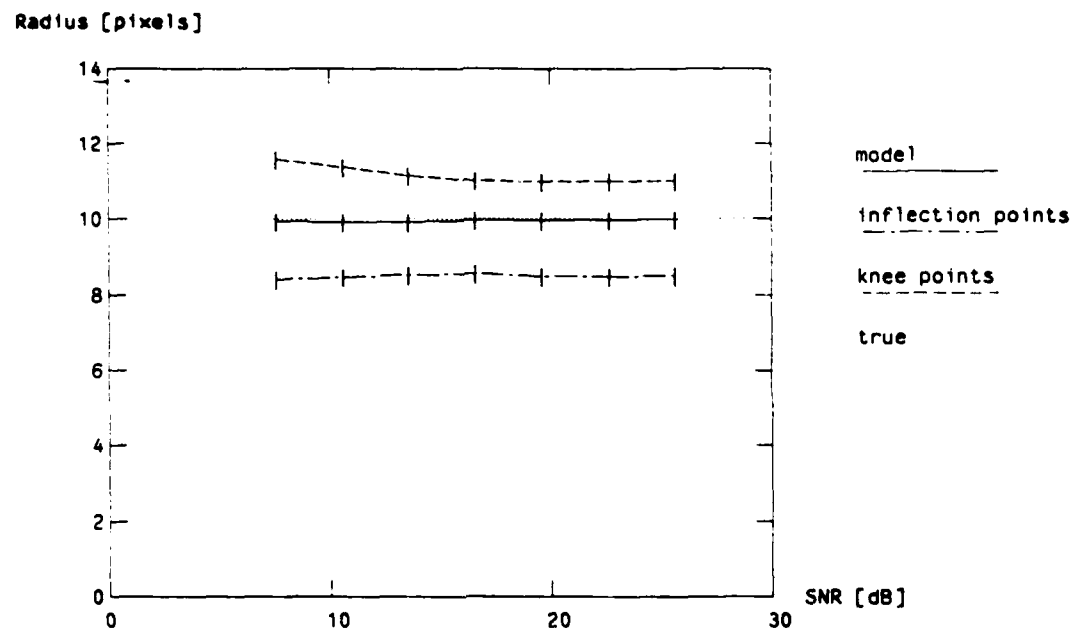
#### 4.1.1 Effect of Noise Level

For this experiment all the parameters were fixed except the noise level. The synthetic densitometric profile we used was that of figure 4.1(a). The vessel parameters were  $c = 40$  pixels,  $r = 10$  pixels,  $\alpha = 2$ , and  $s = 1$  pixel. To this profile we added 7 different levels of noise. For each noise level we considered 80 noise samples and estimated the vessel dimensions for each sample. The signal to noise ratio (SNR) is defined as follows:

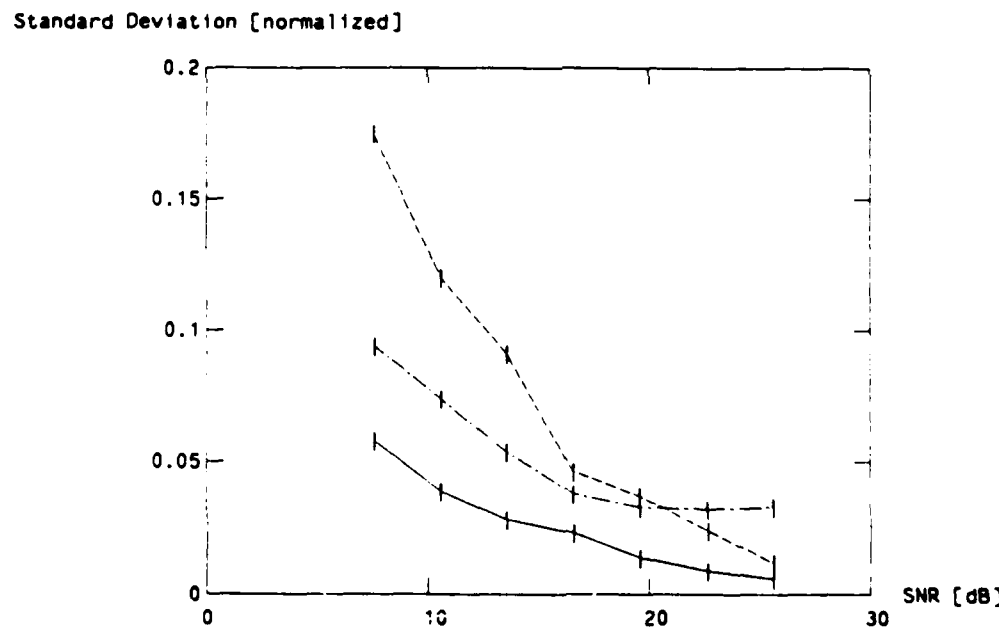
$$\text{SNR} = 10 \log_{10} \left( \frac{\text{signal variance}}{\text{noise variance}} \right) \quad (4.1)$$

The average of the radius estimates as a function of signal to noise ratio is shown in figure 4.2(a) and the normalized standard deviation is shown in figure 4.2(b). The solid line represents the model estimates, the dot-dashed line represents the corresponding results when the inflection points are found, and the dashed line represents the results for the knee points. The true radius is shown in dotted line. We observe that the inflection point method underestimates the vessel radius, while the knee point method overestimates it. This behavior is characteristic of such algorithms, and is consistent with previous results [32]. Note that for the signal to noise ratios considered, the average of the model estimates is roughly constant. The same is true for the inflection point estimates, but the average of the knee point estimates increases for low SNR's. As expected the standard deviation of the estimates is significantly higher in the slope methods.

The average of the area estimates as a function of signal to noise ratio is shown in figure 4.3(a) and the standard deviation is shown in figure 4.3(b). The solid line represents the model estimates, the dot-dashed line shows the inflection point estimates, and the dashed line shows the knee point estimates. The dotted line

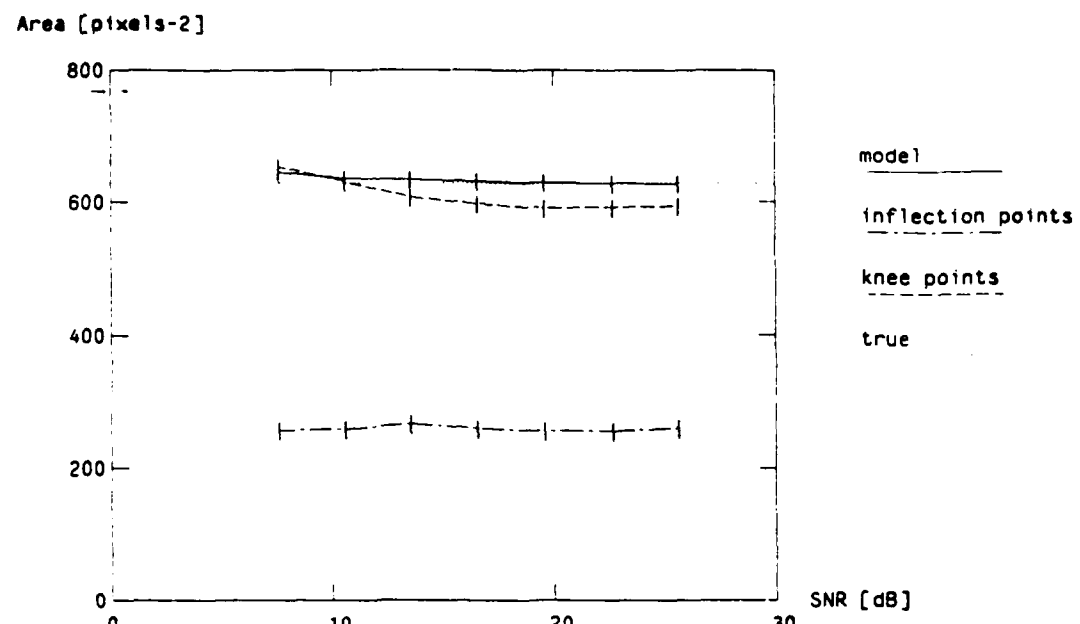


(a) Average of Radius Estimates

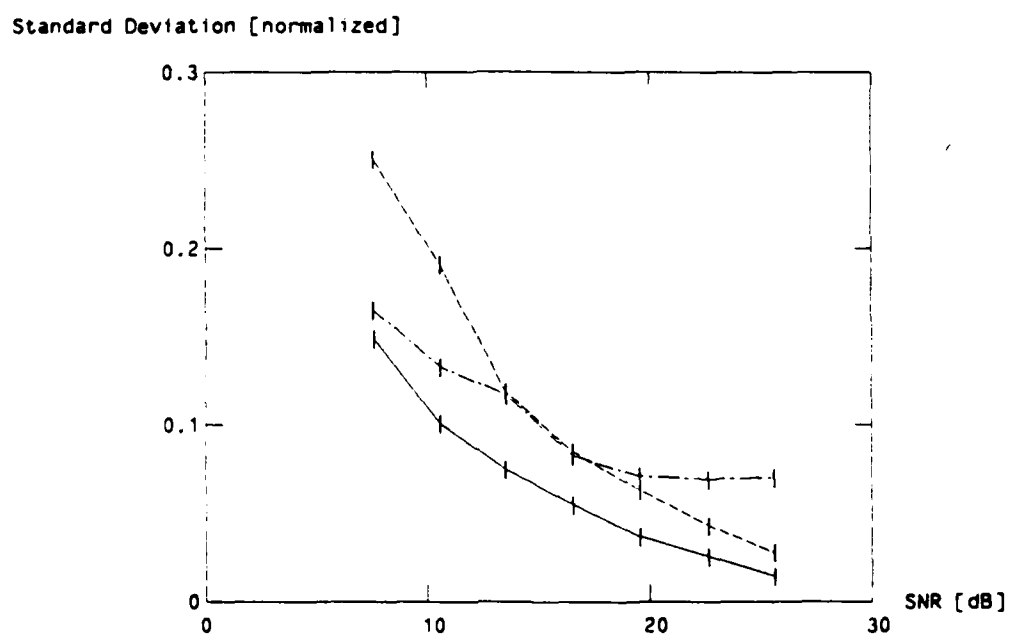


(b) Normalized Standard Deviation of Radius Estimates

Figure 4.2: Radius Estimation for Different SNR's



(a) Average of Area Estimates



(b) Normalized Standard Deviation of Area Estimates

Figure 4.3: Area Estimation for Different SNR's

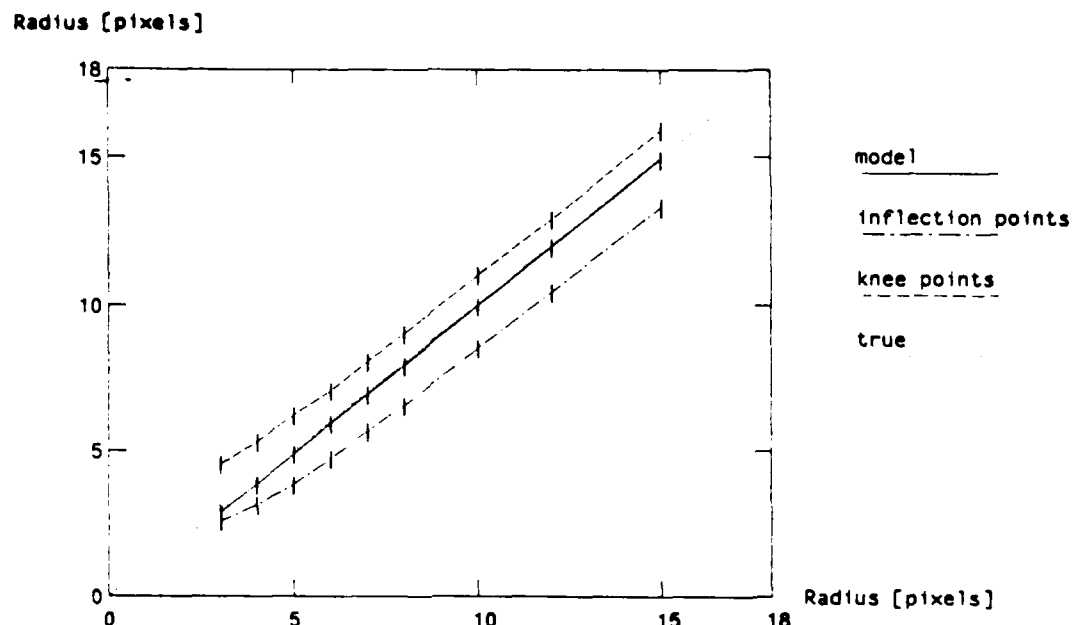
represents the true area. Here we observe that the knee point method slightly underestimates the area, but, more importantly, the estimate changes significantly with the signal to noise ratio. For the signal to noise ratios considered, the average of the model estimates is roughly constant. The inflection point method grossly underestimates the area. As a result, the usefulness of the inflection point area estimates is doubtful, but we include the results for completeness. The standard deviation of the slope approach estimates is higher than that of the model estimates.

#### 4.1.2 Effect of Vessel Radius

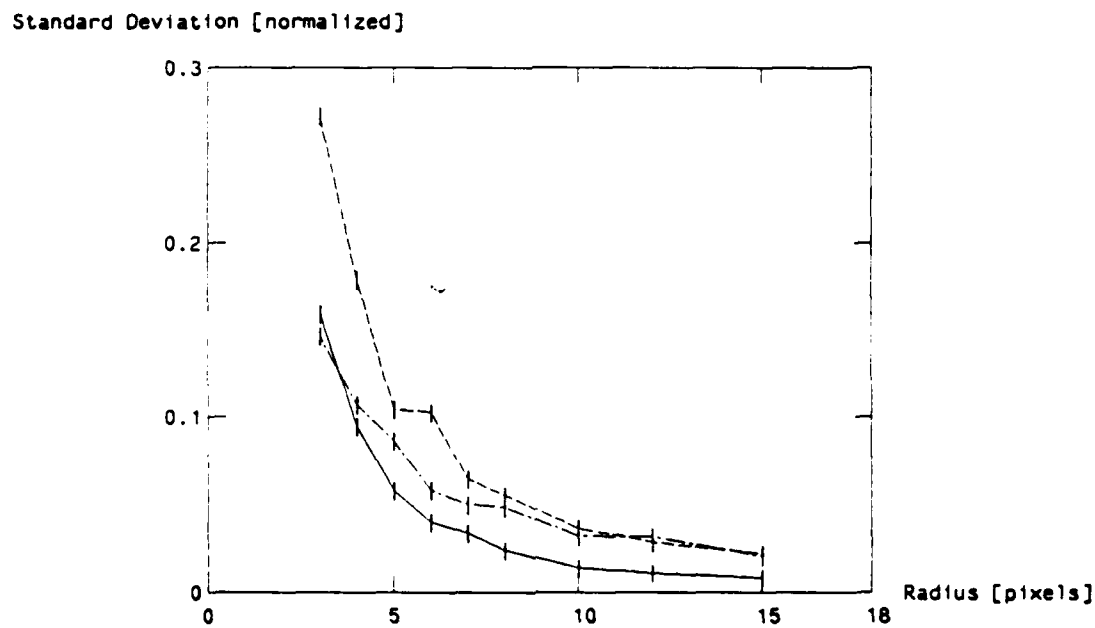
For this experiment all the parameters were fixed except the vessel radius. The vessel parameters were  $c = 40$  pixels,  $\alpha = 2$ , and  $s = 1$  pixel. The standard deviation of the noise was fixed at  $\sigma = 2$  (this corresponds to signal to noise ratio of 19.6 dB when  $r = 10$  pixels). The values of the radius were  $r = 3, 4, 5, 6, 7, 8, 10, 12, 15$  pixels. For each radius we considered 80 noise samples and estimated the vessel dimensions for each sample.

The average of the radius estimates as a function of radius is shown in figure 4.4(a) and the normalized standard deviation is shown in figure 4.4(b). The solid line represents the model estimates, the dot-dashed line represents the inflection point estimates, and the dashed line represents the knee point estimates. The true radii lie on the diagonal (dotted line). Observe that the inflection point method underestimates the vessel radius, and the knee point method overestimates it. The problem for the slope methods, however, is that the estimates lie on a line that does not pass through the origin. Moreover, the line curves up near the origin. This means that the relative radius estimates are biased, and thus can lead to significant errors in the determination of vessel obstruction. We also observe that the standard deviation of the slope approach estimates is higher.

The average of the area estimates as a function of area is shown in figure 4.5(a) and the normalized standard deviation is shown in figure 4.5(b). Both axes of

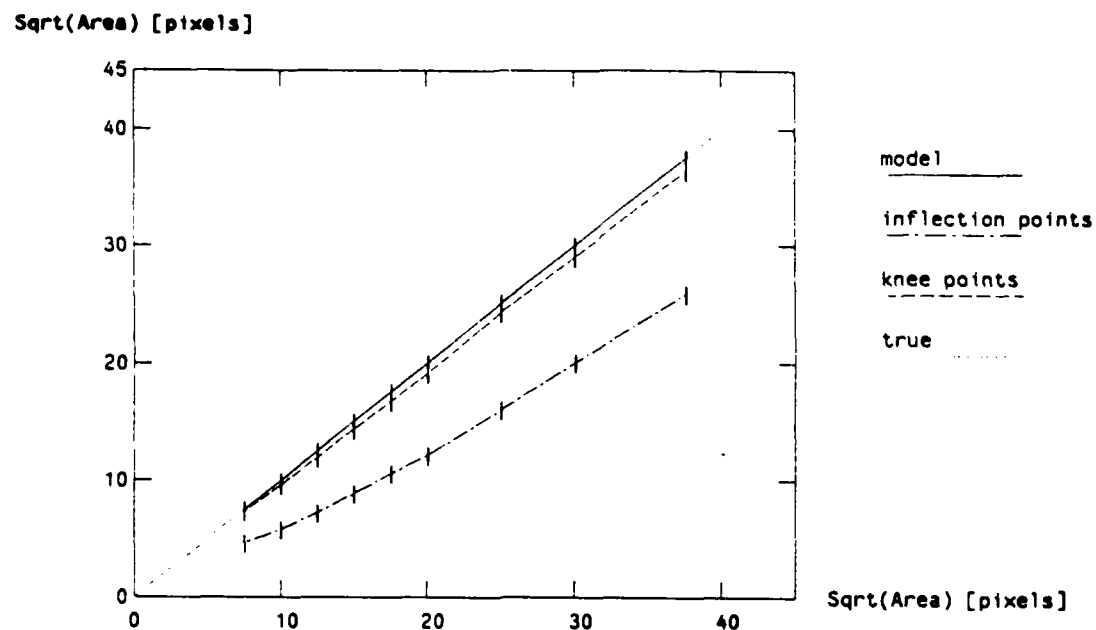


(a) Average of Radius Estimates

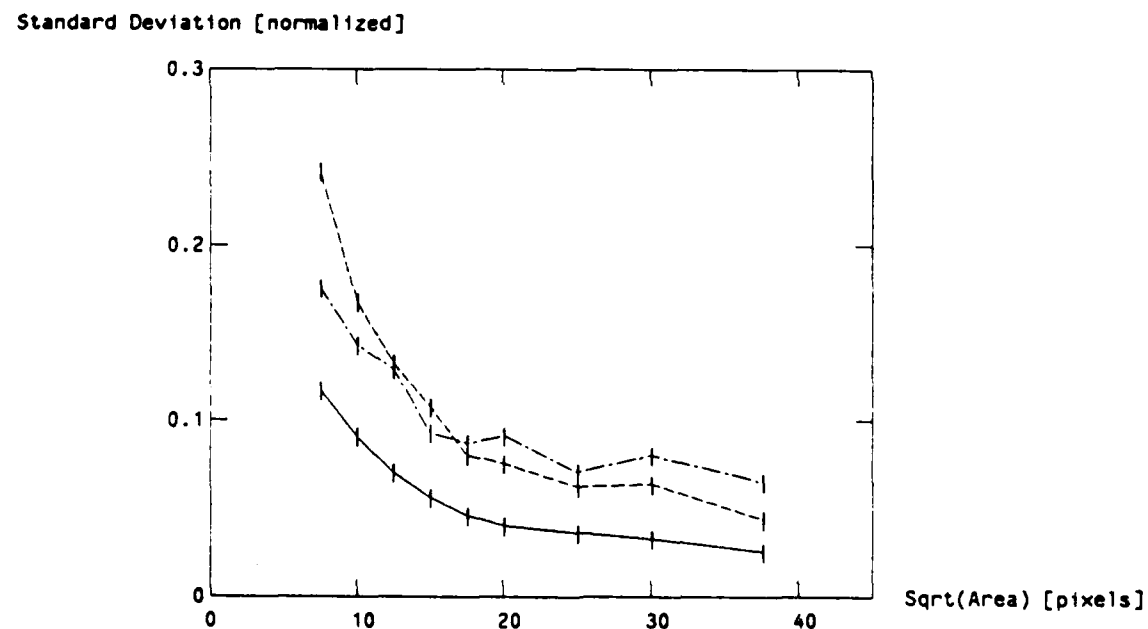


(b) Normalized Standard Deviation of Radius Estimates

Figure 4.4: Radius Estimation for Different Radii



(a) Average of Area Estimates



(b) Normalized Standard Deviation of Area Estimates

Figure 4.5: Area Estimation for Different Radii

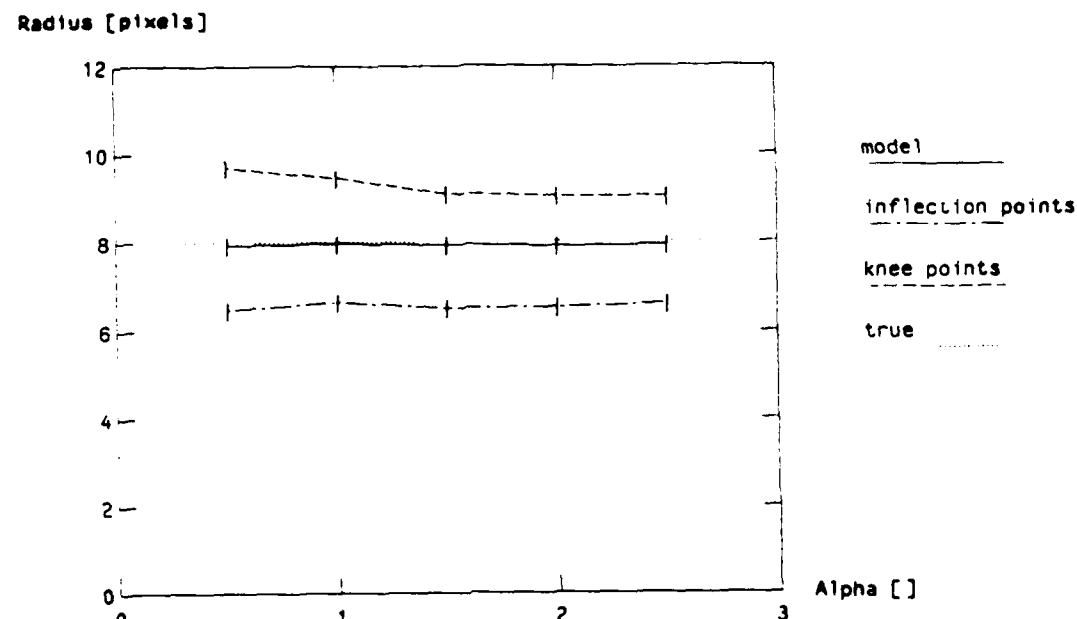
figure 4.5(a) and the x-axis of figure 4.5(b) show the square root of the area, so that the data points are more evenly spaced. The solid line represents the model estimates, the dot-dashed line represents the inflection point estimates, and the dashed line represents the knee point estimates. The true areas lie on the diagonal (dotted line). Here the knee point estimates of the area lie on a line very close and roughly parallel to the diagonal. Again the line bends up near the origin. These observations are much more pronounced in the inflection point results. We also observe that the standard deviation of the slope approach estimates is higher. The average of the model estimates is on the diagonal.

#### 4.1.3 Effect of Parameter Alpha

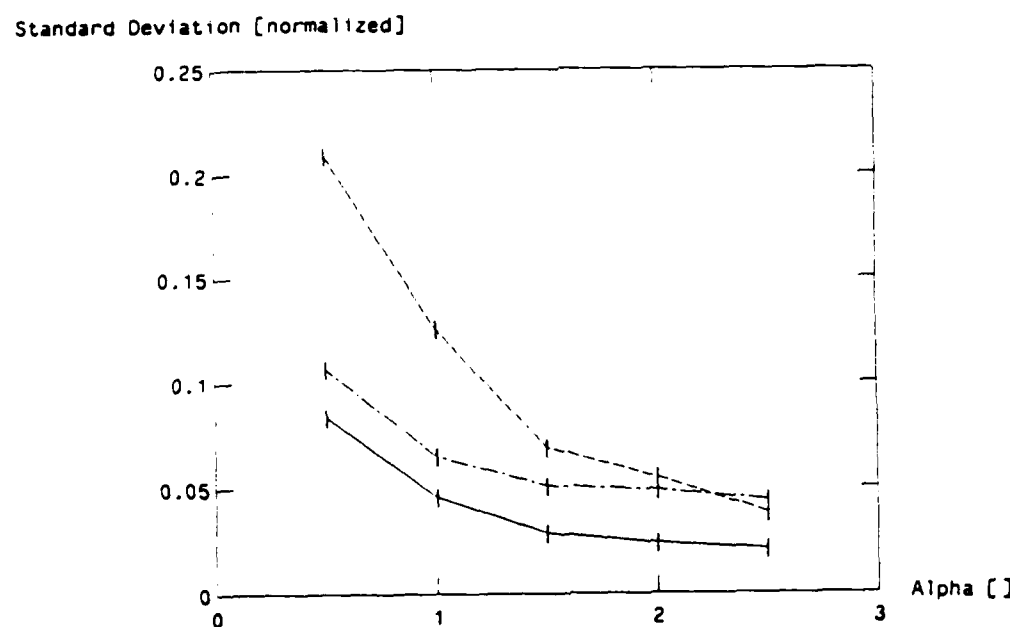
For this experiment all the parameters were fixed except  $\alpha$ . The vessel parameters were  $c = 40$  pixels,  $r = 8$  pixels, and  $s = 1$  pixel. The standard deviation of the noise was fixed at  $\sigma = 2$  (this corresponds to signal to noise ratio of 17.2 dB when  $\alpha = 1$ ). The parameter alpha ranged from  $\alpha = 0.5$  to  $\alpha = 2.5$  in steps of 0.5. For each alpha we considered 80 noise samples and estimated the vessel dimensions for each sample.

The average of the radius estimates as a function of alpha is shown in figure 4.6(a) and the normalized standard deviation is shown in figure 4.6(b). The solid line represents the model estimates, the dot-dashed line represents the inflection point estimates, and the dashed line represents the knee point estimates. The true radius is shown in dotted line. Again we observe that the inflection point method underestimates the vessel radius, and the knee point method overestimates it. Note that the knee point estimates increase for small alphas. The standard deviation of the slope approach estimates is higher than that of the model estimates.

The average of the area estimates as a function of alpha is shown in figure 4.7(a) and the normalized standard deviation is shown in figure 4.7(b). The solid line represents the model estimates, the dot-dashed line represents the inflection point

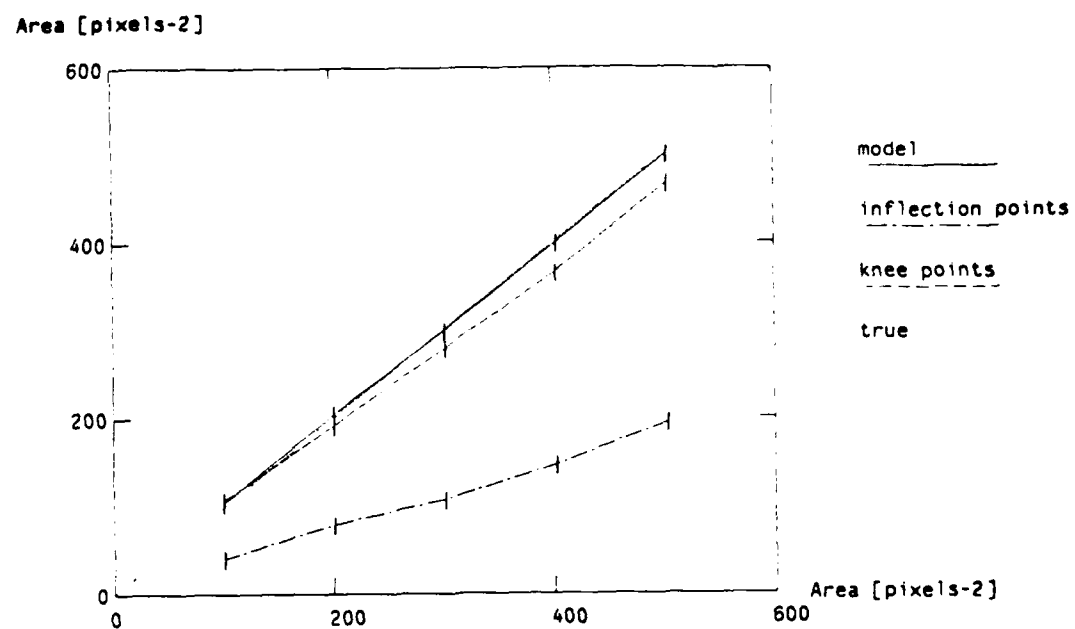


(a) Average of Radius Estimates

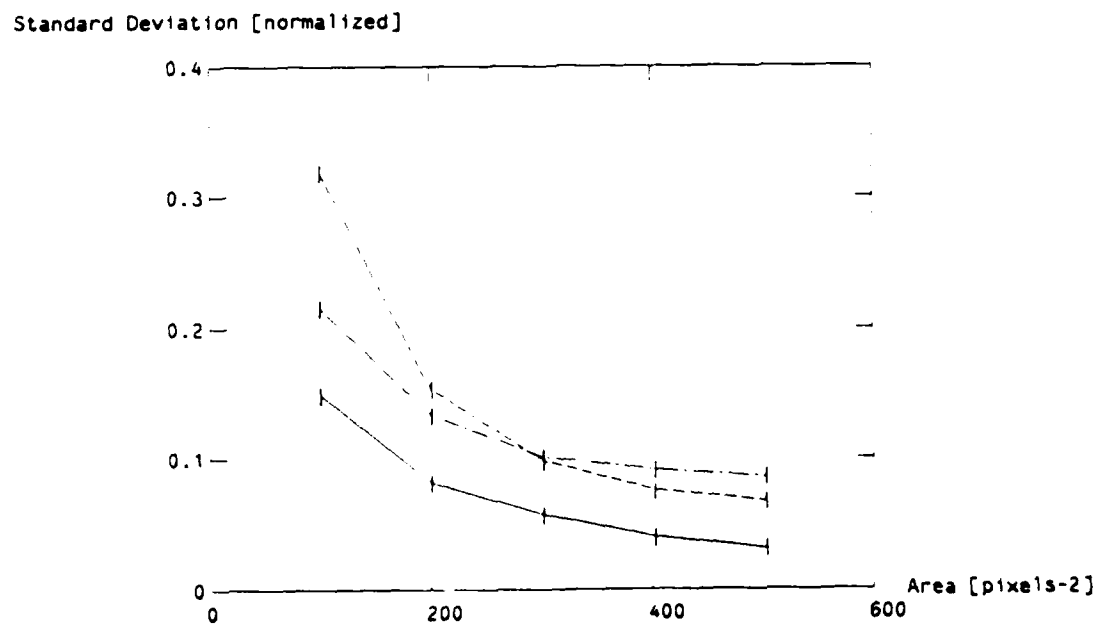


(b) Normalized Standard Deviation of Radius Estimates

Figure 4.6: Radius Estimation for Different Alphas



(a) Average of Area Estimates



(b) Normalized Standard Deviation of Area Estimates

Figure 4.7: Area Estimation for Different Alphas

estimates, and the dashed line represents the knee point estimates. The true areas lie on the diagonal (dotted line). Here we observe a significant bias for the knee point method. The estimates lie on a line that curves up as we approach the origin. Also the standard deviation of the slope approach estimates is higher than that of the model estimates.

#### 4.1.4 Effect of Background

For this experiment all the parameters were fixed except the background. The vessel parameters were  $c = 40$  pixels,  $r = 10$  pixels,  $\alpha = 1$ , and  $s = 1$  pixel. The standard deviation of the noise was fixed at  $\sigma = 2$  (this corresponds to signal to noise ratio of 10.9 dB for the flat background). The different backgrounds used are shown in figure 4.8. They were obtained from actual angiogram profiles. For each background we considered 80 noise samples and estimated the vessel dimensions for each sample. The average of the radius estimates for the different backgrounds is shown in figure 4.9(a) and the normalized standard deviation is shown in figure 4.9(b). The solid line represents the model estimates, the dot-dashed line represents the corresponding results when the inflection points are found, and the dashed line represents the results for the knee points. The true radius lies on the dotted line. The corresponding results for the area estimates are shown in figures 4.10(a) and 4.10(b). We observe that the model estimates are not very sensitive to variations in the background. The same is true for the radius estimates of the slope approaches, but not for the area estimates. This is expected, because the background is smooth and thus cannot have a significant effect on the derivatives of the profile, but it has an effect on the area estimates which assume that the background is linear. Consistent with the previous experiments, the standard deviation of the slope approach estimates is higher than that of the model estimates.

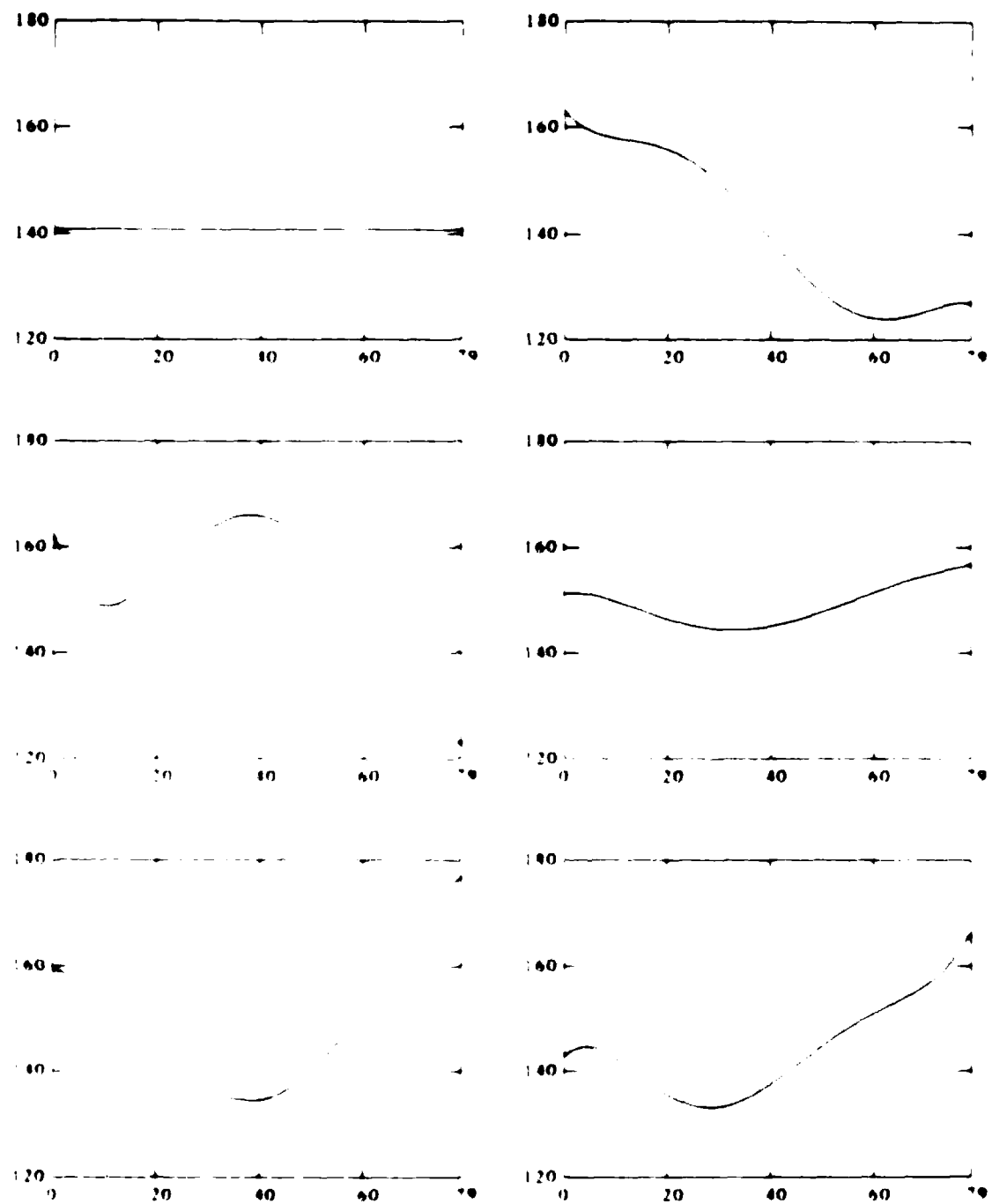
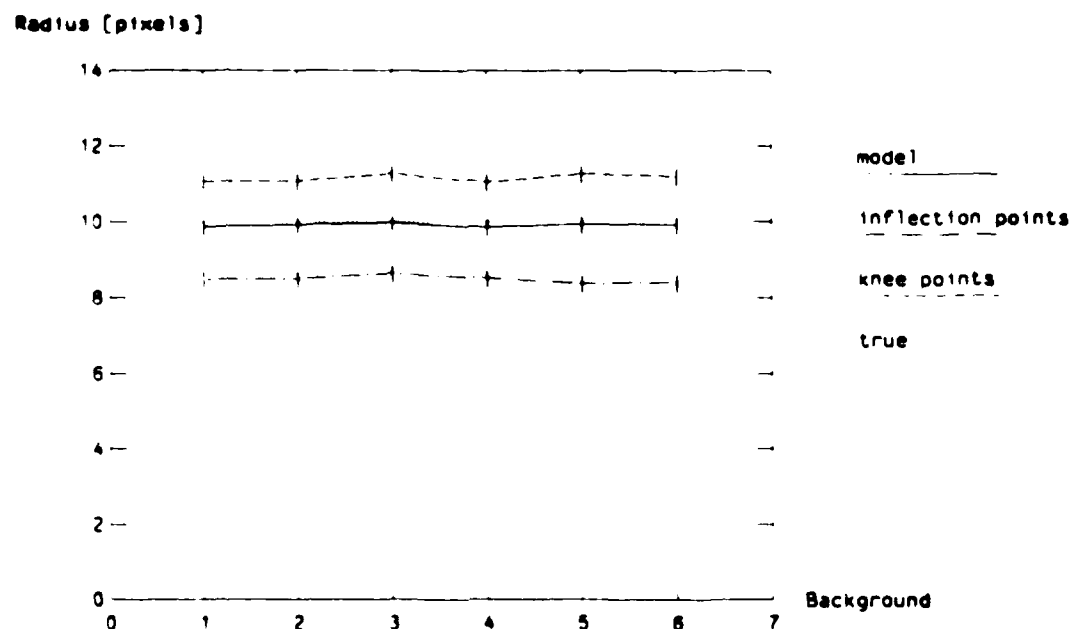
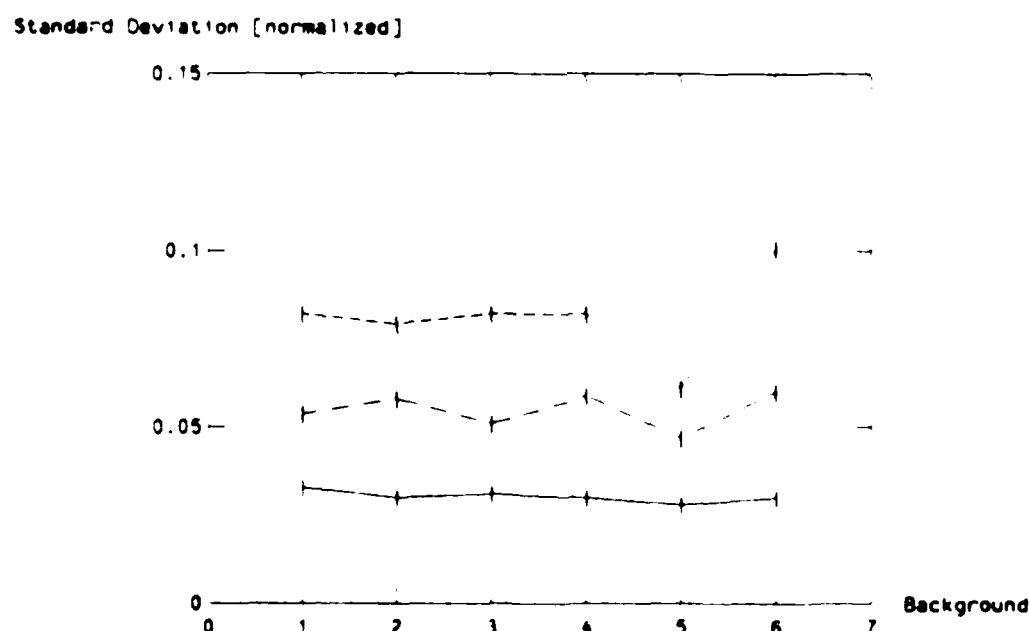


Figure 4 • Different Backgrounds for Background Experiment

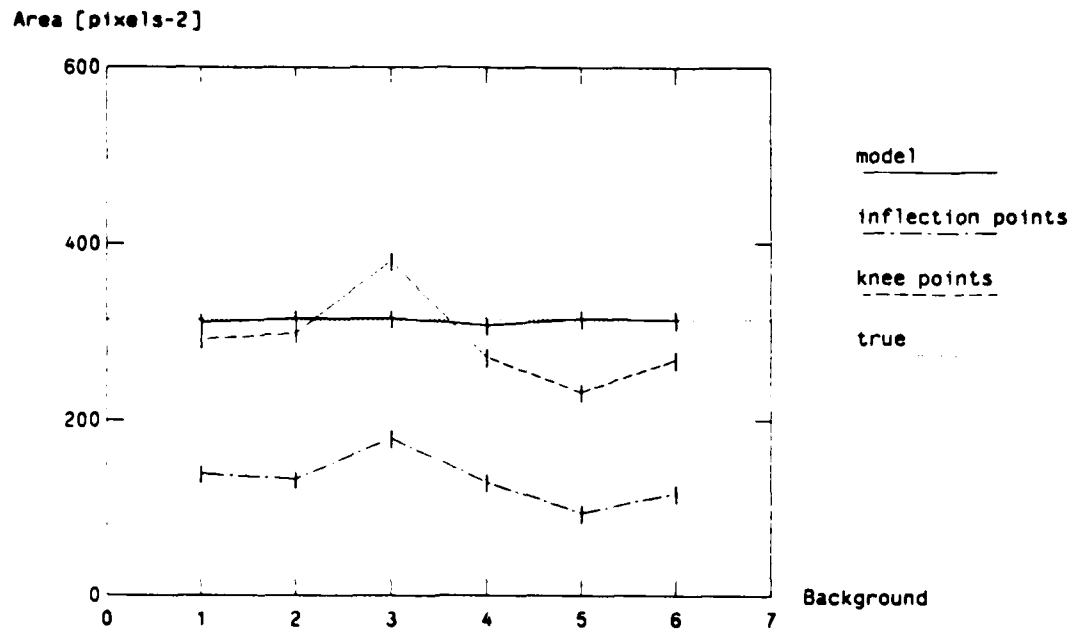


(a) Average of Radius Estimates

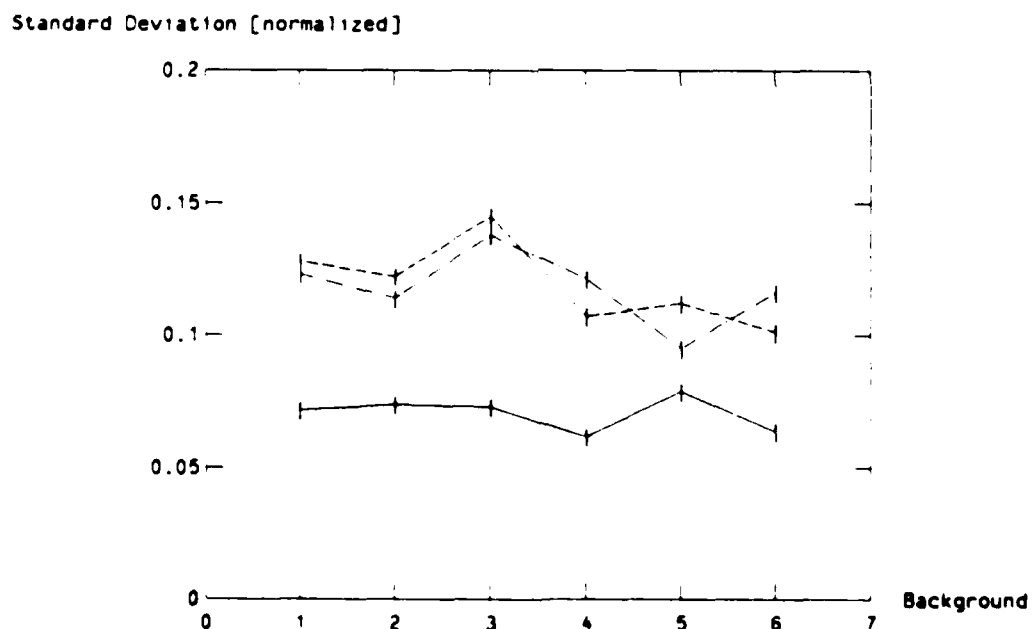


(b) Normalized Standard Deviation of Radius Estimates

Figure 4.9: Radius Estimation for Different Backgrounds



(a) Average of Area Estimates



(b) Normalized Standard Deviation of Area Estimates

Figure 4.10: Area Estimation for Different Backgrounds

#### 4.1.5 Remarks

Summarizing the results of the synthetic data experiments, we note that in all cases the performance of the modeling approach is superior to that of the slope methods. It presents an improvement in both the average of the estimates and in their standard deviation. The bias in the slope methods can lead to significant errors in the determination of the relative dimensions at different points of the vessel.

Our results also indicate that the knee point estimates are less reliable than the inflection point estimates. This should be expected, because the knee point estimates use the second derivatives of the profiles, whereas the inflection point estimates use the first derivatives, which are less sensitive to noise.

## 4.2 Vessel Phantoms

Now we examine the performance of the algorithms on the vessel phantom x-rays. The vessel phantoms are cylindrical holes with 14 different radii, drilled in a plastic block, and filled with angiographic contrast material. The radiographic properties of the plastic block are very similar to those of water, and thus the human tissue. The block is parallelepiped, so the background of the phantom x-rays is flat. All x-rays were obtained under the same set of radiographic conditions. The vessel phantoms are shown in figure 4.11. Figure 4.12 shows the perpendicular cross-section of a vessel phantom and the profile of the perfect projection at that cross-section. Since the phantoms have constant cross-sections, this experiment is similar to the radius experiment performed in the synthetic data case. We considered 50 consecutive profiles of each phantom, and estimated the vessel dimensions for each profile. The estimates were averaged and the standard deviation of the estimates was computed. The degree of the polynomials used in the modeling approach was 3. As we discussed in section 3.1, a lower degree (3 instead of 5) polynomial to model an approximately flat background performs better in this case.

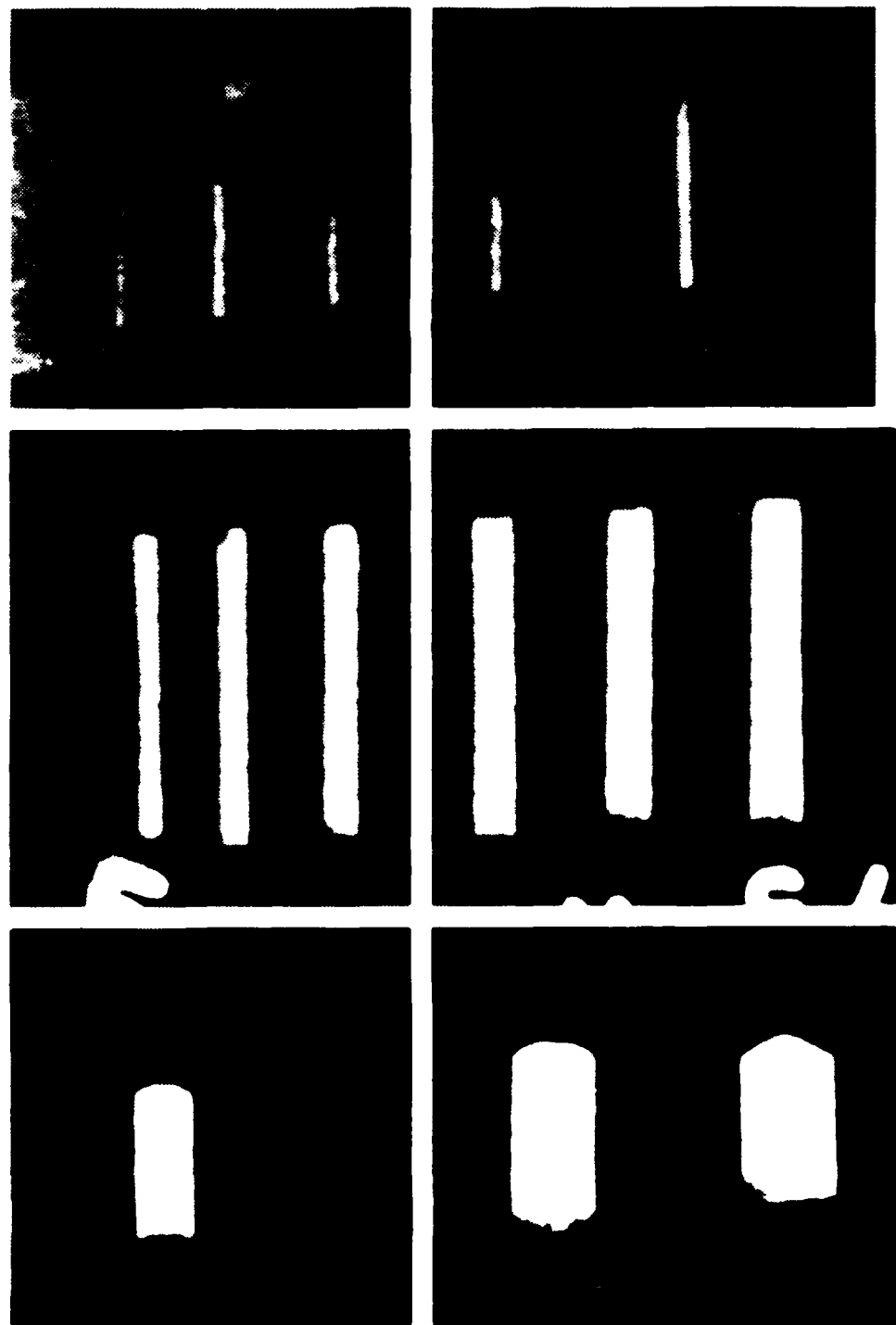


Figure 4.11 Vessel Phantoms

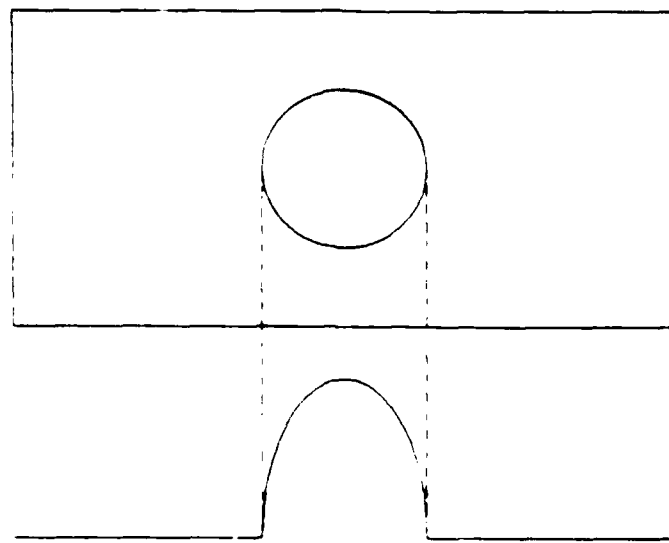
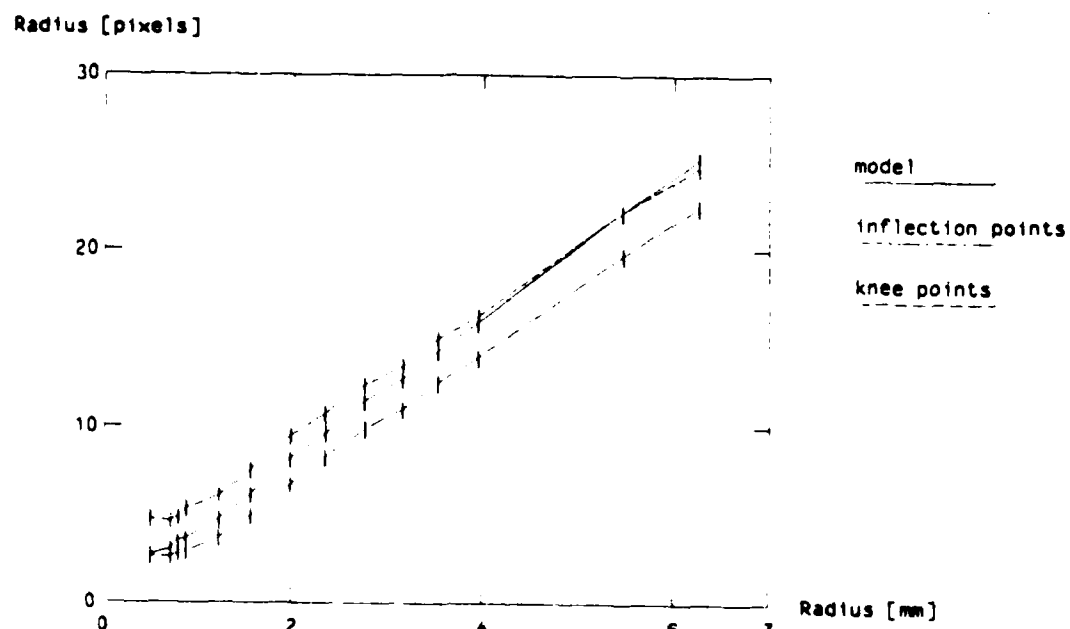


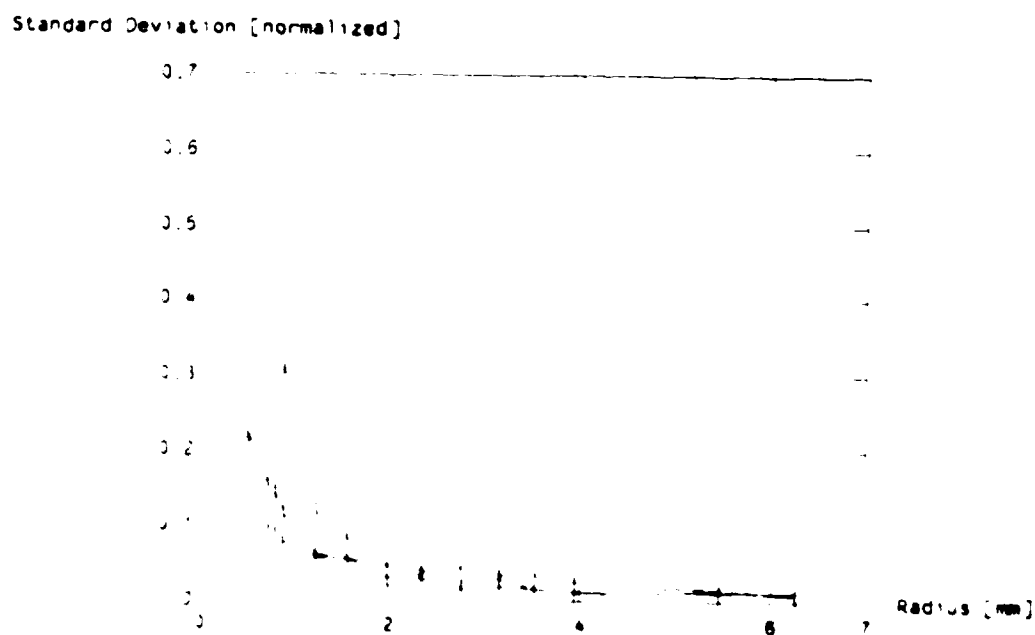
Figure 4.12: Vessel Phantom Cross-Section and Perfect Projection

The average of the radius estimates as a function of true radius is shown in figure 4.13(a) and the normalized standard deviation is shown in figure 4.13(b). The solid line represents the model estimates, the dot-dashed line represents the inflection point estimates, and the dashed line represents the knee point estimates. The units of the x-axis are millimeters (mm) and of the y-axis pixels. The exact correspondence is not known, and is important only if absolute measurements are desired. If we are interested in relative measurements, then the estimates are satisfactory when they lie on a straight line passing through the origin. Since the exact correspondence between the radius in mm and the radius in pixels is not known, we normalized the standard deviation of the estimates by the values on a diagonal line close to the average of the estimates.

Observe that the average of the model estimates roughly lies on a straight line through the origin. This is not true for the inflection and knee point estimates. The corresponding lines do not pass through the origin, and curve up near the origin. Observe also that the inflection point method underestimates the vessel radius relative to the modeling approach, and the knee point method overestimates



(a) Average of Radius Estimates



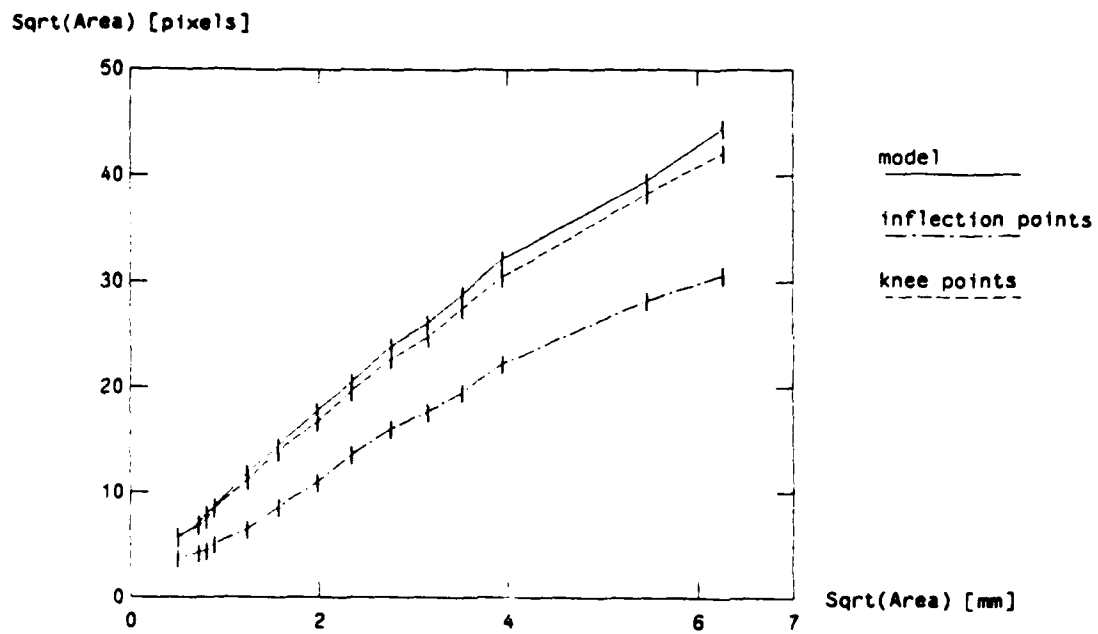
(b) Normalized Standard Deviation of Radius Estimates

Figure 4.13 Phantom Experiment: Radius Estimation

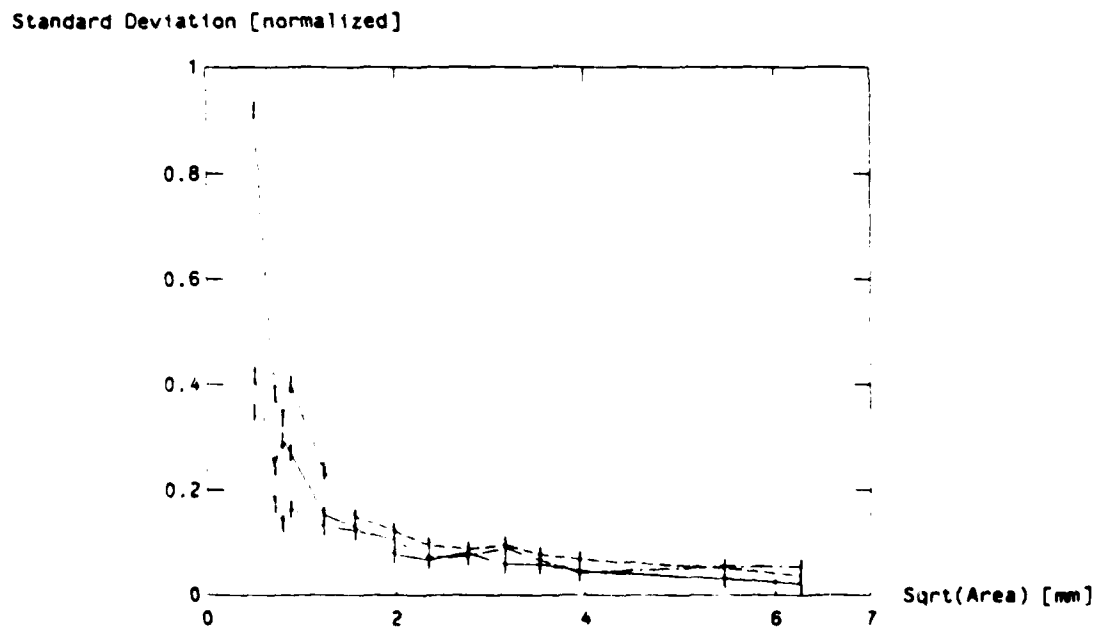
it. These results are similar to those obtained in the radius experiment of the synthetic data case. The standard deviation of the model estimates is only slightly lower than that of the slope estimates. This is due to the fact that in this set of experiments the signal to noise ratio is very high for phantoms with radii greater than 1mm. Also, the fact that the background is flat eliminates one potential source of error for the slope methods, which estimate the background as the straight line connecting the boundary points.

The average of the area estimates as a function of area is shown in figure 4.14(a) and the standard deviation is shown in figure 4.14(b). Similarly to the radius case, the standard deviation of the estimates was normalized by the values on a diagonal line close to the average of the estimates. Both axes of figure 4.14(a) and the x-axis of figure 4.14(b) show the square root of the area, so that the data points are more evenly spaced. The solid line represents the model estimates, the dot-dashed line represents the inflection point estimates, and the dashed line represents the knee point estimates.

We observe that the knee point method slightly underestimates the area relative to the model estimates. As we noted in the synthetic data experiments, the inflection point method grossly underestimates the area, and is of limited usefulness. Also, the standard deviation of the model estimates is lower than that of the knee point estimates. However, there is a major difference from the synthetic data results. The average of the estimates does not lie on a straight line. Instead, it lies on a line that bends down as the radius increases. This is true for both the modeling approach and the slope approach. The reason for this is that the relationship between the density of the radiographic image and the thickness of the contrast agent is not linear. As we discussed in the introduction, appropriate corrections can be made to restore linearity [30,31,17]. This result indicates that the cross-sectional area estimation is more sensitive to the imaging process, and emphasizes the importance of densitometric checks and, if necessary, calibration of the imaging system.



(a) Average of Area Estimates



(b) Normalized Standard Deviation of Area Estimates

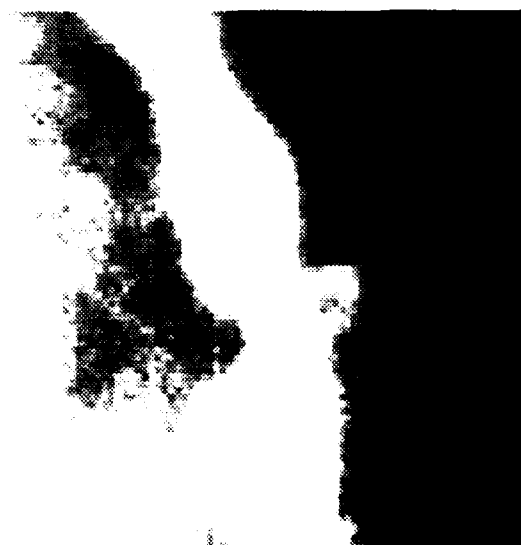
Figure 4.14: Phantom Experiment: Area Estimation

## 4.3 Coronary Angiograms

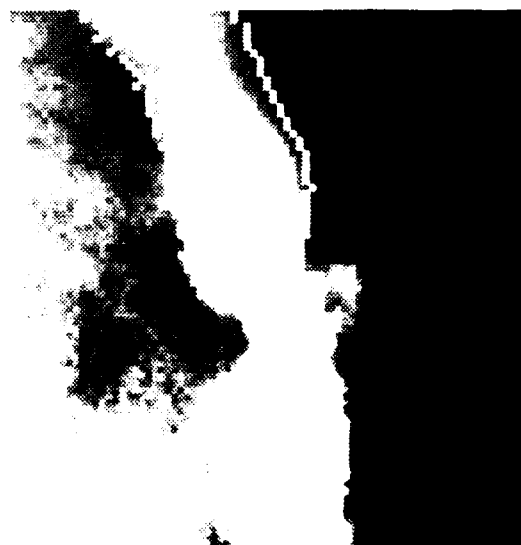
The performance of the algorithms was also tested on real coronary angiograms. As we mentioned earlier, it is very difficult to evaluate the performance of the algorithms in this case, because we do not know the true dimensions of the arteries. However, a simple inspection of the angiograms and their models can give us a good indication of the relative performance of the two approaches. Thus the comparisons in this section will be qualitative, in contrast to the quantitative results of the previous sections.

In the examples we present, the approximate direction of the blood vessels is vertical. The one-dimensional algorithm was applied to the profiles perpendicular to this direction. The degree of the polynomials used in the modeling approach was 5. As we discussed in section 3.1, a second iteration of the algorithms could provide the parameters of the perpendicular vessel cross-sections. Since both approaches use the same profiles, we chose not to carry out the second step. This does not affect the comparison of the two methods, and makes the presentation of the results a lot easier.

A section of a coronary angiogram is shown in figure 4.15(a); the resolution is  $80 \times 80$  pixels. The boundaries detected by the modeling approach are shown in figure 4.15(b). Figures 4.15(c) and (d) show the inflection and knee points, respectively. The boundaries detected by the modeling approach and the inflection points appear to follow the shape of the vessel very well. The knee point boundaries are more noisy, as should be expected from our analysis and previous results. Also consistent with our previous results is the fact that the inflection point boundaries are inside the model boundaries, and the knee point boundaries are outside. As we mentioned in section 1.2, the inflection points are close to what our eyes perceive as the vessel edge, which is not the same as the actual vessel edges. The area estimates are shown in figure 4.16. The solid line represents the modeling approach estimates, the dot-dashed line represents the inflection point estimates, and the dashed line



(a) Original



(b) Modeling Approach



(c) Edge Points



(d) K-means

Figure 4.15: Boundary Detection Results.

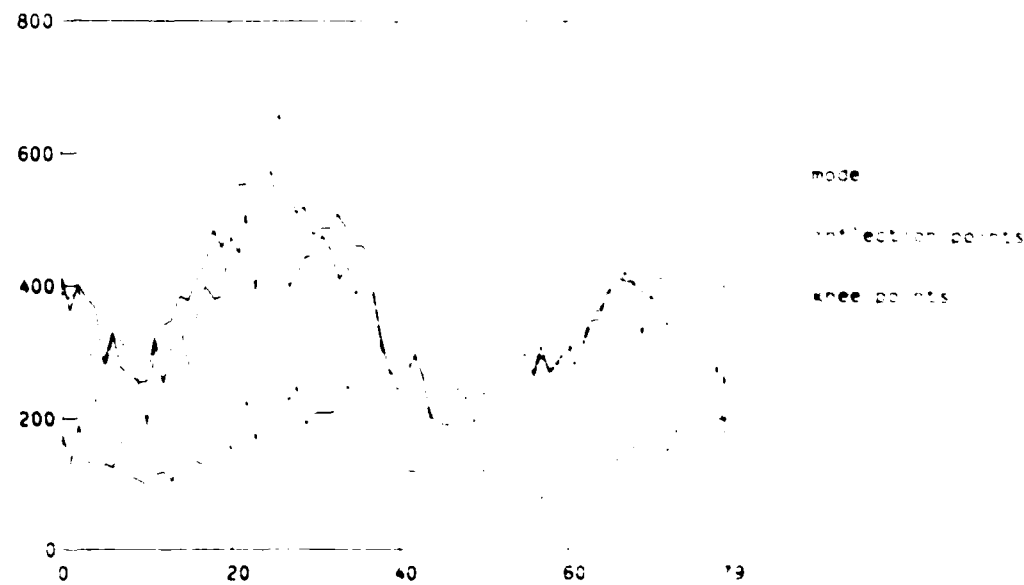


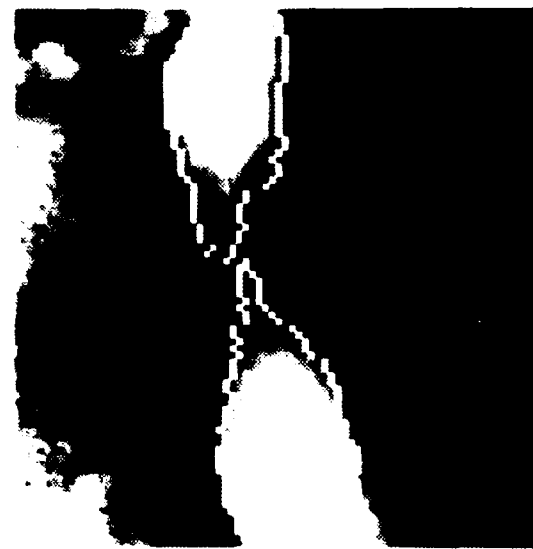
Figure 4.16. Cross-sectional Area Detection - Example A

represents the knee point estimates.

Another example is shown in figure 4.17(a); the resolution is  $80 \times 80$  pixels. The boundaries detected by the modeling approach are shown in figure 4.17(b). Figures 4.17(c) and (d) show the inflection and knee points, respectively. There is a severe obstruction in this vessel segment. The performance of the algorithms in the wide regions of the vessel is similar to the previous example. At the narrow section of the vessel the inflection point boundaries are very noisy, and the knee point boundaries fail completely. Also note that at the narrowing the inflection point boundaries are wider than the mode boundaries. This is consistent with our synthetic data results, where we showed that the slope approach tends to overestimate the vessel diameter at the narrow points. The area estimates are shown in figure 4.18. The solid line represents the modeling approach estimates, the dashed line represents the inflection point estimates, and the long-dash line represents the knee point estimates.



(a) Image



(b) Modeling Approach



(c) Smoothing



(d) Knee Points

Figure 4.17: Boundary Detection (Example B)

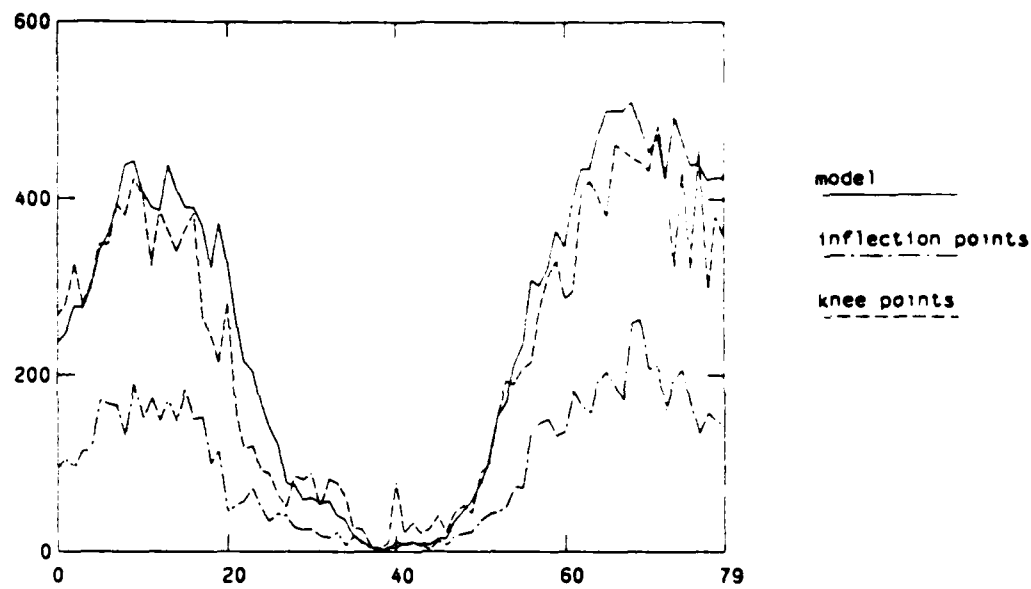


Figure 4.18: Cross-sectional Area Detection (Example B)

#### 4.4 Summary

The experimental results we presented in this chapter indicate that the performance of the modeling approach is better than that of the slope methods. Our results show that the inflection points tend to be inside the model based boundaries and the knee points tend to be outside. More importantly, this bias is not consistent, thus resulting in errors in the determination of the relative dimensions at different points of the vessel. The variance of the slope method estimates was shown to be higher than that of the model based estimates. In the case of the knee point estimates, the variance was especially high for low signal to noise ratios, that is, for the obstructed sections of the vessel.

The reason for the better performance of the modeling approach is that it uses all the information available in the vessel profile. The slope approaches use information ~~more~~ locally (the slope at the sides, or the second derivative near the base points of the profile). Thus they can be very sensitive to the local shape of the profile.

rather than its overall structure. For example, if there are two local maxima of the slope, it is not clear which one should be the boundary point. Similarly, the cross-sectional area estimates depend only on the boundary points to estimate the background. The model works well even when the number of samples across the vessel profile is very small. This is an advantage over the slope methods in which it becomes difficult to determine the inflection or knee points accurately as the number of samples decreases.

The advantage of the slope methods is their computational simplicity. However, when one considers the time and effort that is required to get an angiogram of the coronary arteries, it appears to be reasonable to spend more time to get better estimates of the severity of the obstructions.

## Chapter 5

# Comparison of Two-Dimensional Model With One-Dimensional Model

In this chapter we examine the performance of the two-dimensional model and compare it to that of the one-dimensional model. The two-dimensional model incorporates the spatial continuity of the vessel and the background, and is thus expected to be more robust to noise than the one-dimensional model.

In the experiments of the previous chapter we considered each densitometric profile independently of the adjacent profiles, i.e., the spatial continuity of the vessel and the background was not taken into account. In chapter 3 we discussed a heuristic way to use the spatial continuity of the vessel with the one-dimensional approach. This is to fit splines to the estimated vessel parameter sequences. We will refer to this modified approach as the smoothed one-dimensional approach. In order to compare it to the two-dimensional approach, we will use the same spline parameters for the smoothed one-dimensional approach as those of the two-dimensional approach. In the following experiments we will compare the two-dimensional approach with both the one-dimensional approach and the smoothed one-dimensional

approach.

Similarly to the previous chapter, the algorithms were tested on computer generated data (synthetic data), on x-rays of contrast-medium-filled cylindrical phantoms, and on real coronary angiograms.

## 5.1 Synthetic Data

First we examine the performance of the model on synthetic data. The data were generated assuming the two-dimensional model is valid. We conducted a number of experiments to study the properties of the two-dimensional modeling approach and compare it with the one-dimensional approach. In particular, we investigated the behavior of the two approaches for different levels of noise and different vessel dimensions.

In order to be able to make quantitative statements about the experiments, we considered first vessels of constant radius ( $r(q) = r_0$ ) and alpha ( $\alpha(q) = \alpha_0$ ). Also, we chose the axes of the vessels to be straight vertical lines ( $c_1(q) = c_0$ ,  $c_2(q) = q$ ). This makes it possible to isolate the effects that the level of the noise, the radius of the vessel, and the parameter alpha have on the problem. It also simplifies the implementation of the one-dimensional algorithm, and makes the comparison easier. Since the two-dimensional algorithm does not take these facts into consideration, they should not bias our experiments. A more realistic example with parameter sequences obtained from a real angiogram will be considered at the end of this section.

In each of the experiments we describe below, all the parameters (background,  $c_0$ ,  $r_0$ ,  $\alpha_0$ ,  $\sigma$ , and noise variance) were fixed except one. We considered one noise sample for each value of the variable parameter, and estimated the vessel parameter sequences using the one-dimensional and two-dimensional approaches. Each sample is now a two-dimensional image (50 x 50 pixels). Since the sequences  $r(q)$  and  $\alpha(q)$

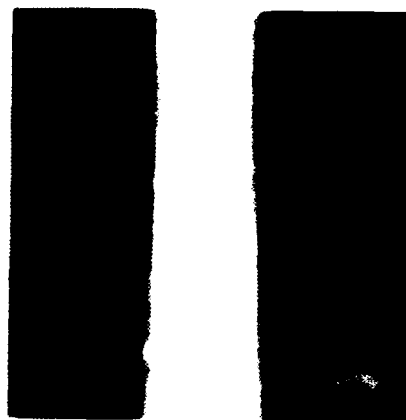


Figure 5.1: Two-Dimensional Synthetic Image

and hence the vessel cross-sections are constant, we can compute the average and standard deviation of the radius and area sequence estimates over  $q$ . This is similar to the experiments of chapter 4, where we considered 80 noise samples of a one-dimensional profile and averaged the estimates. The standard deviation was normalized, that is, it was divided by the true value of the parameter being estimated (radius or area).

A typical example of a synthetic test image is shown in figure 5.1. The background is a fifth degree two-dimensional polynomial, obtained from a real angiogram. The vessel parameter values are  $c_1(q) = 25$  pixels,  $r(q) = 8$  pixels,  $\alpha(q) = 2$ , for all  $q$ , and  $S = \text{diag}(1,1)$  (pixels)<sup>2</sup>. The standard deviation of the noise is  $\sigma = 2$ , which corresponds to signal to noise ratio of 16.2 dB.

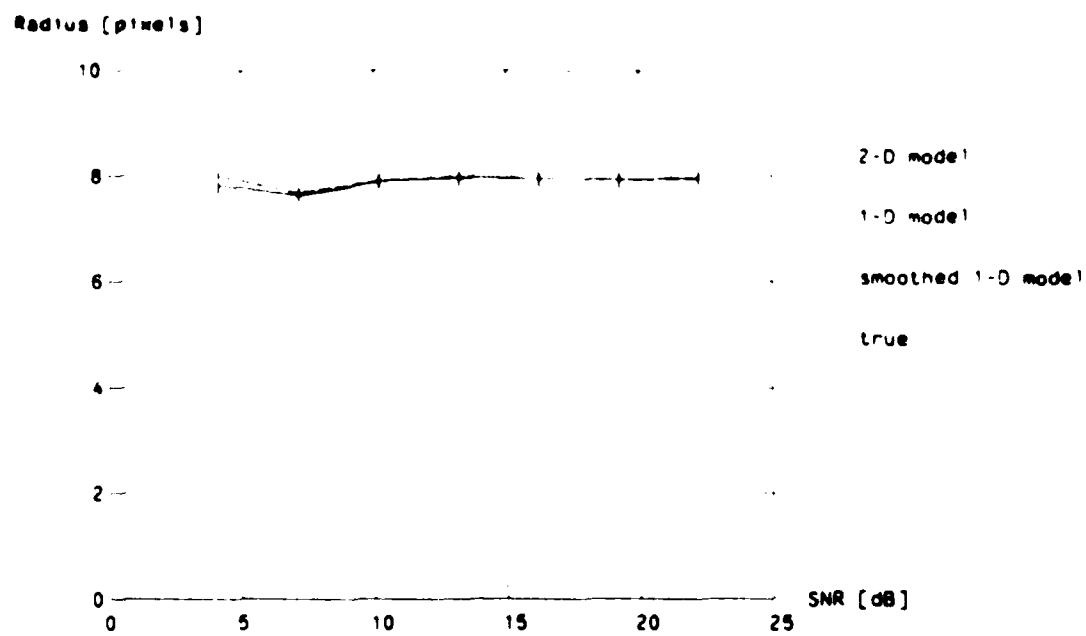
The degree of both the two-dimensional and the one-dimensional polynomials used in the corresponding estimation algorithms was 5, the same as that of the synthetic data. The spacing of the nodes of the cubic splines used in the last stage of the two-dimensional algorithm and for smoothing the one-dimensional estimates was 7 points.

### 5.1.1 Effect of Noise Level

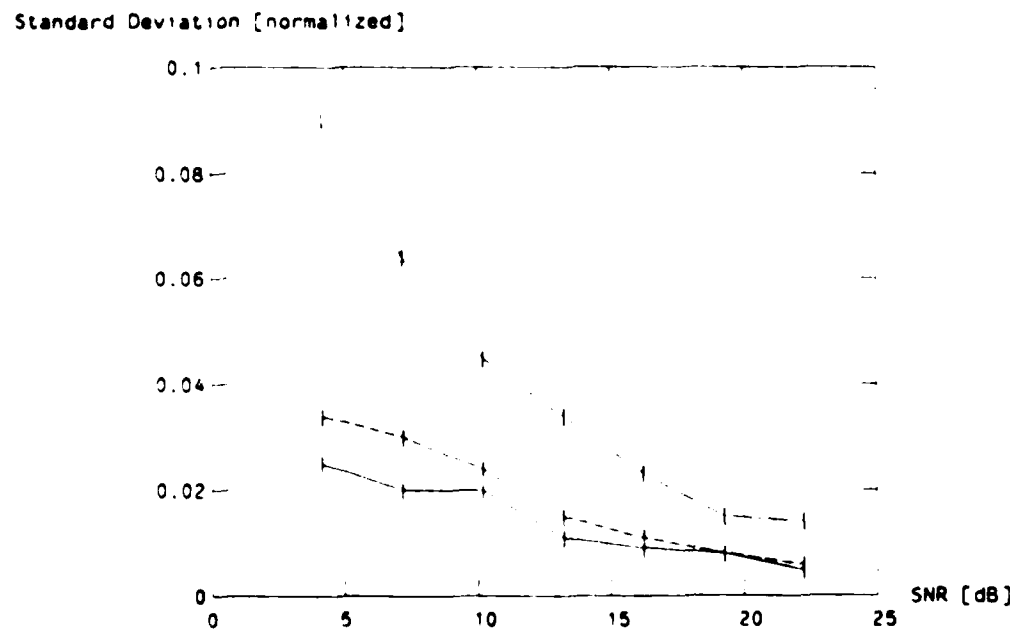
For this experiment all the parameters were fixed except the noise level. The synthetic image we used was that of figure 5.1. The vessel parameters were  $c_1 q = 25$  pixels,  $r q = 8$  pixels, and  $\alpha q = 2$ , for all  $q$ , and  $S = \text{diag}(1, 1)$  (pixels)<sup>2</sup>. To this profile we added 7 different levels of noise. For each noise sample we estimated the vessel parameter sequences using the two-dimensional and one-dimensional approaches. The signal to noise ratio (SNR) is defined as in equation (4.1) of the previous chapter.

The average of the radius estimates as a function of signal to noise ratio is shown in figure 5.2(a) and the normalized standard deviation is shown in figure 5.2(b). The solid line represents the two-dimensional model estimates, the dot-dashed line represents the one-dimensional model estimates without any smoothing, and the dashed line represents the smoothed one-dimensional estimates. The true radius is shown in dotted line. We observe that the average of the estimates for the two-dimensional approach is very similar to that of the one-dimensional approach. The smoothing of the one-dimensional estimates does not affect the average (the dot-dashed and dashed lines coincide), but, as expected, improves considerably the standard deviation. The standard deviation of the two-dimensional estimates is only slightly better than that of the smoothed one-dimensional estimates.

The average of the area estimates as a function of signal to noise ratio is shown in figure 5.3(a) and the normalized standard deviation is shown in figure 5.3(b). The solid line represents the two-dimensional model estimates, the dot-dashed line shows the one-dimensional model estimates without any smoothing, and the dashed line shows the smoothed one-dimensional estimates. The dotted line represents the true area. In figure 5.3(a) the dot-dashed and dashed lines coincide. The two-dimensional approach offers some improvement in the average of the estimates, and only a small improvement in the standard deviation of the smoothed one-dimensional estimates.

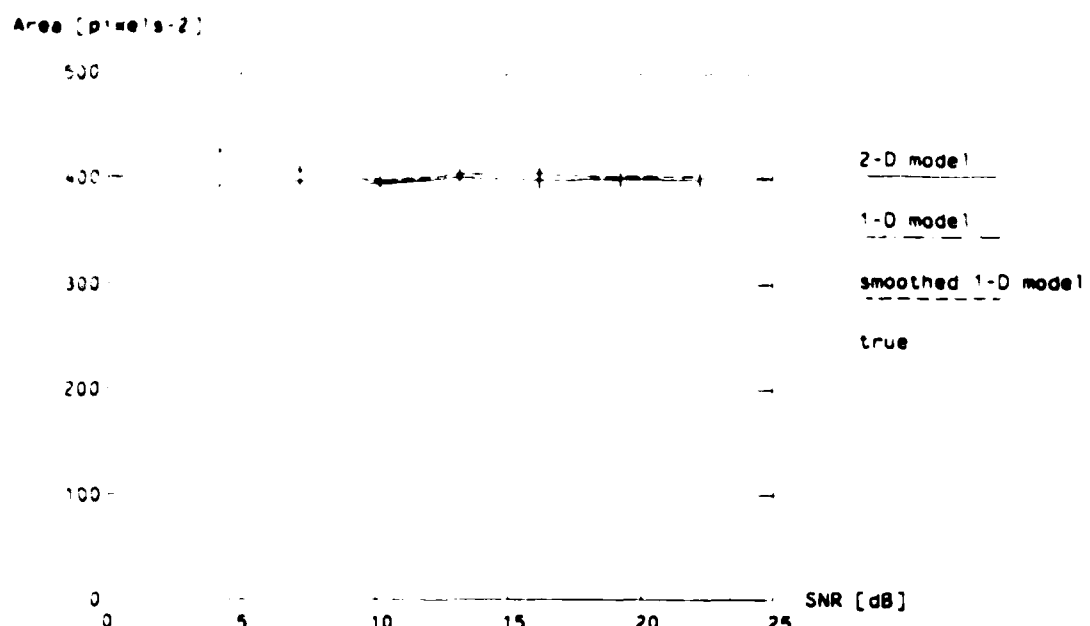


(a) Average of Radius Estimates

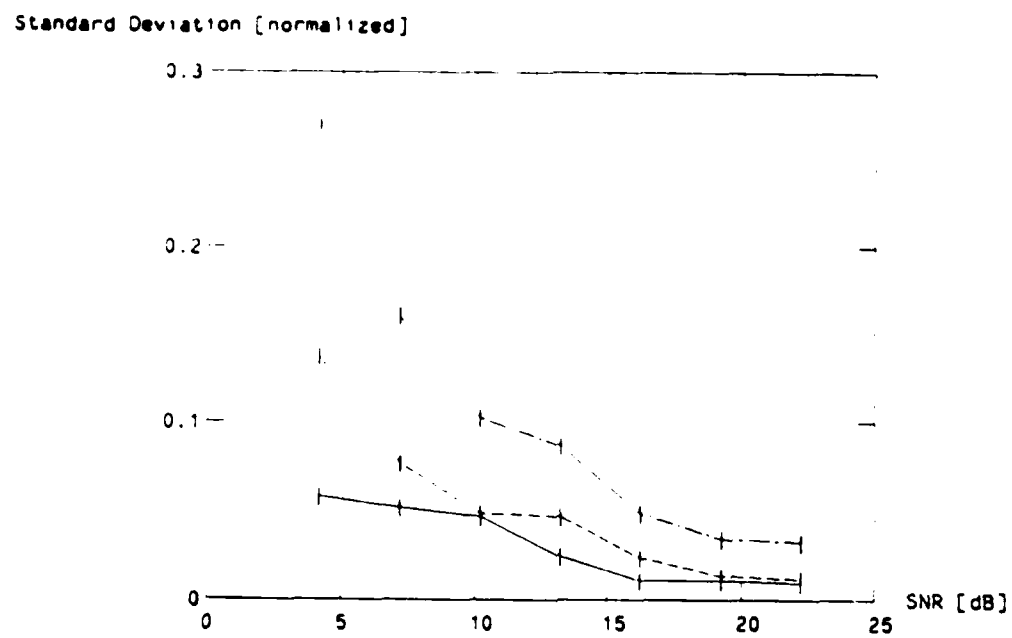


(b) Normalized Standard Deviation of Radius Estimates

Figure 5.2: Radius Estimation for Different SNR's



(a) Average of Area Estimates



(b) Normalized Standard Deviation of Area Estimates

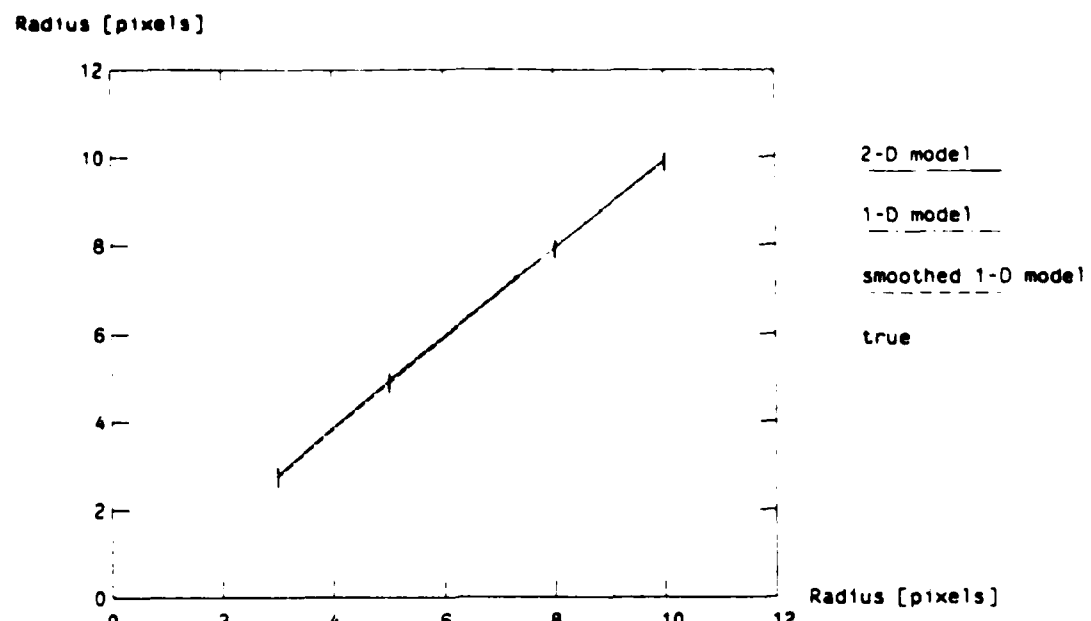
Figure 5.3: Area Estimation for Different SNR's

### 5.1.2 Effect of Vessel Radius

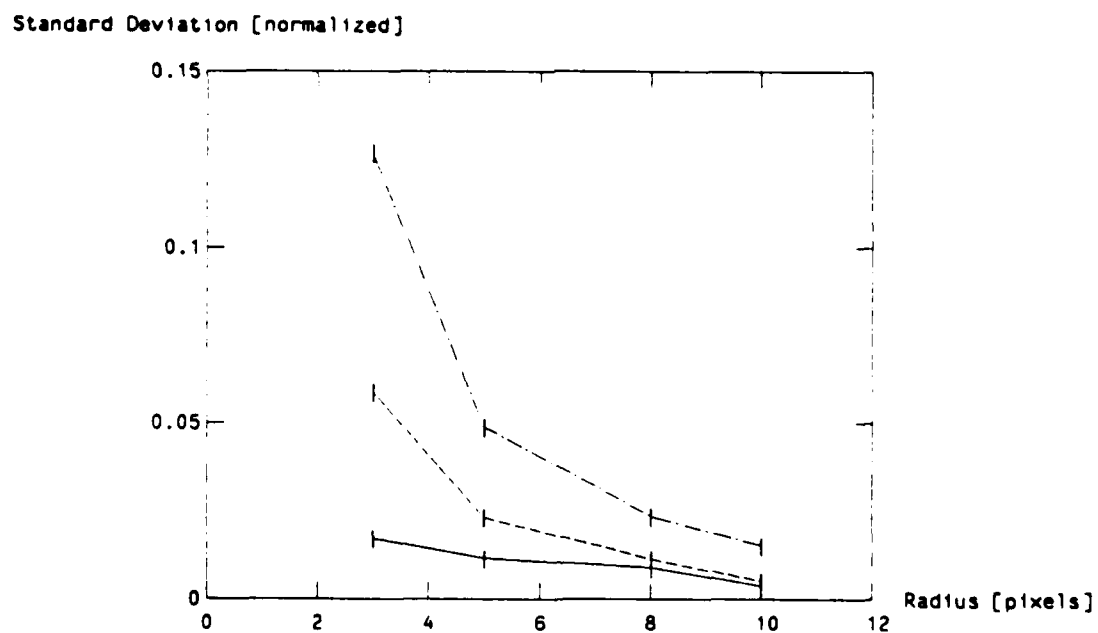
For this experiment all the parameters were fixed except the vessel radius. The vessel parameters were  $c_1[q] = 25$  pixels,  $r[q] = r_o$  pixels, and  $\alpha[q] = 2$ , for all  $q$ , and  $S = \text{diag}(1, 1)$  (pixels)<sup>2</sup>. The standard deviation of the noise was fixed at  $\sigma = 2$  (this corresponds to signal to noise ratio of 16.2 dB when  $r_o = 8$  pixels). The values of the radius were  $r_o = 3, 5, 8, 10$  pixels. We estimated the vessel parameter sequences for each radius using the two-dimensional and one-dimensional approaches.

The average of the radius estimates as a function of radius is shown in figure 5.4(a) and the normalized standard deviation is shown in figure 5.4(b). The solid line represents the two-dimensional model estimates, the dot-dashed line represents the one-dimensional model estimates without any smoothing, and the dashed line represents the smoothed one-dimensional estimates. The true radii lie on the diagonal (dotted line). We observe that the average of the estimates for the two-dimensional approach is almost identical to that of the one-dimensional approach, and both are close to the true value. The two-dimensional approach offers some improvement in the standard deviation of the estimates, especially for smaller radii.

The average of the area estimates as a function of area is shown in figure 5.5(a) and the normalized standard deviation is shown in figure 5.5(b). Both axes of figure 5.5(a) and the x-axis of figure 5.5(b) show the square root of the area, so that the data points are more evenly spaced. The solid line represents the two-dimensional model estimates, the dot-dashed line shows the one-dimensional model estimates without any smoothing, and the dashed line shows the smoothed one-dimensional estimates. The dotted line represents the true area. Again, the average of the estimates for the two-dimensional approach is very close to that of the one-dimensional approach, and both are close to the true area. The two-dimensional approach offers some improvement in the standard deviation of the estimates over the smoothed one-dimensional approach.

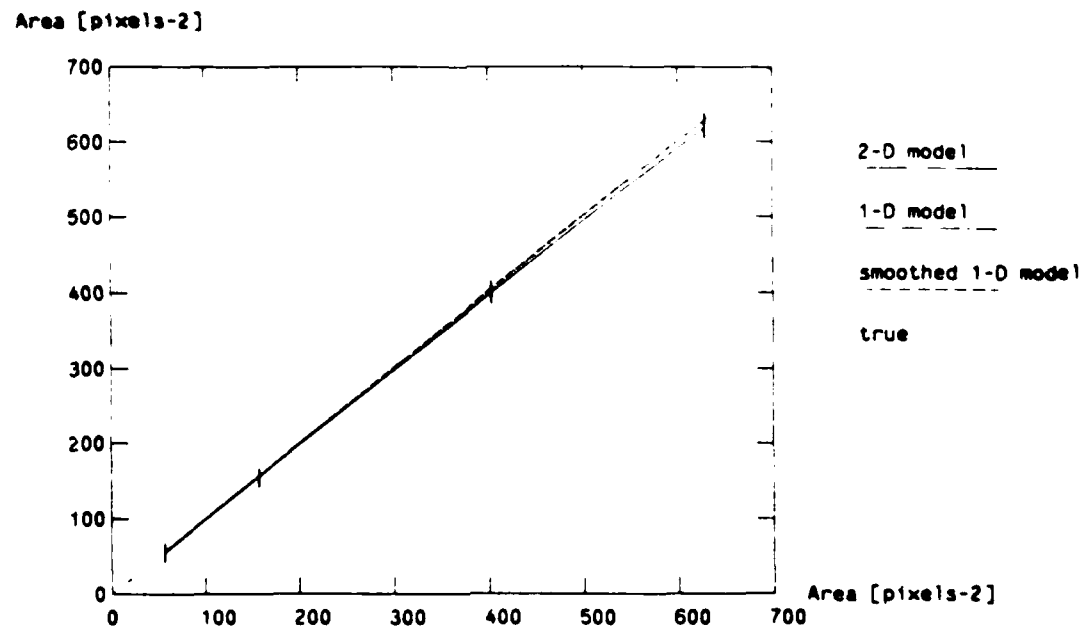


(a) Average of Radius Estimates

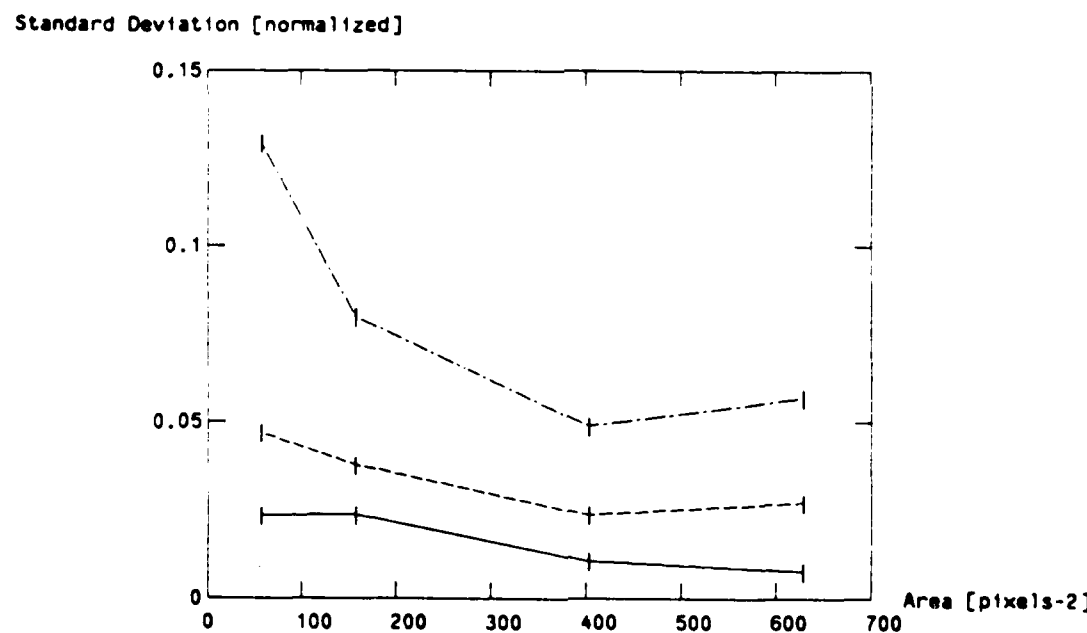


(b) Normalized Standard Deviation of Radius Estimates

Figure 5.4: Radius Estimation for Different Radii



(a) Average of Area Estimates



(b) Normalized Standard Deviation of Area Estimates

Figure 5.5: Area Estimation for Different Radii

### 5.1.3 Effect of Parameter Alpha

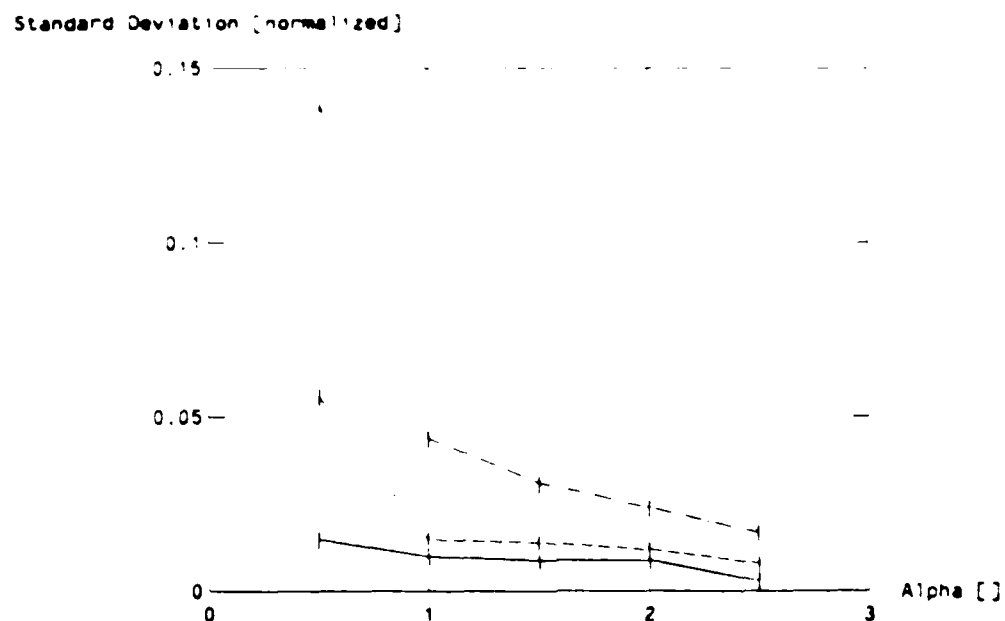
For this experiment all the parameters were fixed except  $\alpha$ . The vessel parameters were  $c_1 q = 25$  pixels,  $r q = 8$  pixels, and  $\alpha q = \alpha_*$ , for all  $q$ , and  $S = (1, 1)$  (pixels<sup>2</sup>). The standard deviation of the noise was fixed at  $\sigma = 2$  (this corresponds to signal to noise ratio of 16.2 dB when  $\alpha = 2$ ). The parameter alpha ranged from  $\alpha_* = 0.5$ , to  $\alpha_* = 2.5$  in steps of 0.5. For each  $\alpha$  we estimated the vessel parameter sequences using the two-dimensional and one-dimensional approaches.

The average of the radius estimates as a function of alpha is shown in figure 5.6(a) and the normalized standard deviation is shown in figure 5.6(b). The solid line represents the two-dimensional model estimates, the dot-dashed line represents the one-dimensional model estimates without any smoothing, and the dashed line represents the smoothed one-dimensional estimates. The true radius is shown in dotted line. We observe that the average of the estimates for the two-dimensional approach is almost identical to that of the one-dimensional approach, and both are close to the true value. The two-dimensional approach offers some improvement in the standard deviation of the estimates only when alpha is small.

The average of the area estimates as a function of alpha is shown in figure 5.7(a) and the normalized standard deviation is shown in figure 5.7(b). The solid line represents the two-dimensional model estimates, the dot-dashed line shows the one-dimensional model estimates without any smoothing, and the dashed line shows the smoothed one-dimensional estimates. The dotted line represents the true area. Again, the average of the estimates for the two-dimensional approach is very close to that of the one-dimensional approach, and both are close to the true area. The two-dimensional approach offers some improvement in the standard deviation of the estimates over the smoothed one-dimensional estimates, more so for small alpha.

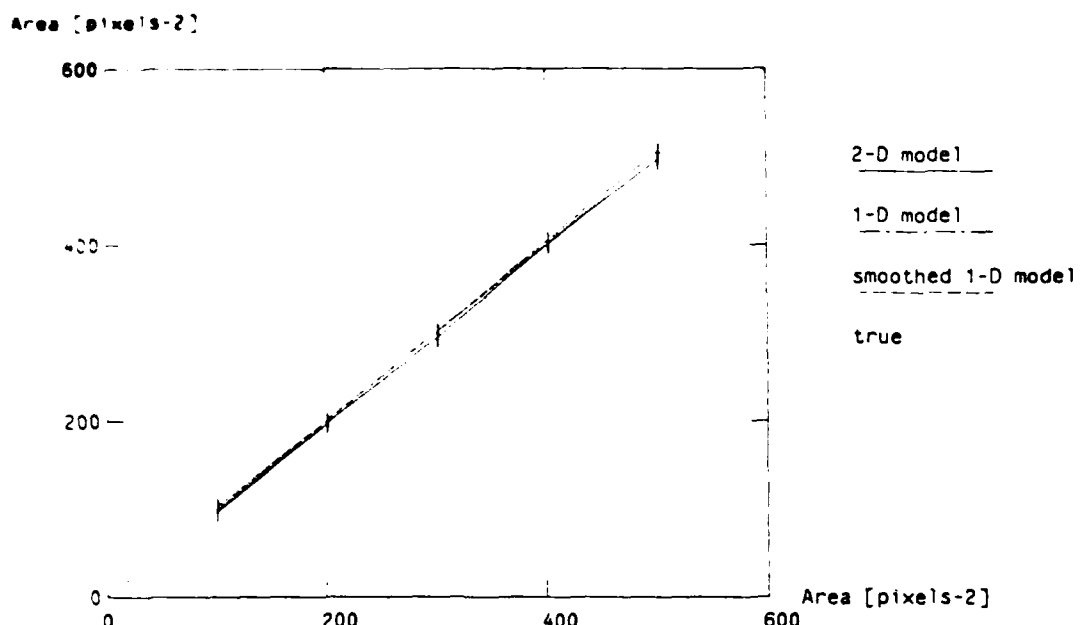


(a) Average of Radius Estimates

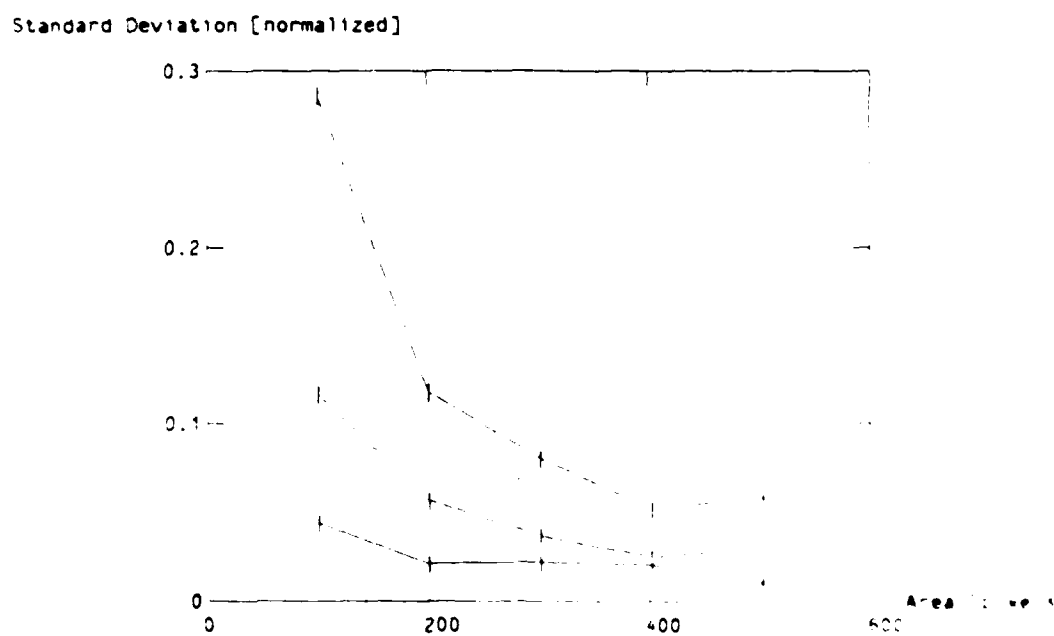


(b) Normalized Standard Deviation of Radius Estimates

Figure 5.6: Radius Estimation for Different Alphas



(a) Average of Area Estimates



(b) Normalized Standard Deviation of Area Estimates

Figure 5.7 Area Estimation for 1000x1000 Areas

AD-A181 671

ESTIMATION OF CORONARY ARTERY DIMENSIONS FROM  
ANGIGRAMS (U) MASSACHUSETTS INST OF TECH CAMBRIDGE  
RESEARCH LAB OF ELECTRONICS T N PAPPAS APR 87 TR-528

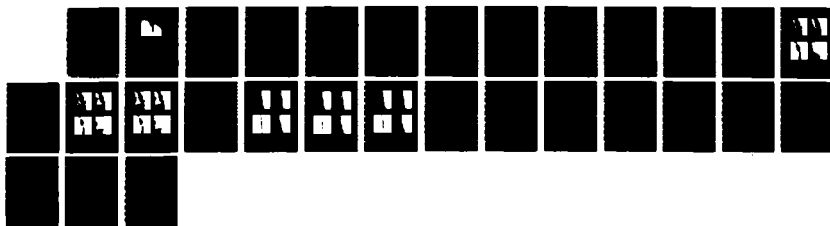
2/2

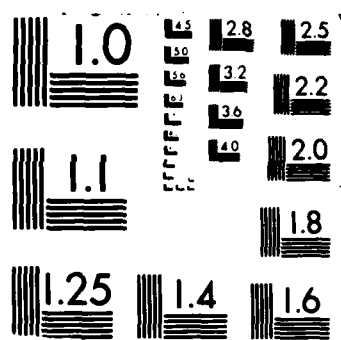
UNCLASSIFIED

N00014-81-K-0742

F/G 6/5

NL





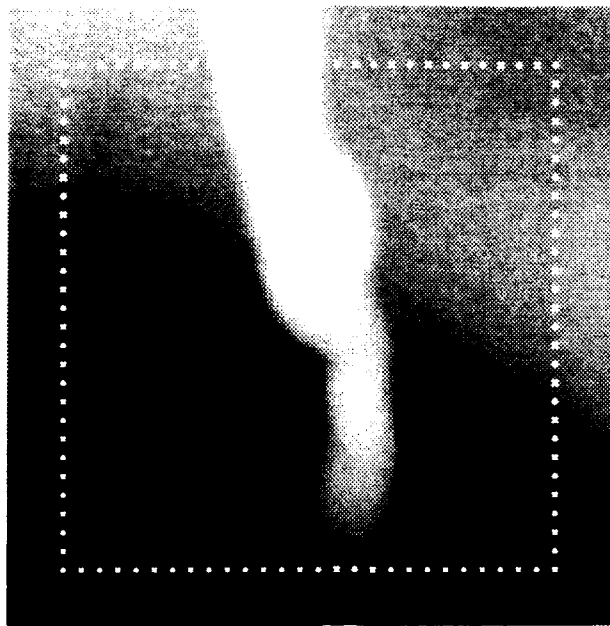


Figure 5.8: Two-Dimensional Synthetic Image

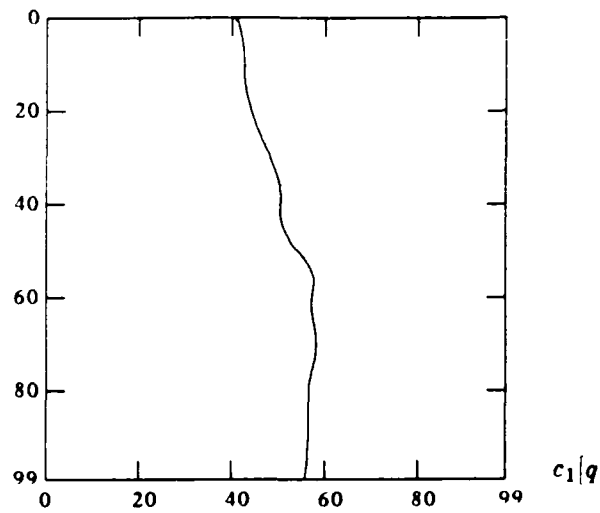
#### 5.1.4 Realistic Example

The previous experiments were designed to study the behavior of the two approaches for different levels of noise and different vessel dimensions. Here we present a more realistic example in order to compare the overall performance of the two methods on synthetic data.

The synthetic image we used in this experiment is  $100 \times 100$  pixels, and is shown in figure 5.8. No noise has been added to this image. The background is a fifth degree two-dimensional polynomial, obtained from a real angiogram profile. The vessel parameter sequences  $c_1[q]$ ,  $r[q]$ , and  $\alpha[q]$  are shown in figures 5.9(a), (b), and (c), respectively. They too were chosen to closely match the vessel projection of a real angiogram. The covariance matrix of the blurring function is  $S = \text{diag}(1, 1)$  (pixels)<sup>2</sup>. The units of  $q$  and the sequences  $c_1[q]$  and  $r[q]$  are in pixels.

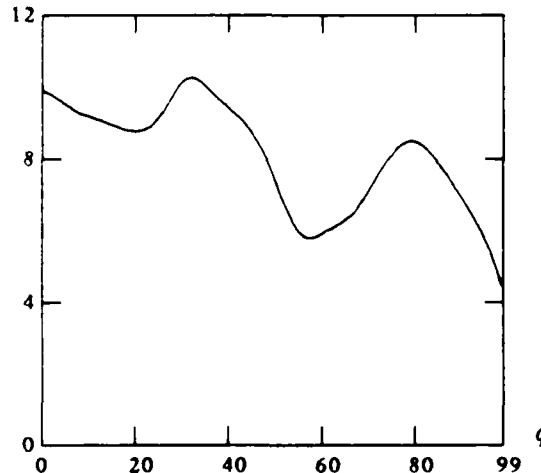
To the synthetic image of figure 5.8 we added seven different levels of noise. The parameter sequences of a section of this image ( $80 \times 80$  pixels, shown in dotted lines

$$c_2[q] = q$$



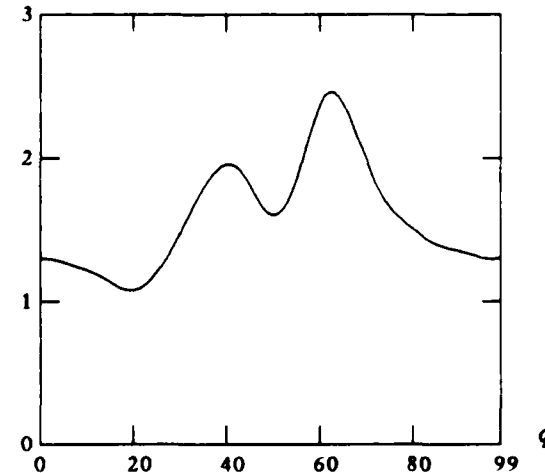
(a) Axis

$$r[q]$$



(b) Radius

$$\alpha[q]$$



(c) Alpha

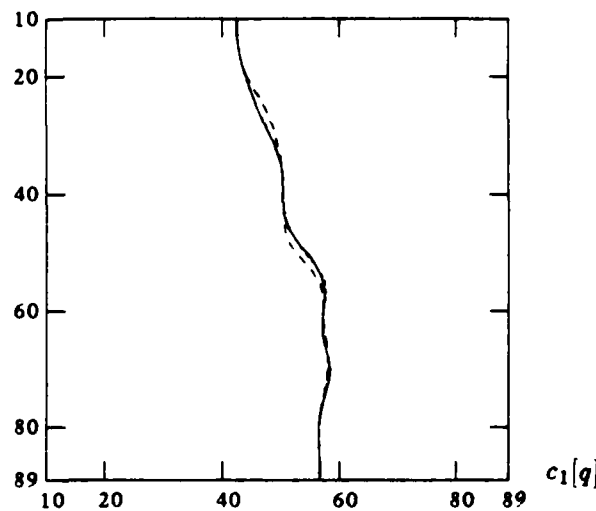
Figure 5.9: Vessel Parameter Sequences

in figure 5.9) were estimated using the two approaches. The degree of both the two-dimensional and the one-dimensional polynomials used in the corresponding approaches was 5, the same as that of the synthetic data. The spacing of the nodes of the cubic splines used in the last stage of the two-dimensional algorithm and for smoothing the one-dimensional estimates was 7 points. A second iteration of the one-dimensional approach was performed to get perpendicular profile estimates. A typical example of the vessel parameter estimates is shown in figure 5.10. They correspond to the case of signal to noise ratio of 16.3 dB. The vessel parameter sequences  $c_1[q]$ ,  $r[q]$ , and  $\alpha[q]$  are shown in figures 5.10(a), (b), and (c), respectively. The solid line represents the two-dimensional model estimates, the dot-dashed line represents the one-dimensional model estimates, and the dotted line shows the true parameter sequences. The smoothed one-dimensional estimates are not shown in this figure.

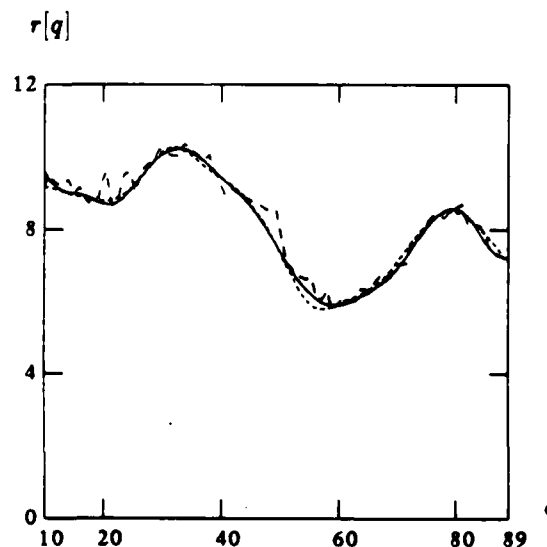
The differences between the true and estimated radius and area sequences were obtained. We then computed the average and standard deviation of these difference sequences. The standard deviation was normalized by the average value of the true radius and area sequences, respectively. The results are shown in figures 5.11 and 5.12 as a function of signal to noise ratio. The signal to noise ratio (SNR) is defined as in equation (4.1) of the previous chapter. The solid line represents the two-dimensional model estimates, the dot-dashed line represents the one-dimensional model estimates without any smoothing, and the dashed line represents the smoothed one-dimensional estimates. Since we are plotting the difference between the true and estimated values, the perfect result would be the zero sequence shown in dotted line. For both the radius and the area estimates we observe that the two-dimensional approach offers some improvement in the average and the standard deviation of the estimates.

The results of this more realistic example are similar to those of the previous sections. The difference in performance between the two-dimensional approach and

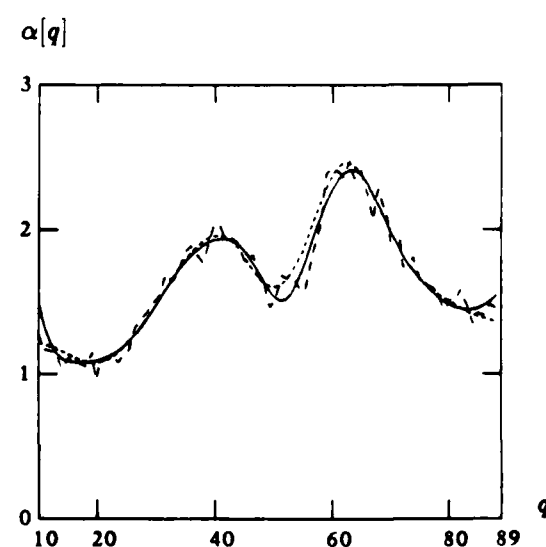
$$c_2[q] = q$$



(a) Axis Estimates

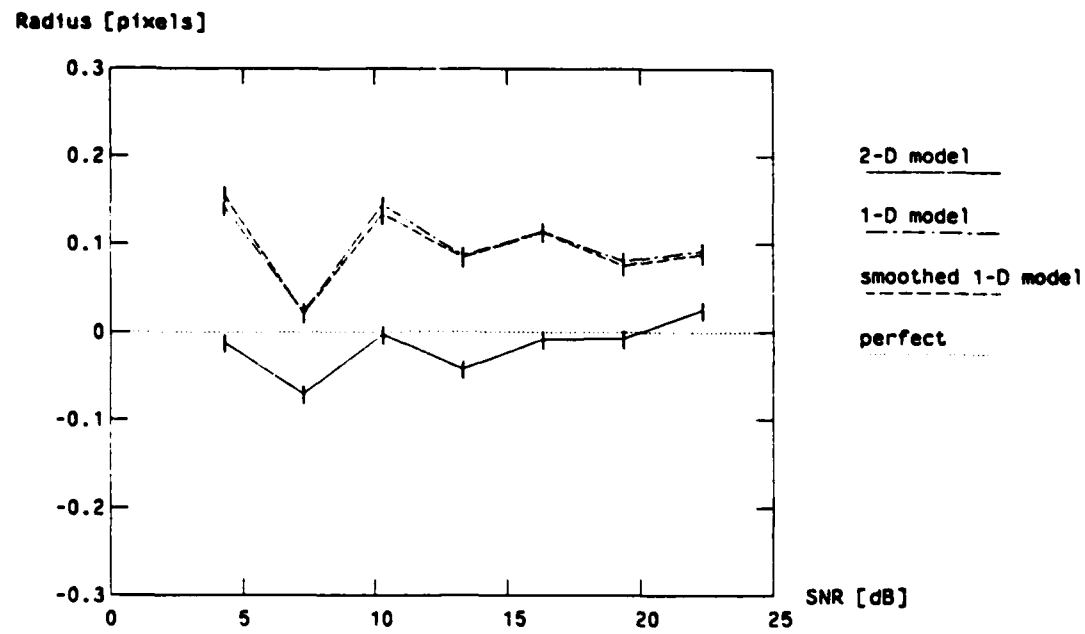


(b) Radius Estimates

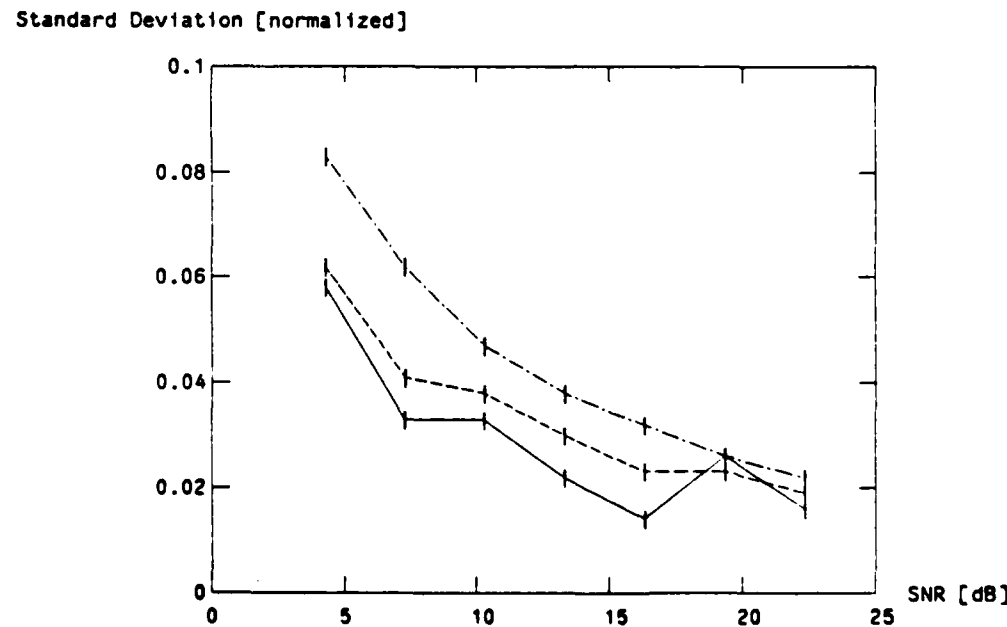


(c) Alpha Estimates

Figure 5.10: Vessel Parameter Estimates

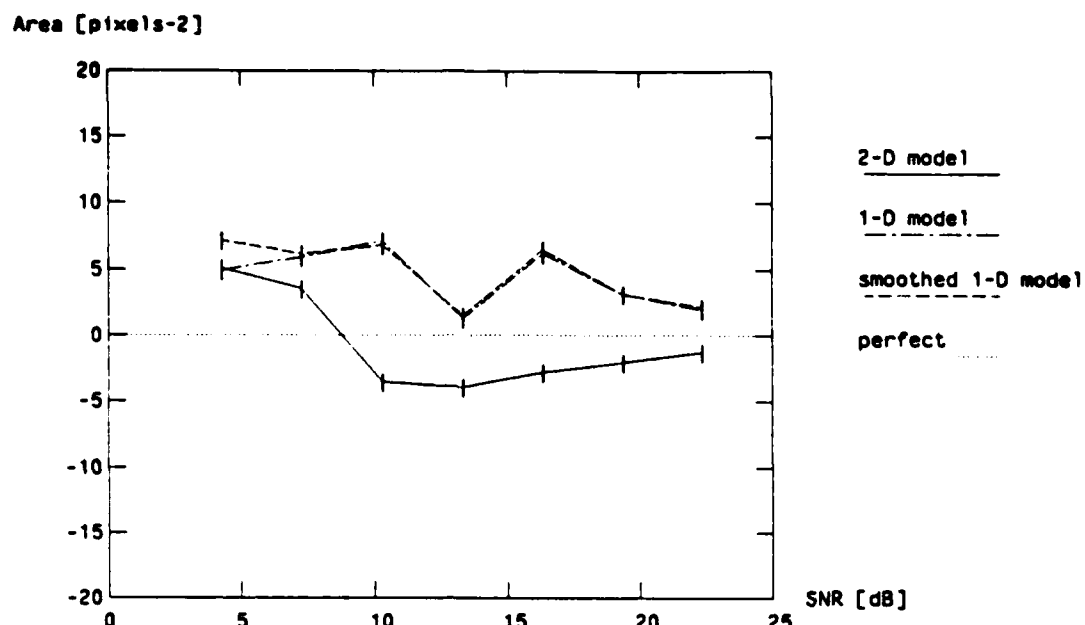


(a) Average of Radius Estimates

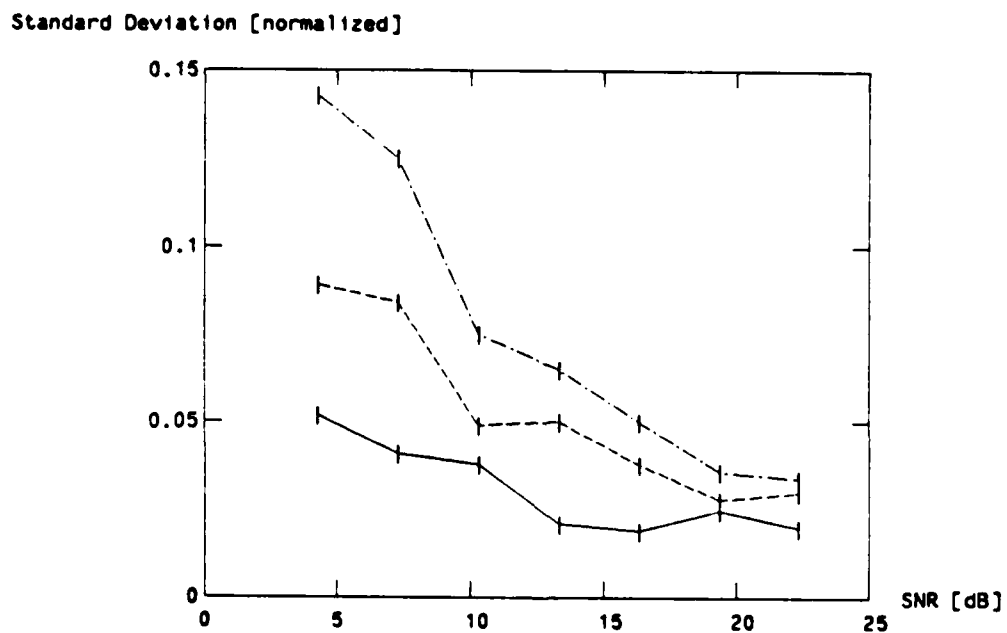


(b) Normalized Standard Deviation of Radius Estimates

Figure 5.11: Radius Estimation for Different SNR's



(a) Average of Area Estimates



(b) Normalized Standard Deviation of Area Estimates

Figure 5.12: Area Estimation for Different SNR's

the smoothed one-dimensional approach we observe here is comparable to that of the previous sections. This means that the earlier experiments were reasonable, even though the vessel shape was too simple.

### 5.1.5 Remarks

Summarizing the results of the synthetic data experiments, we note that the two-dimensional approach offers some improvement in the variance of the estimates, while the average is very close to the true value for both approaches. As expected, the smoothing of the one-dimensional estimates reduces the standard deviation considerably, but does not affect the average.

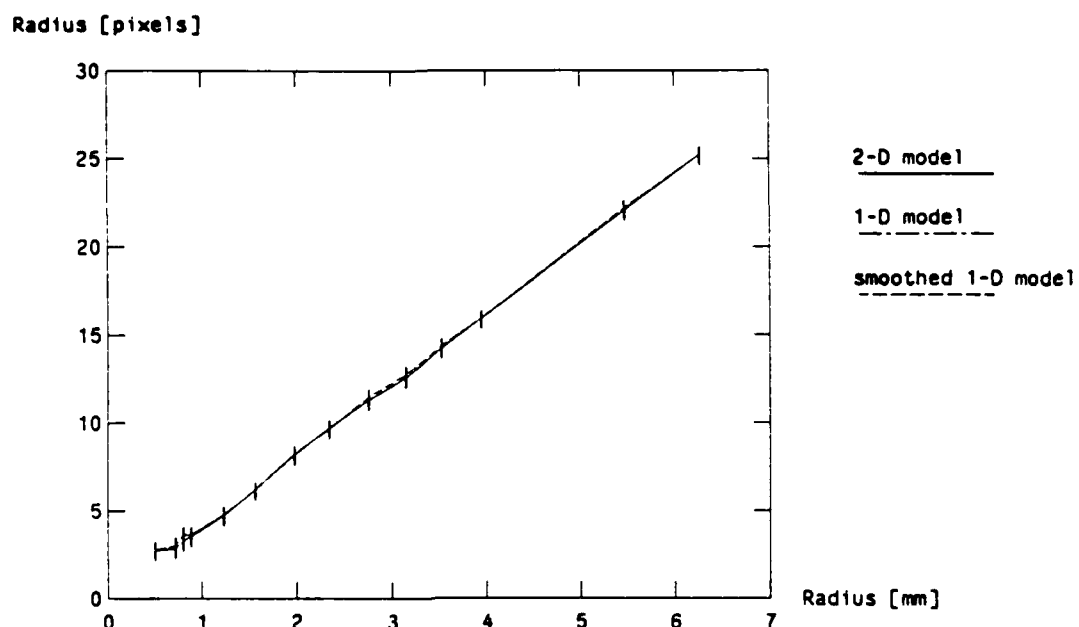
## 5.2 Vessel Phantoms

Now we examine the performance of the algorithms on the vessel phantom x-rays. The phantoms are the same ones that we used in chapter 4. For each vessel phantom we considered a section of the x-ray which contained 50 consecutive profiles of the phantom, and estimated the vessel parameter sequences using the one-dimensional and two-dimensional approaches. Since the phantoms have constant cross-sections, we can compute the average and the standard deviation of the radius and area estimates over  $q$ . The standard deviation of the estimates was normalized in the same way as in section 4.2, by the values on a diagonal line close to the average of the one-dimensional estimates (the exact correspondence between the radius in millimeters and the radius in pixels is not known). This experiment is similar to the radius experiment in the synthetic data case (section 5.1.2). The degree of the polynomials used in the estimation algorithms was 3. As we discussed in section 4.2, a third degree polynomial to model an approximately flat background has better performance. The spacing of the nodes of the cubic splines used in the last stage of the two-dimensional algorithm and for smoothing the one-dimensional estimates

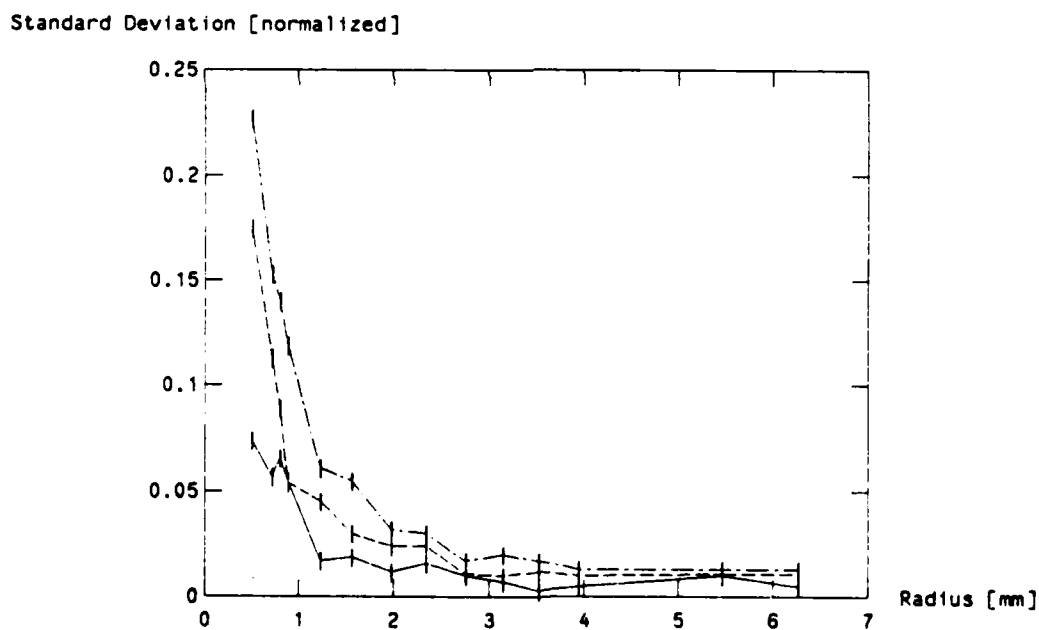
was 7 points.

The average of the radius estimates as a function of true radius is shown in figure 5.13(a) and the normalized standard deviation is shown in figure 5.13(b). The solid line represents the two-dimensional model estimates, the dot-dashed line represents the one-dimensional model estimates without any smoothing, and the dashed line represents the smoothed one-dimensional estimates. The units of the x-axis are millimeters (mm) and of the y-axis pixels. As we discussed in the previous chapter, we are interested in relative measurements. Thus the estimates are satisfactory when they lie on a straight line passing through the origin. We observe that the average of the radius estimates for the two-dimensional model roughly lies on a straight line through the origin, and is very close to the one-dimensional model average. The standard deviation for the two-dimensional approach is lower than the standard deviation for the smoothed one-dimensional approach.

The average of the area estimates as a function of area is shown in figure 5.14(a) and the standard deviation is shown in figure 5.14(b). Both axes of figure 5.14(a) and the x-axis of figure 5.14(b) show the square root of the area, so that the data points are more evenly spaced. The solid line represents the two-dimensional model estimates, the dot-dashed line shows the one-dimensional model estimates without any smoothing, and the dashed line shows the smoothed one-dimensional estimates. Again, there is very little difference in the average of the estimates of the two approaches. The behavior of the average area estimate was discussed in section 4.2 of the previous chapter. The standard deviation of the two-dimensional model estimates is lower than the standard deviation of the smoothed one-dimensional model over most of the range of area values.

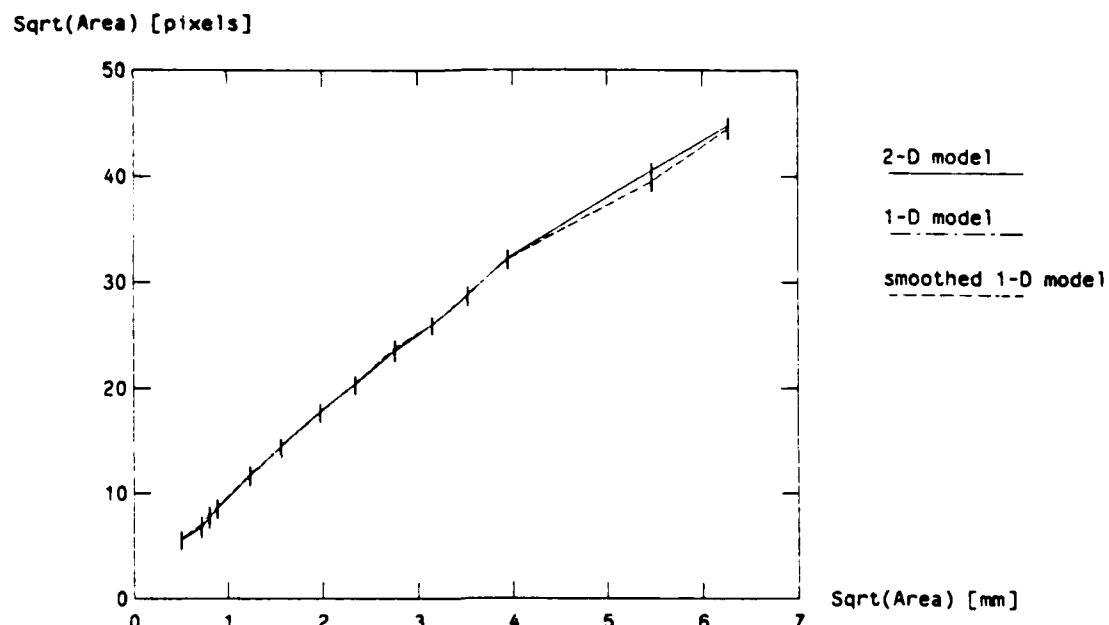


(a) Average of Radius Estimates

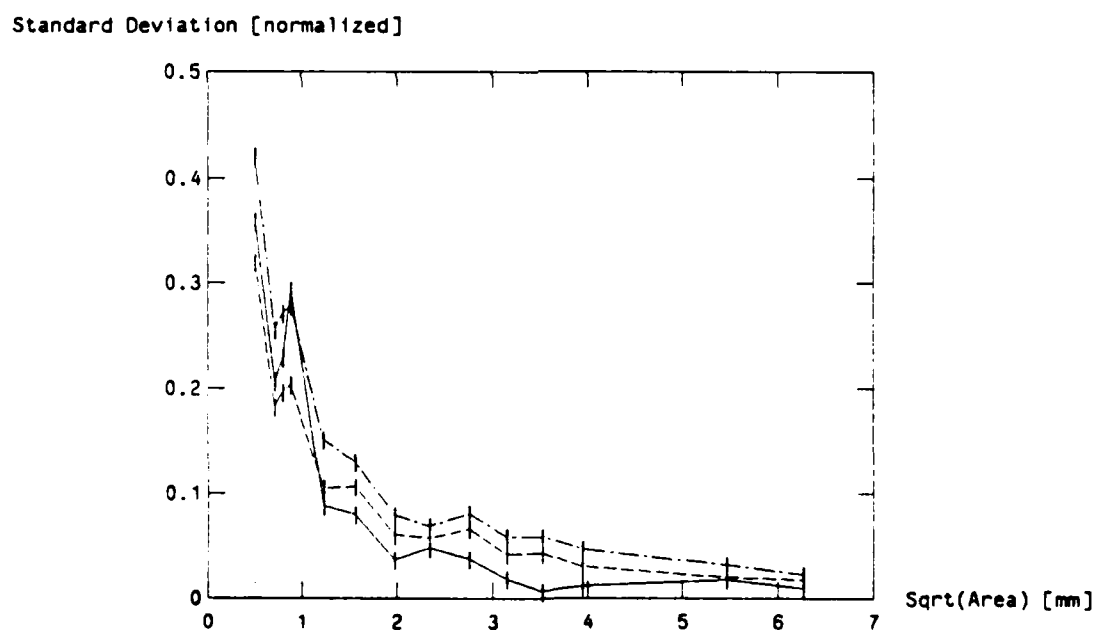


(b) Normalized Standard Deviation of Radius Estimates

Figure 5.13: Phantom Experiment: Radius Estimation



(a) Average of Area Estimates



(b) Normalized Standard Deviation of Area Estimates

Figure 5.14: Phantom Experiment: Area Estimation

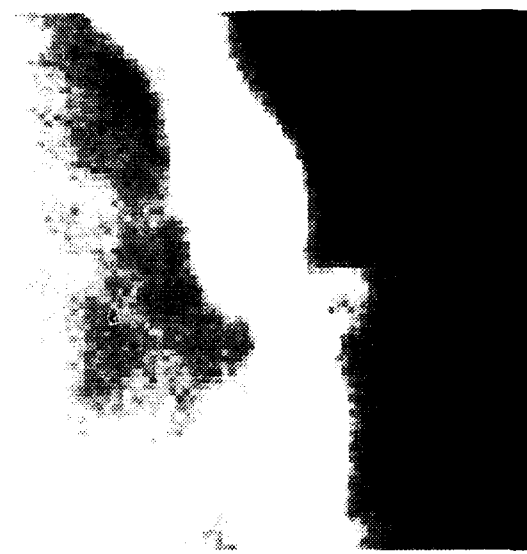
### 5.3 Coronary Angiograms

The performance of the algorithms was also tested on real coronary angiograms. As we mentioned earlier, it is very difficult to evaluate the performance of the algorithms in this case, because we do not know the true dimensions of the arteries. However, a simple inspection of the angiograms and their models can give us a good indication of the relative performance of the two approaches. Thus the comparisons of this section will be qualitative, in contrast to the quantitative results of the previous sections.

In the examples we present, the approximate direction of the blood vessels is vertical. The one-dimensional algorithm was applied to the profiles perpendicular to this direction. More iterations of the algorithm provided the parameters of the perpendicular vessel cross-sections. The degree of the polynomials used in the estimation algorithms was 5. The spacing of the nodes of the cubic splines used in the last stage of the two-dimensional algorithm and for smoothing the one-dimensional estimates was 7 points.

The performance of the two-dimensional model is shown in figure 5.15. Part (a) shows the original image, which is  $80 \times 80$  pixels; part (b) shows the model; part (c) shows the vessel component of the model; and part (d) shows the background component. The estimated radius and area sequences are shown in solid line in figures 5.16(a) and 5.16(b) respectively.

The performance of the one-dimensional model is shown in figure 5.17. Part (a) shows the original image; part (b) shows the model; parts (c) and (d) show the vessel and background components of the model, respectively. Figure 5.18 shows the smoothed one-dimensional model. In these figures we show the results of the first iteration of the algorithm. The profiles in the first stage of the optimization are parallel and nonoverlapping, and hence can be displayed in an image. The profiles of the second stage are in different directions and can only be plotted one at a time. The displayed results are adequate for a qualitative comparison of the



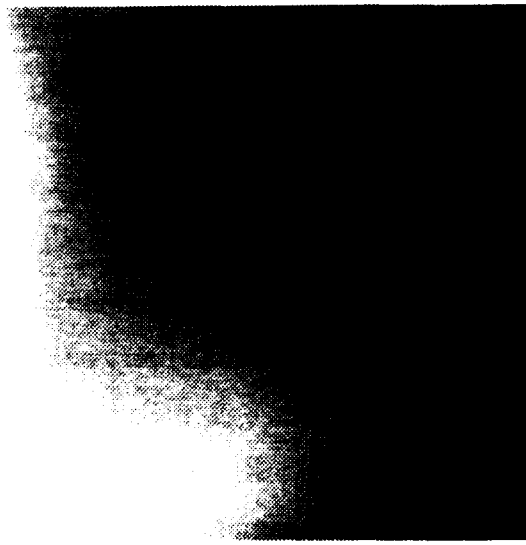
(a) Original



(b) Model

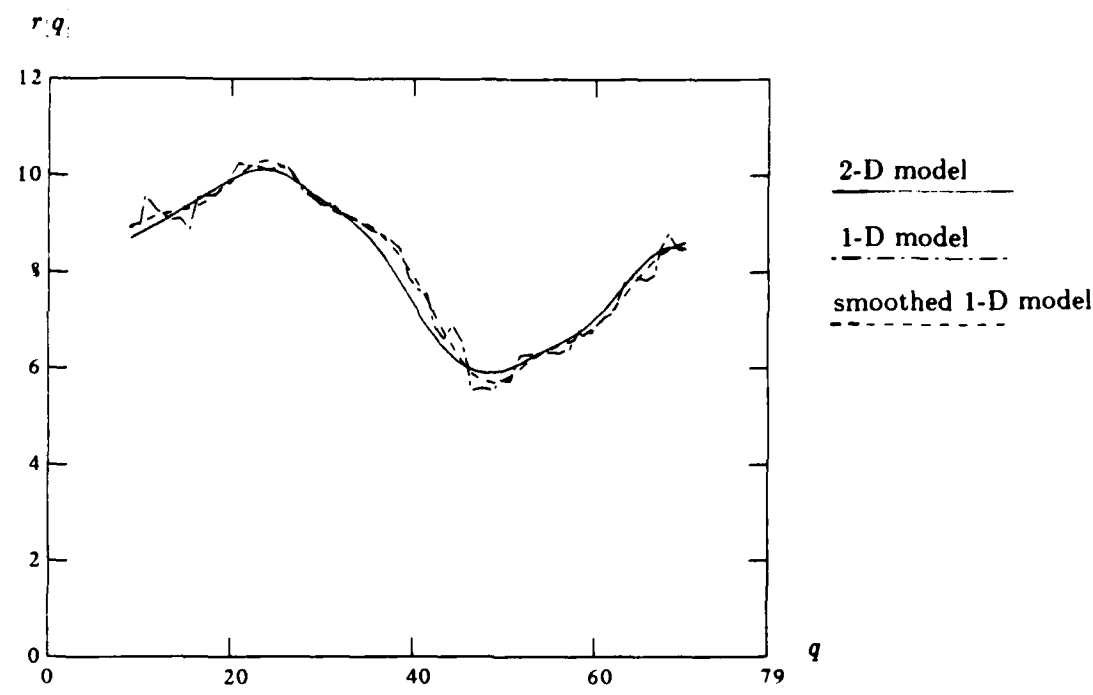


(c) Vessel Component

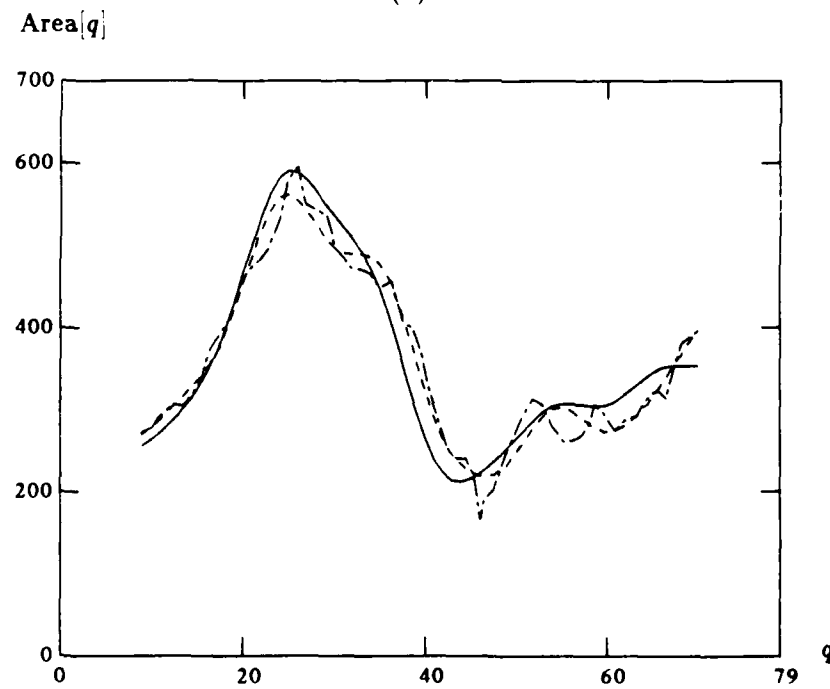


(d) Background Component

Figure 5.15: Two-Dimensional Model (Example A)



(a) Estimated Radius

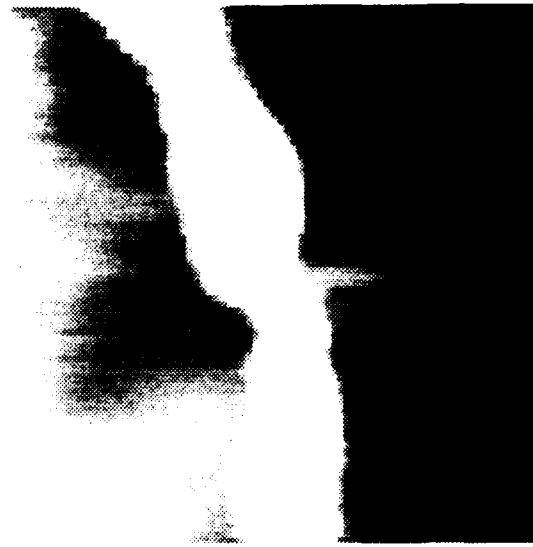


(b) Estimated Cross-Sectional Area

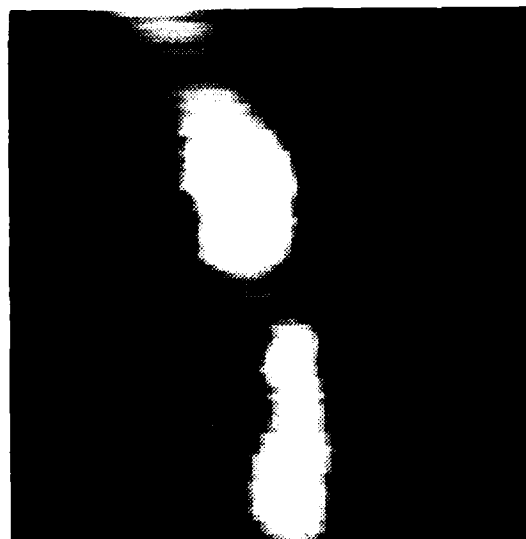
Figure 5.16: Estimated Parameter Sequences (Example A)



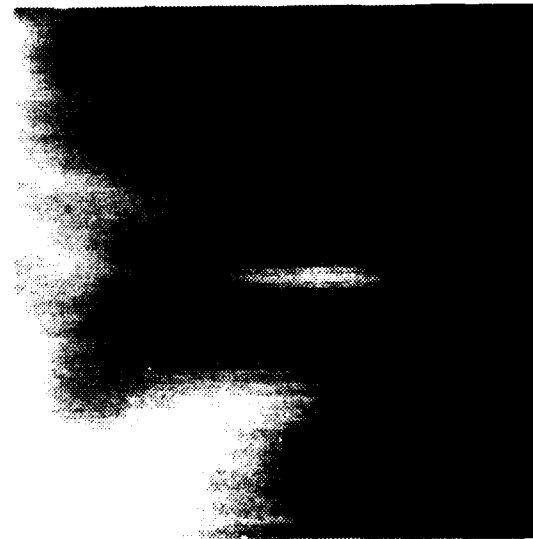
(a) Original



(b) Model



(c) Vessel Component



(d) Background Component

Figure 5.17: One-Dimensional Model (Example A)



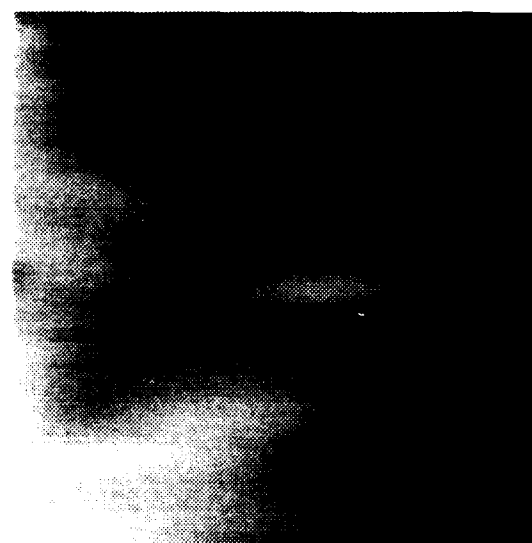
(a) Original



(b) Model



(c) Vessel Component



(d) Background Component

Figure 5.18: Smoothed One-Dimensional Model (Example A)

algorithm performances. For the one-dimensional model, the estimated radius and area sequences of the profiles perpendicular to the vessel are shown in dot-dashed line in figures 5.16(a) and 5.16(b), respectively. The smoothed radius and area sequences are shown in dashed lines.

Comparing figures 5.15 and 5.18, we observe that both models look pretty close to the original. As should be expected the background in the one-dimensional model is discontinuous in the direction of the vessel. However, when we look at the vessel component of the one-dimensional model, we see a valley in the intensity at the narrow point in the middle. This valley is not present in the two-dimensional vessel model, and is apparently caused by the small vessels in the background. This indicates that the two-dimensional model is more robust to non-white noise in the background.

Another example is shown in figures 5.19, 5.20, and 5.21; the resolution is  $80 \times 80$  pixels. We observe that the vessel component of the one-dimensional model has some wide points which are obviously caused by the background noise. The effect of the noise on the two-dimensional vessel estimate is considerably smaller. The signal to noise ratio is very low in this case, and the performance of the two-dimensional model is clearly superior. This observation is consistent with the results of the previous sections, where we showed that the standard deviation of the estimates in the two-dimensional approach becomes significantly smaller for small signal to noise ratios.

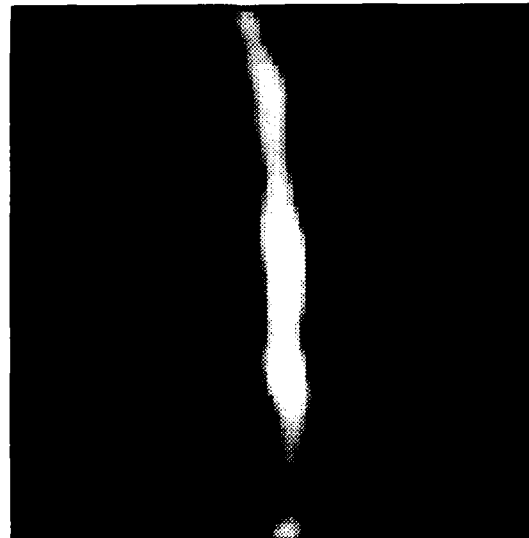
The estimated radius and area sequences of the profiles perpendicular to the vessel are shown in figures 5.22(a) and 5.22(b), respectively. The two-dimensional model estimates are in solid lines, the one-dimensional model estimates are in dot-dashed lines, and the smoothed one-dimensional model estimates are shown in dashed lines.



(a) Original



(b) Model



(c) Vessel Component



(d) Background Component

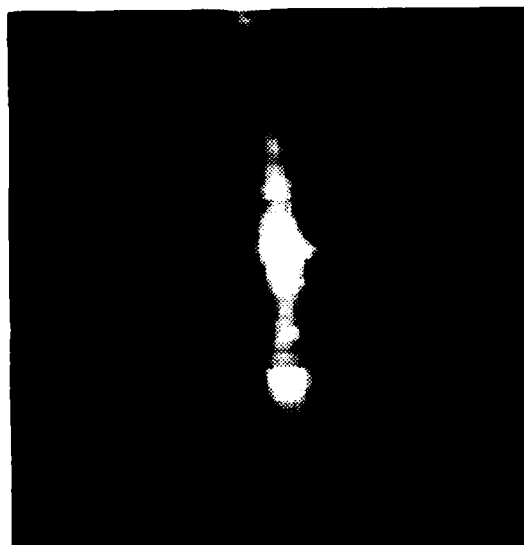
Figure 5.19: Two-Dimensional Model (Example B)



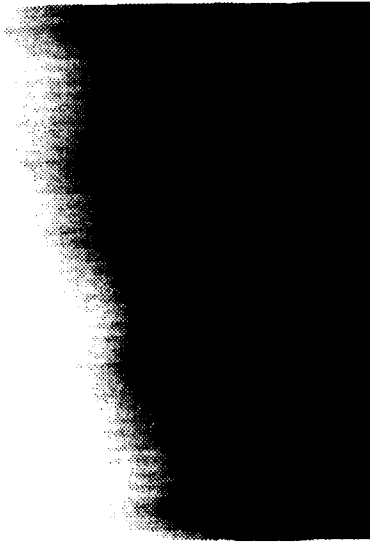
(a) Original



(b) Model



(c) Vessel Component



(d) Background Component

Figure 5.20: One-Dimensional Model (Example B)



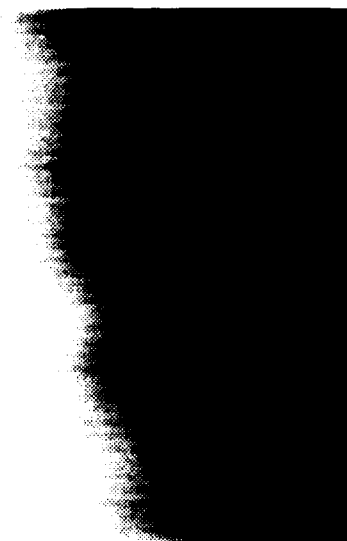
(a) Original



(b) Model

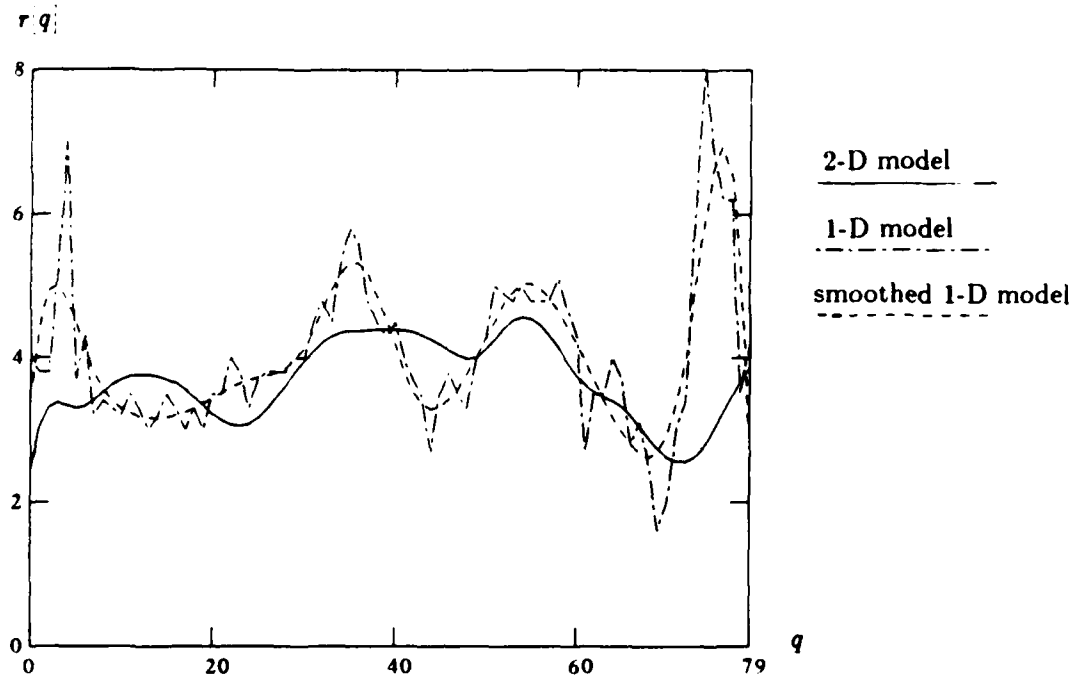


(c) Vessel Component

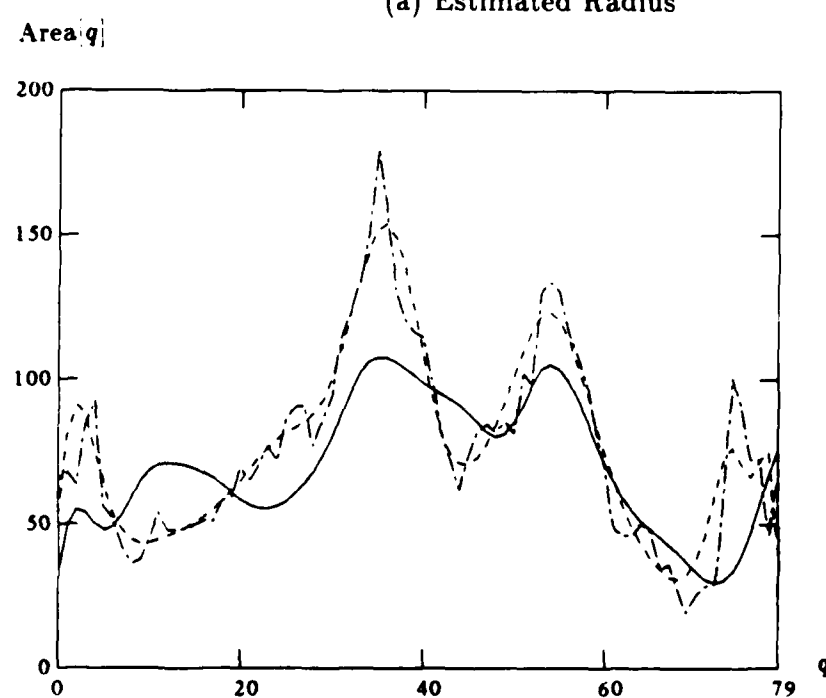


(d) Background Component

Figure 5.21: Smoothed One-Dimensional Model (Example B)



(a) Estimated Radius



(b) Estimated Cross-Sectional Area

Figure 5.22: Estimated Parameter Sequences (Example B)

## 5.4 Summary

The synthetic and phantom data experiments we presented in this chapter indicate that when compared to the smoothed one-dimensional approach the two-dimensional approach offers some improvement in the variance of the estimates, while the average is very close to the true value for both approaches. When we examined the behavior of the algorithms on real coronary angiograms, however, we found that the two-dimensional model is more robust to non-white noise in the background.

As we discussed in chapter 3, the two-dimensional approach requires a lot more computation than the one-dimensional approach. Again, when one considers the time and effort that is required to get an angiogram of the coronary arteries, it appears to be reasonable to spend more time to get better estimates of the severity of the obstructions.

# Chapter 6

## Summary and Future Work

### 6.1 Summary

In this thesis we presented a modeling approach for the estimation of the dimensions of the coronary arteries from coronary angiograms. The model we developed accounts for the structure of the background, as well as distortions introduced by the imaging system. The model takes into account the continuity of both the vessel and the background. The desired vessel dimensions, that is, the diameter and cross-sectional area at each point along the vessel, can be obtained easily from the model parameters. Two models were presented. The first is a two-dimensional model of a section of the angiogram containing a single vessel. The second is one-dimensional model of the profiles of the lines crossing the vessel.

The maximum likelihood estimates of the model parameters were obtained by iterative algorithms. The computational requirements for the one-dimensional algorithm are reasonable. The two-dimensional algorithm requires much more computation than the one-dimensional algorithm. The amount of computation for both algorithms is considerably greater than that of the slope methods.

We tested the algorithms on three types of data. The first type is computer generated data. The second is x-rays of contrast-medium-filled cylindrical phantoms.

The algorithms were also tested on real coronary angiograms. In the experiments we presented we first compared the performance of the one-dimensional model to the slope approaches. Then we compared the performance of the one-dimensional model to that of the two-dimensional model.

Our results indicate that both the one-dimensional and the two-dimensional algorithm have better performance than the conventional slope approaches. This is because the modeling approach uses all the information in the projection image to estimate the model parameters, while the slope approaches use only the slope at the sides of the vessel to determine the vessel boundaries and to estimate the background. We also showed that the two-dimensional algorithm is more robust to non-white noise in the background than the one-dimensional algorithm.

As we discussed in the thesis, the cross-sections of the coronary obstructions are frequently irregular in shape. This suggests that more complicated models of the vessel would be desirable. As the model gets more complicated, however, the problem of estimating the parameters from one projection becomes more and more ill-conditioned. Also the amount of computation increases. The model we developed in this thesis is an attempt to balance the need for an accurate model of the vessels and the requirement of a well-conditioned estimation problem.

Our model can easily be extended to handle the case of multiple vessels in the image segment. It can also be extended to use more projections to reconstruct the elliptical cross-sections. The problem in both cases of course is that the computational requirements and the complexity of the estimation procedure increase significantly.

## 6.2 Suggestions for Further Research

A problem that is not treated in this thesis is that of estimating the severity of obstructions that occur at points where the vessel separates into two branches.

This is an important problem, because stenoses can occur at vessel bifurcations [4]. To estimate the artery dimensions at a bifurcation, one could extend the modeling approach of this thesis. The vessel component of the model would have to be modified to describe a bifurcation. However, the new model will most likely involve more parameters, making the parameter estimation procedure more complicated.

Another interesting problem is that of reconstructing the vessel cross-sections from two or more projections. We have already discussed the problems with obtaining more than one view of the coronary arteries and the difficulty of proper registration of the projections in the various views. Despite these problems the problem of vessel reconstruction from two or more projections has been of interest to many researchers. According to the projection-slice theorem, if we know the projections at all angles, we can reconstruct the object exactly. However, the vessel reconstruction problem has a very special structure. Thus it might be possible to reconstruct the cross-section from two orthogonal projections. The conditions under which this can be achieved are not known. The general problem of reconstructing an array of zeros and ones from two projections (the sum of its rows and columns) is considered in [7]. Approximate reconstructions have been considered by Reiber *et al.* [18,33] and Spears *et al.* [33]. Spears *et al.* use a maximum entropy iterative algorithm to reconstruct the cross-sections from a small number of views. All of the above approaches assume that the vessel component of each projection can be isolated from the background in the presence of blurring and noise. However, as we argued in this thesis, the problem of isolating the vessel component of the projection is not easy.

Finally, there is the problem of combining the information in consecutive frames in time. This would require an accurate procedure to estimate the movement of the vessel from frame to frame, and could lead to improved parameter estimates.

## Bibliography

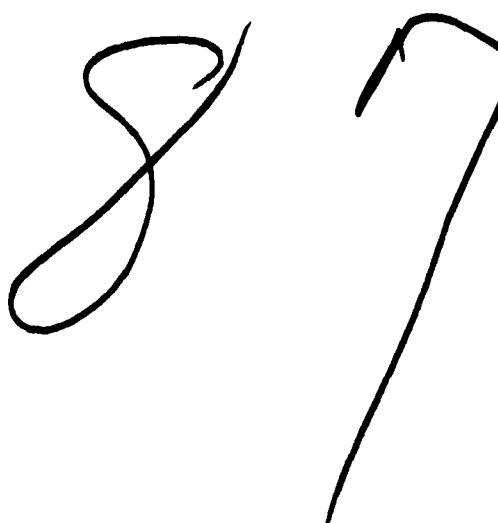
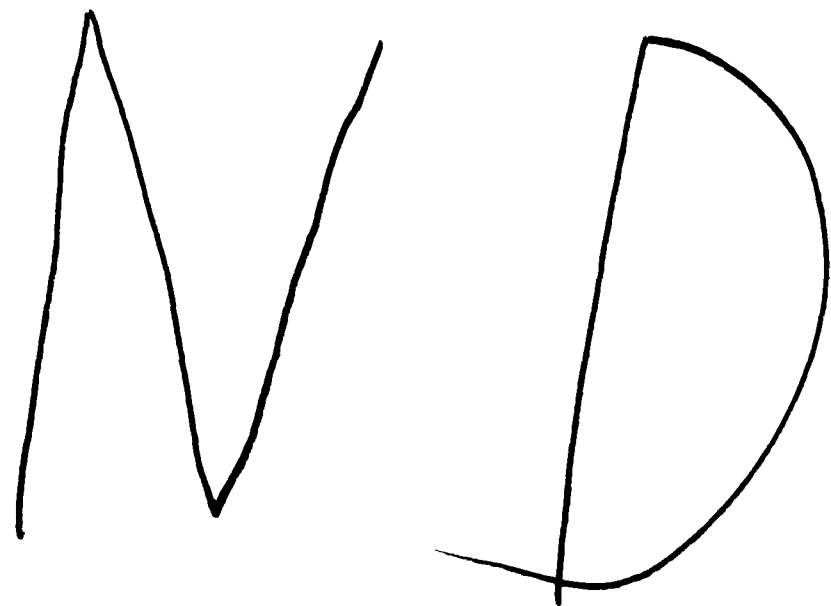
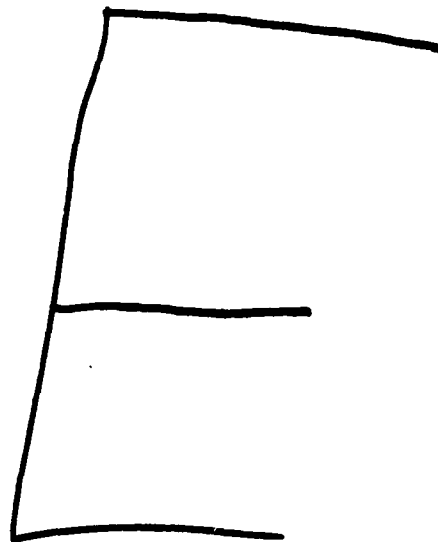
- 1] H. L. Abrams, ed. *Coronary Arteriography*. Little, Brown and Company, 1983.
- 2] G. J. Agin, T. O. Binford, "Computer Description of Curved Objects," *IEEE Trans. Comp.*, Vol. C-25, No. 4, pp. 439-449, April 1976.
- 3] E. L. Alderman et al., "Quantitation of Coronary Artery Dimensions Using Digital Image Processing," *Digital Radiography, SPIE Vol. 314*, pp. 273-278, 1981.
- 4] M. Amiel et al., *Coronary Artery Diseases*. Springer-Verlag, 1984.
- 5] K. Barth et al., "The Objective Measurement of Coronary Obstructions by Digital Image Processing," *Proc. of Int. Workshop on Physics and Eng. in Med. Imaging, IEEE Cat. No. 82 CH1751-7*, pp. 74-78, 1982.
- 6] K. Barth et al., "Quantification of Coronary Stenoses," in *Radiological Functional Analysis of the Vascular System*, (Ed. F. H. W. Heuck), Springer-Verlag, Berlin, pp. 207-213, 1983.
- 7] S. K. Chang, Y. R. Wang, "Three-Dimensional Object Reconstruction from Orthogonal Projections," *Pattern Recognition*, Vol. 7, pp. 167-176, 1975.
- 8] S. D. Conte, Carl De Boor, *Elementary Numerical Analysis*. McGraw-Hill, 1980.
- 9] D. W. Crawford et al., "Rotating Step-Wedge Technique for Extraction of Luminal Cross-Sectional Area Information from Single Plane Coronary Angiograms," *Investigative Radiology*, Vol. 12, pp. 307-313, 1977.
- 10] Carl De Boor, *A Practical Guide to Splines*. Springer-Verlag, Applied Mathematical Sciences, Vol 27, 1978.
- 11] T. A. De Rouen et al., "Variability in the Analysis of Coronary Arteriograms," *Circulation*, 55, pp. 324-328, 1977.

- 12 K. M. Detre et al., "Observer Agreement in Evaluating Coronary Angiograms," *Circulation*, **52**, pp. 979-986, 1975.
- 13 K. L. Gould, K. Lipscomb, "Effects of Coronary Stenoses on Coronary Flow Reserve and Resistance," *Am. J. of Cardiology*, Vol. 34, pp. 48-55, July 1974.
- 14 K. L. Gould, "Pressure-Flow Characteristics of Coronary Stenoses in Unsedated Dogs at Rest and During Coronary Vasodilation," *Circ. Res.*, Vol. 43, pp. 242-..., 1978.
- 15 C. J. Kooijman et al., "Computer-Aided Quantitation of the Severity of Coronary Obstructions from Single View Cineangiograms," *Proceedings of Int. Symp. on Medical Imaging and Image Interpretation*, pp. 59-64, 1982.
- 16 J. H. C. Reiber et al., "Objective Characterization of Coronary Obstructions from Cineangiograms with Single and Multiple Views," *Proceedings of Second Int. Conf. on Visual Psychophysics and Medical Imaging*, Brussels, Belgium, pp. 11-17, 1981.
- 17 J. H. C. Reiber et al., "Transfer Functions of the X-Ray-Cine-Video Chain Applied to Digital Processing of Coronary Cineangiograms," in *Digital Imaging in Cardiovascular Radiology*, (Eds. P. H. Heintzen and R. Brennecke), Georg Thieme Verlag, Stuttgart, pp. 89-104, 1983.
- 18 J. H. C. Reiber et al., "3-D Reconstruction of Coronary Arterial Segments from Two Projections," in *Digital Imaging in Cardiovascular Radiology*, (Eds. P. H. Heintzen and R. Brennecke), Georg Thieme Verlag, Stuttgart, pp. 151-163, 1983.
- 19 J. H. C. Reiber et al., "Coronary Artery Dimensions from Cineangiograms - Methodology and Validation of a Computer-Assisted Analysis Procedure," *IEEE Trans. Med. Imag.*, Vol. MI-3, n. 3, pp. 131-140, 1984.
- 20 J. H. C. Reiber et al., "Computer Assisted Analysis of the Severity of Obstructions from Coronary Cineangiograms: A Methodological Review," *Automedica*, Vol. 5, pp. 219-238, 1984.
- 21 J. R. Rice, *The Approximation of Functions*, Vol 2. Addison-Wesley, 1969.
- 22 K. Rossmann, "Image-Forming Quality of Radiographic Screen-Film Systems: The Line Spread-Function," *Am. J. Roentgenology, Rad. Therapy & Nuclear Med.*, Vol. 90, No. 1, pp. 886-906, July 1963.
- 23 T. Sandor et al., "Cine-Densitometric Measurement of Coronary Arterial Stenoses," *Catheterization and Cardiovascular Diagnosis*, **5**, pp. 229-245, 1979.

- [24] M. E. Sanmarco et al., "Reproducibility of a Consensus Panel in the Interpretation of Coronary Angiograms," *American Heart Journal*, **96**, pp. 430-437, 1978.
- [25] H. J. Scudder, "Introduction to Computer Aided Tomography," *Proceedings IEEE*, Vol. 66, n. 6, pp. 628-637, 1978.
- [26] R. H. Selzer et al., "Computer Analysis of Cardiovascular Imagery," *Proc. of the CALTEC/JPL Conference on Image Processing Technology, Data Sources and Software for Commercial and Scientific Applications*, Pasadena, California, pp. 6-1-6-20, 1976.
- [27] K. Shmueli, "Estimation of Blood Vessel Boundaries in X-Ray Images," Ph.D. Thesis, Stanford University, 1981.
- [28] K. Shmueli et al., "Estimation of Blood Vessel Boundaries in X-Ray Images," *Optical Engineering*, Vol. 22, No. 1, pp. 110-116, 1983.
- [29] D. N. Smith et al., "A Semiautomatic Computer Technique for Processing Coronary Angiograms," *Computers in Cardiology*, pp. 325-328, 1981.
- [30] J. R. Spears, "Rotating Step-Wedge Technique for Extraction of Luminal Cross-Sectional Area Information from Single Plane Coronary Angiograms," *Acta Radiologica Diagnosis*, **22**, pp. 217-225, 1981.
- [31] J. R. Spears et al., "Computer Aided Densitometric Evaluation of Coronary Cineangiograms," in *Radiological Functional Analysis of the Vascular System*, (Ed. F. H. W. Heuck), Springer-Verlag, Berlin, pp. 195-206, 1983.
- [32] J. R. Spears et al., "Computerized Image Analysis for Quantitative Measurement of Vessel Diameter from Cineangiograms," *Circulation*, **68**, pp. 453-461, 1983.
- [33] J. R. Spears et al., "Computer Reconstruction of Luminal Cross-Sectional Shape from Multiple Cineangiographic Views," *IEEE Trans. Medical Imag.*, Vol. MI-2, No. 1, pp. 49-54, March 1983.
- [34] Harry L. Van Trees, *Detection, Estimation, and Modulation Theory, Part I*. Wiley, New York, 1968.
- [35] E. H. Timothy Whitten, "Orthogonal Polynomial Trend Surfaces for Irregularly Spaced Data," *Mathematical Geology*, Vol. 2, No. 2, pp. 141-152, 1970.
- [36] L. M. Zir et al., "Interobserver Variability in Coronary Angiography," *Circulation*, **53**, pp. 627-632, 1976.

DISTRIBUTION LIST

	<u>DODAAD Code</u>	
<b>Director</b> Defense Advanced Research Project Agency 1400 Wilson Boulevard Arlington, Virginia 22209 Attn: Program Management	HX1241	(1)
<b>Head Mathematical Sciences Division</b> Office of Naval Research 800 North Quincy Street Arlington, Virginia 22217	N00014	(1)
<b>Administrative Contracting Officer</b> E19-628 Massachusetts Institute of Technology Cambridge, Massachusetts 02139	N66017	(1)
<b>Director</b> Naval Research Laboratory Attn: Code 2627 Washington, D. C. 20375	N00173	(6)
<b>Defense Technical Information Center</b> Bldg 5, Cameron Station Alexandria, Virginia 22314	S47031	(12)
<b>Dr. Judith Daly</b> DARPA / TTO 1400 Wilson Boulevard Arlington, Virginia 22209		(1)



A hand-drawn circle, a hand-drawn 'T' with a dot above it, and a hand-drawn circle.